Università degli Studi di Torino
Doctoral School of the University of Torino
PhD Programme in Chemical and Materials Sciences XXXIIIth Cycle

Magnetic Resonance Spectroscopies for the Characterization of V^{4+} Species in Solid State and Molecular Systems

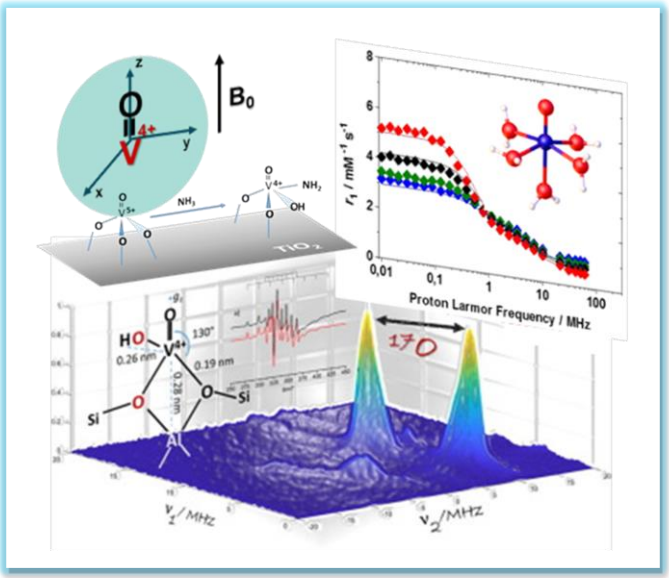

Valeria Lagostina

Supervisor:
Prof. Mario Chiesa

Università degli Studi di Torino

Doctoral School of the University of Torino

PhD Programme in Chemical and Materials Sciences XXXIIIth cycle

Magnetic Resonance Spectroscopies for the Characterization of V^{4+} Species in Solid State and Molecular Systems

Candidate: **Valeria Lagostina**

Supervisor: Prof. **Mario Chiesa**

Jury Members:

Prof. **Barbara Bonelli**
Politecnico di Torino
Dipartimento Scienza Applicata e Tecnologia

Prof. **Mauro Botta**
Università del Piemonte Orientale
Dipartimento di Scienze ed Innovazione Tecnologica

Prof. **Maria Cristina Paganini**
Università degli studi di Torino
Dipartimento di Chimica

Head of the Doctoral School: Prof. Alberto Rizzuti
PhD Programme Coordinator: Prof. Bartolomeo Civalleri

Torino, 2021

Summary

Preface

Many of the chemical reactions which take place at surfaces and interfaces involve paramagnetic species. Unpaired electrons associated with surface localized chemical entities, such as transition metal ions (TMIs), are often involved in the formation of temporary chemical bonds with the reacting molecules, leading to specifically activated complexes or reaction intermediates. On the other hand, highly reactive molecules containing one or more broken bonds can be stabilized on surfaces or within porous media such as molecular sieves.

These stabilized molecules, which are often paramagnetic, offer the possibility of controlled reactions with other molecules to produce specific products, whereas the corresponding gas-phase reaction would not be as selective. Moreover, the same open-shell species as part of molecular complexes, can be important model systems in many different technological areas, ranging from magnetic resonance imaging (MRI) to quantum information technologies. In any of these applications, structure-function relationships need to be established to engineer spin-lattice relaxation times and phase-memory relaxation times.

These considerations suggest that Electron Paramagnetic Resonance (EPR) spectroscopy, with its ability to detect small concentrations of paramagnetic species and to probe in detail those features of their electronic structure associated with the unpaired electron spin distribution, will be a useful method of investigating solid-state and molecular systems involving transition metal ions in paramagnetic states, which can be of relevance in a

wide range of applications ranging from catalysis to the development of new contrast agents and quantum information technologies. The potential of EPR in the characterization of paramagnetic species can be enormously extended by exploiting advanced pulse methods, which have successfully been employed in the characterization of biochemical systems but are still of limited application in the field of heterogeneous catalysis and surface chemistry. In particular, so-called *hyperfine spectroscopy* (ESEEM, ENDOR, HYSCORE) allows monitoring the distribution of the unpaired electrons wave function over first and second coordinative shells, which is one of the most useful of the molecular "fingerprints" obtained from an EPR spectrum.

Herer continuous wave (CW) and pulse EPR methods are applied in order to advance the understanding of vanadium species at surfaces and interfaces and to answer specific questions inherent with their structure, distribution and reactivity to explore the spin dynamics in molecular systems.

The thesis is organized as follows: a general introduction on the vanadium chemistry, containing systems for catalytic applications with emphasis on the application of EPR spectroscopy as a tool to gain insights into their structure is given in Chapter 1; the theoretical basis of CW and pulse EPR techniques are reported in Chapter 2; samples preparation and experimental methods are illustrated in Chapter 3; the results obtained for the characterization of the heterogeneous catalysts are reported and discussed in Chapter 4, while vanadyl molecular complexes are dealt with in Chapter 5; conclusions and outlook to the future are reported in the last paragraph.

Chapter 1

Introduction

1.1 Vanadium

Vanadium is a 5th group transition metal element (with niobium and tantalum) with electronic configuration [Argon]4s^{2}3d^3. Moreover, vanadium is characterized by two isotopes, a stable one ^{51}V, and a radioactive one ^{50}V, with a half-life of 1.5 × 10^{17} years and a natural abundance of 0.25%.

V exhibits a range of oxidation states, from -1 to +5, especially in molecular complexes with a very large different type of ligands. [1]

However, in aqueous media are accessible the oxidation states from +2 (d^3) to +5 (d^0), which are characterized by aquo-complexes with different colours (violet for $[V(H_2O)_6]^{2+}$, green for $[V(H_2O)_6]^{3+}$, blue for $[VO(H_2O)_5]^{2+}$ and yellow $[VO(H_2O)_5]^{+}$).

The standard redox processes [2] that characterize the aqueous solution are:

$$VO_2^+{}_{aq} + 2H^+{}_{aq} \rightleftharpoons VO^{2+}{}_{aq} + H_2O \quad E_0 = +1\,V$$

$$VO^{2+}{}_{aq} + 2H^{+}{}_{aq} \rightleftharpoons V^{3+}{}_{aq} + H_2O \quad E_0 = +0.34\,V$$

$$V^{3+}{}_{aq} \rightleftharpoons V^{2+}{}_{aq} \quad E_0 = -0.26\,V$$

In Figure 1 is reported the pH versus potential diagram for vanadium, which shows a good stability of the vanadyl (VO^{2+}) species in acid solution, while V^{5+} species are predominant at basic pH.

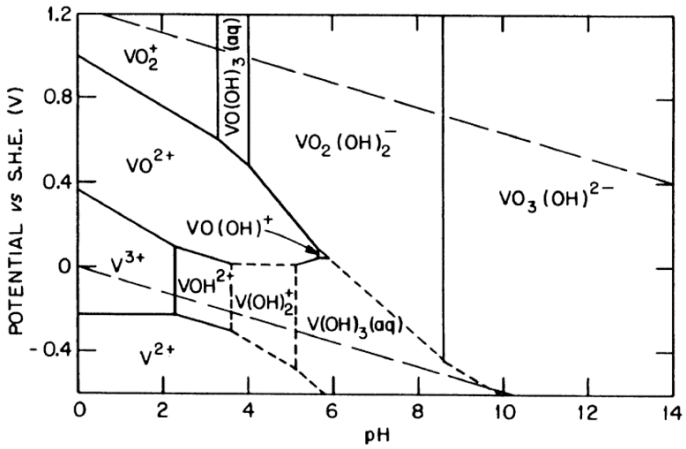

Figure 1: Diagram of potential (vs. SHE) vs. pH for vanadium species present in dilute solutions. The upper and lower dashed lines represent respectively 1 atm O_2 and 1 atm H_2. [3]

The diatomic structure of VO^{2+} is indeed a particular case in chemistry, because presents a multiple bonding between vanadium and oxygen. The formation of this bond is due to a strong Lewis acidity of the metal that, in turn, increases the Brønsted acidity of the water that can lose, depending on the pH solution, one or two protons with the formation of hydroxo or oxo species. The VO^{2+} formed is so stable that the deprotonation reaction is irreversible even in concentrated acid solutions. [4]

The electronic structure of the molecular orbitals of VO^{2+} in water is explained with a model introduced by Ballhausen and Gray [5] in 1962, which describes the combination of vanadium and water oxygen orbitals in C_{4v} symmetry.

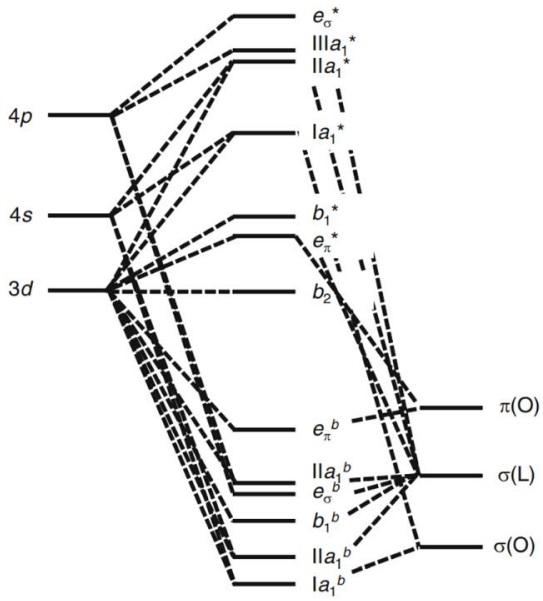

Figure 2: electronic structure of $VO(H_2O)_5^{2+}$ ion, adapted from. [4,5]

Table 1: scheme of orbital transformation from. [5]

Representation	Metal orbital	Ligand orbitals
a_1	$3d_{z^2} + 4s$	σ_5
	$4s - 3d_{z^2}$	$^1/_2\,(\sigma_1 + \sigma_2 + \sigma_3 + \sigma_4)$
	$4p_z$	σ_6
e	$3d_{xz}, 3d_{yz}$	$\pi_5(2p_x, 2p_y)$
	$4p_x, 4p_y$	$^1/_{\sqrt{2}}(\sigma_1 - \sigma_3), ^1/_{\sqrt{2}}(\sigma_2 - +\sigma_4)$
b_1	$3d_{x^2-y^2}$	$^1/_2\,(\sigma_1 - \sigma_2 + \sigma_3 - \sigma_4)$
b_2	$3d_{xy}$	

The nucleus of ^{51}V, characterized by a nuclear spin $I = {}^{7}/_{2}$, is often used in NMR spectroscopy for investigations in both solution and solid state. [6]

Moreover, the stability of the 4+ oxidation state, characterized by a doublet ground state, makes EPR spectroscopy particularly well suited to investigate this species. Most of EPR investigations are restricted to V^{4+} $(S = {}^{1}/_{2})$,however, also V^{3+} and V^{2+} species are measurable via EPR, but both these oxidation states are characterized by S > ${}^{1}/_{2}$, that introduce zero-field splitting terms that require high-frequency spectrometer (291 GHz) to obtain informative spectra. [7]

Moreover, in EPR is possible to directly detect the hyperfine coupling between the unpaired electron with an active nucleus, which generates a splitting of the EPR transition into $2 * I + 1$ lines (green arrows in Figure 3).

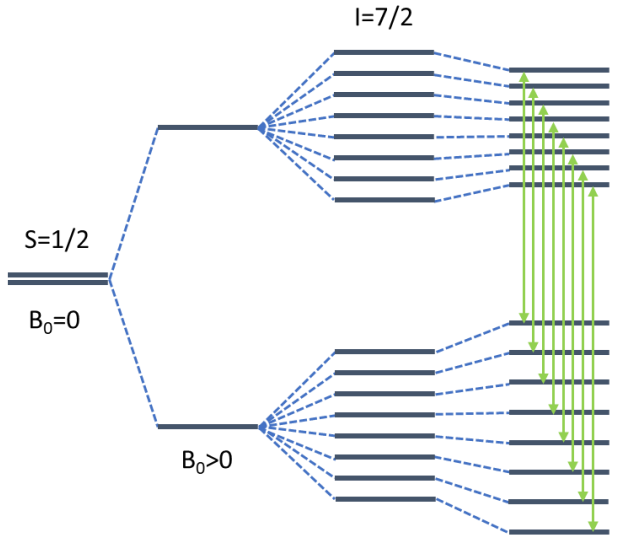

Figure 3: Schematic representation of V^{4+} EPR transitions.

As example case, it is reported the $[VO(H_2O)_5]^{2+}$ complex in water at room temperature (Figure *4*a) and 77 K (Figure *4*b).

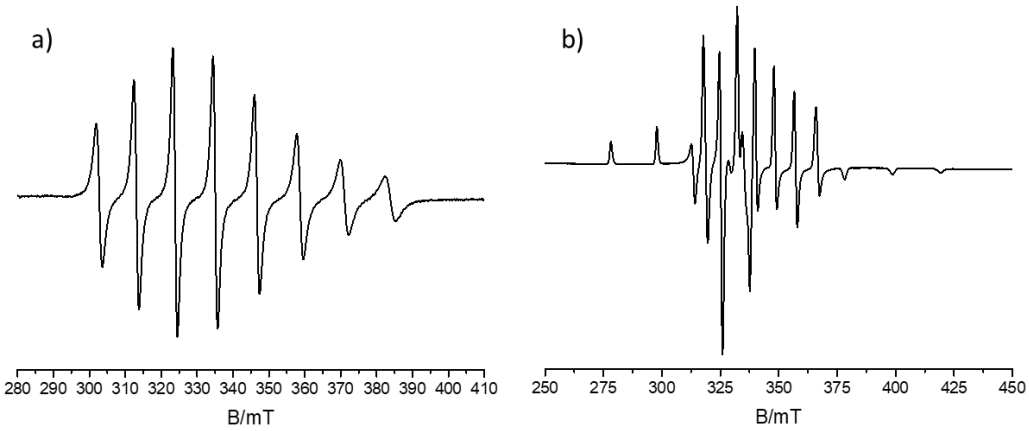

Figure 4: X-band CW EPR spectra of $[VO(H_2O)_5]^{2+}$ at a) room temperature and b) 77 K.

1.2 Catalytic application of vanadium

Vanadium compounds are largely used and studied in the context of both homogeneous and heterogeneous catalysis. In the past 50 years, in fact, the chemistry of vanadium has had a very large development in various catalysis fields, as reported in a recent review. [8]

In homogeneous catalysis vanadium compounds are used as catalysts for the selective oxidation of organic molecules, [9] including alcohols, ketones, epoxides, aldehydes, organohalides, and carboxylic acids, using molecular oxygen as the oxidant. [10,11] Vanadium also shows an interesting role as a catalyst for olefin homo- and copolymerization, like vanadium-based Ziegler−Natta polymerization. [12] In addition, it is also reported the use of

vanadium complexes in the formation of asymmetric sulfide and α-hydroxy acid oxidations, epoxidations, cyanations of aldehydes, Friedel–Crafts reactions, Michael additions, and oxidative couplings of polycyclic phenols.[13]

Heterogeneous vanadium catalysis is based on supported vanadium oxide species and solid-state compounds containing vanadium species that are active and selective for a variety of catalytic commercial systems. In gas-phase chemistry of small organic compounds, catalysts containing vanadium sites are used for methanol oxidation to formaldehyde, [14,15,16] selective oxidation of butane to maleic anhydride, [17] selective oxidation of propene to acrolein and ammoxidation of propene to acrylonitrile. [18] Vanadium catalysts are also tested for oxidative dehydrogenation and show good activity especially for propane to propylene reaction. [19,20,21] Moreover, one of the most important applications of vanadium-supported catalysts is the selective catalytic reduction (SCR) of NO_x by ammonia, which is commercially used for stationary engines. [22,23,24]

Questions about the nature of the active species and the reaction mechanisms remain often open for both homogeneous and heterogeneous systems. In solid systems, the identification of the vanadium active site is particularly challenging because different surface centres can be present.

The properties of supported vanadium oxides on high surface area oxide supports (SiO_2, Al_2O_3, etc.), focusing on their application as oxidative catalysts, [25] for the functionalization of alkanes and alkenes, [26] and on selective oxidation of light alkanes. [27] It also investigates structure–reactivity relationships in catalytic gas-phase oxidation reactions.[28]

In the case of SCR catalysts, the Raman and Fourier Transform Infrared (FTIR) spectroscopy have largely been used to interrogate surface chemistry of vanadia at near SCR-relevant conditions. [29,30] To have a better understanding of the surface properties of these catalytic systems, the use of EPR spectroscopy is also introduced because during the SCR reaction the formation of reduced V^{4+} species, detectable via EPR spectroscopy, is observed. Moreover, it is possible to build an experimental set-up with a reactor heated with a flow of gas that permits to directly follow the reactions inside the cavity of the EPR instrument under so-called *operando* conditions. [31,32,33] It is also possible to study with EPR spectroscopy catalytic systems in *ex-situ* condition, that means after activation at relevant reaction conditions. [34]

EPR is also largely used in the study of vanadium zeolites, prepared with different synthetic strategies, and mesoporous materials use in catalytic applications. It is reported the use of EPR also in combination with DFT calculation to fine modeling of the V sites in different zeolite structures. [35] The advanced pulse-EPR techniques are also used to investigate the fine properties of different frameworks structure, either when the vanadium is exchanged as counter ions in ZSM-5 [36] or SBA-15, [37] or when is a cation substituted in the zeolite frameworks. [38]

References Chapter 1

[1] Crans, D. C. and Smee, J. J., Jon A. McCleverty, Thomas J. Meyer, Comprehensive Coordination Chemistry II, Pergamon, 2004, 175-239.

[2] Cotton, F. A.; Wilkinson, G.; Murillo, C. A.; Bochmann, M., Advanced Inorganic Chemistry, 6th ed.; John Wiley & Sons: New York, 1999.

[3] Baes, J.; Charles F.; Mesmer, R. E. In The Hydrolysis of Cations; Baes, J., Charles F., Mesmer, R. E., Eds.; John Wiley & Sons: New York, 1976.

[4] J. R. Winkler, H. B. Gray, *Struct. Bond.*, 2012, 142, 17–28.

[5] C. J. Ballhausen, H. B. Gray, *Inorg. Chem.*, 1962, 1, 111-122.

[6] D. Rehder, T. Polenova, M. Bühl, *Annu. Rep. NMR Spectrosc*., 2007, 62, 49-114.

[7] J. Krzystek, A. Ozarowski, J. Telser, D. C. Crans, *Coo. Chem. Rev.*, 2015, 301–302, 123–133.

[8] Langeslay R.R., Kaphan D.M., Marshall C.L., Stair P.C., Sattelberger A.P., Delferro M., *Chem. Rev.,* 2019, 119, 2128−2191.

[9] Schwendt, P.; Tatiersky, J.; Krivosudský, L.; Šimuneková, M., *Coord. Chem. Rev*., 2016, 318, 135−157.

[10] da Silva, J. A. L.; da Silva, J. J. R. F.; Pombeiro, A. J. L., Coord. Chem. Rev., 2011, 255, 2232−2248.

[11] Sutradhar, M.; Martins, L. M. D. R. S.; Guedes da Silva, M. F. C.; Pombeiro, A. J. L., Coord. Chem. Rev., 2015, 301−302, 200−239.

[12] Gambarotta, S., Coord. Chem. Rev., 2003, 237, 229−243.

[13] Pellissier, H., Coord. Chem. Rev. 2015, 284, 93−110.

[14] Forzatti, P.; Tronconi, E.; Elmi, A. S.; Busca, G., Appl. Catal., A 1997, 157, 387−408.

[15] Weckhuysen, B. M.; Keller, D. E., Catal. Today, 2003, 78, 25−46.

[16] Wachs, I. E.; Deo, G.; Juskelis, M. V.; Weckhuysen, B. M., Stud. Surf. Sci. Catal., 1997, 109, 305−314.

[17] Dummer, N. F.; Bartley, J. K.; Hutchings, G. J., Adv. Catal., 2011, 54, 189−247.

[18] Brazdil, J. F. A., Appl. Catal., A 2017, 543, 225−233.

[19] Kainthla, I.; Bhanushali, J. T.; Keri, R. S.; Nagaraja, B. M., *Catal. Sci. Technol.*, 2015, 5, 5062−5076.

[20] Carrero, C. A.; Schloegl, R.; Wachs, I. E.; Schomaecker, R., *ACS Catal.*, 2014, 4, 3357−3380.

[21] Sattler, J. J. H. B.; Ruiz-Martinez, J.; Santillan-Jimenez, E.; Weckhuysen, B. M., *Chem. Rev.*, 2014, 114, 10613−10653

[22] Arnarson, L.; Falsig, H.; Rasmussen, S. B.; Lauritsen, J. V.; Moses, P. G., *Phys. Chem. Chem. Phys*., 2016, 18, 17071−17080.

[23] Forzatti, P., *Appl. Catal. A: Gen*., 222, 2001, 21–236.

[24] Lai, J.-K.; Wachs, I. E. A, *ACS Catal.*, 2018, 8, 6537−6551.

[25] Wachs, I. E., *Dalton Trans.*, 2013, 42, 11762−11769.

[26] Maurya, M. R.; Kumar, A.; Costa Pessoa, J., Coord. Chem. Rev. 2011, 255, 2315−2344.

[27] Chu, W.; Luo, J.; Paul, S.; Liu, Y.; Khodakov, A.; Bordes, E., *Catal. Today*, 2017, 298, 145−157.

[28] Chieregato, A.; Lo´pez Nieto, J. M.; Cavani, F., *Coord. Chem. Rev.*, 2015, 301−302, 3−23.

[29] Topsoe, N. Y.; Topsoe, H.; Dumesic, J. A., *J. Catal.*, 1995, 151, 226−240.

[30] Busca, G.; Lietti, L.; Ramis, G.; Berti, F., *Appl. Catal., B*, 1998, 18, 1−36.

[31] A. L. Godiksen, M. H. Funk, S. B. Rasmussen, S. Mossin, *Chem. Cat. Chem.,* 2020**,** 12, 4893-4903.

[32] A. Brückner, Chem. Soc. Rev. 2010, 39, 4673–4684.

[33] Vuong, T. H.; Radnik, J.; Rabeah, J.; Bentrup, U.; Schneider, M.; Atia, H.; Armbruster, U.; Grünert, W.; Brückner, A., *ACS Catal*., 2017, 7, 1693−1705.

[34] M. C. Paganini, L. Dall'Acqua, E. Giamello, L. Lietti, P. Forzatti, G. Busca, *J. Catal.* 1997, *166*, 195–205.

[35] P. J. Carl, S. L. Isley, S. C. Larsen, *J. Phys. Chem. A*, 2001, 105, 4563-4573

[36] Woodworth, J.; Bowman, M. K.; Larsen, S. C., *J. Phys. Chem. B*, 2004, 108, 16128−16134.

[37] Dinse, A.; Wolfram, T.; Carrero, C.; Schlögl, R.; Schomäcker, R.; Dinse, K.-P*., J. Phys. Chem. C,* 2013, 117, 16921−16932.

[38] Chiesa, M.; Meynen, V.; Doorslaer, S. V.; Cool, P.; Vansant, E. F., *J. Am. Chem. Soc*., 2006, 128, 8955−8963.

Chapter 2

Theory of EPR and NMR Spectroscopy

In this chapter the principles of Electron Paramagnetic Resonance (EPR) [1] and Nuclear Magnetic Resonance (NMR) [2] spectroscopies are introduced, along with the main experimental techniques used in this work. In the last part of the chapter, an overview of relaxation theory for paramagnetic systems is also given.

2.1 Basic Principles of Magnetic Resonance

The term resonance implies that the system is ''in tune'' with a natural frequency of the magnetic system, corresponding to the frequency of precession of the magnetic moment in an external magnetic, static field.
Both systems possess a magnetic moment μ and an angular momentum *J*. These two vectors are in fact correlated to each other so that we can write:

$$\mu = \gamma J \tag{2.1}$$

where *γ* is a scalar called gyromagnetic ratio.

In quantum theory, μ and *J* are treated as operators and the modulus of the electron and nuclear spin angular momentum are:

$$|\boldsymbol{I}| = \sqrt{I(I+1)} \tag{2.2}$$

$$|\boldsymbol{S}| = \sqrt{S(S+1)} \tag{2.3}$$

Where S and I are the electron and nuclear spin quantum numbers, respectively.

The magnetic moment of the nucleus can be now defined as:

$$\boldsymbol{\mu}_I = \hbar\gamma_I \boldsymbol{I} \tag{2.4}$$

where $\hbar = {}^{h}/_{2\pi}$ and h is the Planck's constant and γ_I is the nuclear gyromagnetic ratio, that depends on nuclear species.

Similarly, the electron magnetic moment can be written as:

$$\boldsymbol{\mu}_S = -\mu_b g \boldsymbol{S} \tag{2.5}$$

where $\mu_b = {}^{e\hbar}/_{2m_e}$ and m_e is the electron mass. The g is called *g*-factor; for free-electron the value is $g = 2.002319$.

When |α> and |β> states are considered, the potential energy of a magnetic dipole μ is given by $E = -\boldsymbol{\mu B}$, where $\boldsymbol{B}$ indicates the magnetic field. Moreover, E could assumed only the two values in case of application of a static magnetic field to the system:

$$E_I = \pm {}^1/_2 \, \gamma_I \hbar B_0 \tag{2.6}$$

$$E_S = \pm {}^1/_2 \, g|\mu_b|B_0 \tag{2.7}$$

This energy separation between the states is proportional to the strength of the field $\boldsymbol{B}_0$ and it provides the necessary condition for the observation of a spectral line both in NMR and EPR spectroscopy.

When a macroscopic sample is considered, it is needed to consider the distribution of the nuclei or the electrons in the ground and excited state. This phenomenon is described by the Boltzmann relations in function of temperature, that for nuclei and electrons is respectively express as:

$$\frac{N_\beta}{N_\alpha} = exp\left(\frac{-\Delta E}{kT}\right) = exp\left(\frac{-\gamma B_0}{2\pi kT}\right) \approx 1 - \frac{-\gamma B_0}{2\pi kT} \tag{2.8}$$

$$\frac{N_\alpha}{N_\beta} = exp\left(\frac{g_e|\mu_b|B_0}{k_b T}\right) \approx 1 - \frac{g_e|\mu_b|B_0}{k_b T} \tag{2.9}$$

where it is important to notice the in nuclei like protons this difference is only 0.002%, which means that for protons are like 20 nuclei in 10^6, while in the case of electrons the value is 1/1000 spins.

The total magnetization in a real sample is a vector obtained by sum the magnetic moments of the single spins directed along the B_0 field so $M_z = \sum \mu_{zi} = M_0$ and $M_x = M_y = 0$.

When the magnetization direction is changed by applying an external pulse, the following restoration of the equilibrium is described by the Bloch equations:

$$\frac{dM_z}{dt} = -M_y\omega_1 - {(M_z - M_0)}/{T_1} \quad (2.10)$$

$$\frac{dM_x}{dt} = M_y(\omega - \omega_0) - {M_x}/{T_2} \quad (2.11)$$

$$\frac{dM_y}{dt} = M_z\omega_1 - M_x(\omega - \omega_0) \quad (2.12)$$

where ω_0 is the offset frequency between the *Larmor frequency* and the rotating frame of reference.

The T_1 is called longitudinal or spin-lattice relaxation time and is related to the time for restoring the magnetization along the z-axis. The T_2, on the other side, is the transverse or spin-spin relaxation time that depends on how fast the M_x and M_y components lose their phasing.

2.2 The Spin Hamiltonian

The position and the shape of the EPR signal are determined by various interactions in the paramagnetic spin system. These interactions can be expressed in terms of the electron and nuclear spin angular momentum operators, which form the spin Hamiltonian of the system [3,4] where each term describes a specific interaction:

$$\mathcal{H} = \mathcal{H}_{EZ} + \mathcal{H}_{ZFS} + \mathcal{H}_{HF} + \mathcal{H}_{NZ} + \mathcal{H}_{NQ} \quad (2.13)$$

The first term is the electron Zeeman interaction and is expressed as:

$$\mathcal{H}_{EZ} = \frac{\mu_e \boldsymbol{B_0} g \boldsymbol{S}}{\hbar} \quad (2.14)$$

The *g*-factor depends on the orientation of the applied magnetic field with respect to the molecular framework, and is expressed as a tensor instead of a scalar quantity:

$$g = \begin{bmatrix} g_{xx} & 0 & 0 \\ 0 & g_{yy} & 0 \\ 0 & 0 & g_{zz} \end{bmatrix} \tag{2.15}$$

This *g*-tensor orientation reflects the symmetry of the electronic structure of the system, with three limit cases. The first is called cubic symmetry where $g = g_{xx} = g_{yy} = g_{zz}$, which means that the *g*-factor is completely isotropic. The second case is the axial one, characterized by $g_{\perp} = g_{xx} = g_{yy}$ and $g_{\parallel} = g_{zz}$. The last case is when the *g*-tensor is completely anisotropic and is call rhombic symmetry and is characterized by $g_{xx} \neq g_{yy} \neq g_{zz}$.

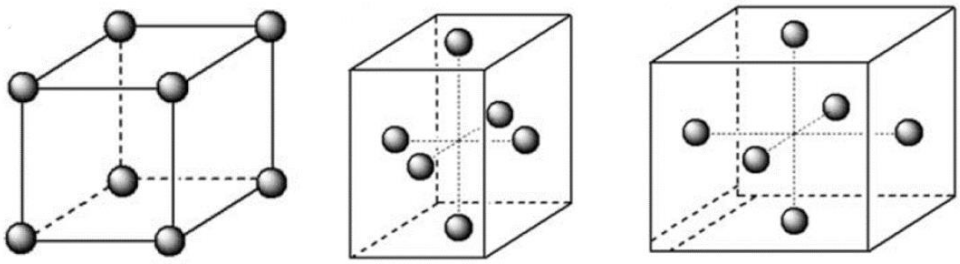

Figure 1: representation of cubic (left), axial (central) and rhombic (right) symmetry.

For a single crystal, the *g*-tensor can be obtained by recording CW EPR spectra for various orientations of the crystal axes with respect to the external magnetic field. On the other side, for polycrystalline samples, *i.e.* powder or frozen solution, the peak of the EPR spectrum corresponds to a

turning point on a spherical surface that shows the angular orientations in $\boldsymbol{B}_0$:

$$\frac{\delta B_{res}(\vartheta,\varphi)}{d\vartheta} = 0 \text{ and } \frac{\delta B_{res}(\vartheta,\varphi)}{d\varphi} = 0 \qquad (2.16)$$

In the case of axial symmetry system ($g_\perp = g_{xx} = g_{yy}$ and $g_\parallel = g_{zz}$) the *g*-tensor description become:

$$g(\vartheta) = (g_\perp^2 sin^2\vartheta + g_\parallel^2 cos^2\vartheta)^{1/2} \qquad (2.17)$$

While for a totally rhombic symmetry system the g-tensor is described as:

$$g(\vartheta,\varphi) = (g_{xx}^2 sin^2\vartheta cos^2\varphi + g_{yy}^2 sin^2\vartheta sin^2\varphi + g_{zz}^2 cos^2\vartheta)^{1/2} \qquad (2.18)$$

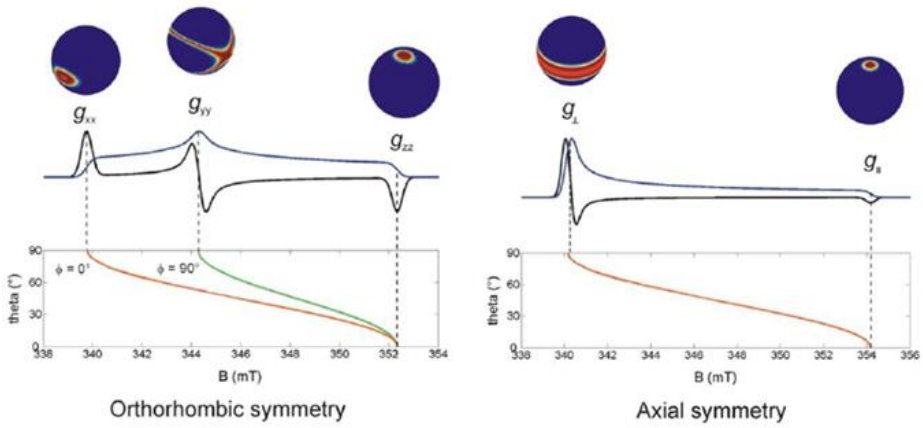

Figure 2: Absorption (blue line) and first derivative (black line) EPR spectra for S=1/2 spin system. For both systems, the angular dependency curve and the orientation selection spheres are shown.

The second term of the spin Hamiltonian (eq 2.13), related to the zero-field splitting, can be expressed as:

$$\mathcal{H}_{ZFS} = \boldsymbol{SDS} \tag{2.19}$$

that represents the interaction between two or more electron spins for $S > {}^{1}/_{2}$ systems.

The third term describes the interaction between an electron and nuclear spins in the local environment and is called hyperfine interaction:

$$\mathcal{H}_{HF} = \sum_{k=1}^{m} \boldsymbol{SA_k I_k} \tag{2.20}$$

where $\mathbf{A}$ represents the hyperfine matrix.

The hyperfine interaction is composed by two different components, the Fermi contact interaction and the electron-nuclear dipole-dipole anisotropic interaction.

The Fermi contact term is the isotropic one and is related mostly to electrons in an *s* orbital, due to the presence of electron spin density set on the nucleus:

$$\mathcal{H}_{iso} = a_{iso}\boldsymbol{SI} \tag{2.21}$$

Where $a_{iso} = \frac{8\pi}{3} g_e \beta_e g_n \beta_n |\Psi(0)|^2$ is the isotropic hyperfine coupling constant and $|\Psi(0)|^2$ is the electron spin density.

The dipolar interaction is also relevant for *p* and *d* orbitals and the anisotropic hyperfine interaction is written as:

$$\mathcal{H}_{DD} = \frac{\mu_0}{4\pi\hbar} g_e \beta_e g_n \beta_n \left[\frac{(3\boldsymbol{Sr})(\boldsymbol{rI})}{r^5} - \frac{\boldsymbol{SI}}{r^3}\right] = \boldsymbol{STI} \tag{2.22}$$

Where *r* is the distance between the electron and the nuclear spin and $\mathbf{T}$ is the traceless dipolar coupling matrix.

The hyperfine matrix ***A*** is the sum of the two terms:

$$A = a_{iso} + \boldsymbol{R}(\alpha,\beta,\gamma)\begin{bmatrix} T_x & 0 & 0 \\ 0 & T_y & 0 \\ 0 & o & T_z \end{bmatrix}\widetilde{\boldsymbol{R}}(\alpha,\beta,\gamma) \tag{2.23}$$

This, in the molecular frame term, becomes:

$$A = a_{iso} + \boldsymbol{R}(\alpha,\beta,\gamma)\begin{bmatrix} -T & 0 & 0 \\ 0 & -T & 0 \\ 0 & o & 2T \end{bmatrix}\widetilde{\boldsymbol{R}}(\alpha,\beta,\gamma) \tag{2.24}$$

The fourth term in EPR spin Hamiltonian is related to the nuclear Zeeman interaction, which describes the interaction of the nuclear spins with the magnetic field:

$$\mathcal{H}_{NZ} = -\beta_n \sum_{k=1}^{m} \frac{g_{n,k}\boldsymbol{B_0 I_k}}{\hbar} \tag{2.25}$$

In CW EPR spectra, however, this term is negligible because the allowed EPR transitions are only $|\Delta m_s| = 1, |\Delta m_I| = 0$.

The last Hamiltonian term represents the nuclear quadrupole interaction, which characterizes nuclei with $I > {}^1/_2$ that have a non-spherical charge distribution:

$$\mathcal{H}_{NQ} = \sum_{I_k > 1/2} \boldsymbol{I_k P_k I_k} \tag{2.26}$$

where P is the traceless quadrupole tensor. In the principal axes system, this interaction is described as:

$$\mathcal{H}_{NQ} = P_x I_x^2 + P_y I_y^2 + P_z I_z^2 = \frac{e^2 qQ}{4I(2I-1)\hbar}\left[3I_z^2 - I(I+1) + \eta(I_x^2 - I_y^2)\right] \tag{2.27}$$

So, the nuclear quadrupole tensor is written as:

$$P = \frac{e^2 qQ}{4I(2I-1)\hbar}\begin{bmatrix} -(1-\eta) & 0 & 0 \\ 0 & -(1+\eta) & 0 \\ 0 & 0 & 2 \end{bmatrix} \tag{2.28}$$

The asymmetry parameter $\eta = {(P_x - P_y)}/{P_z}$ with $|P_z| > |P_y| > |P_x|$ represents the deviation of the field gradient and $0 < \eta < 1$.

2.3 Pulse EPR Techniques

The use of pulse sequences is paramount in EPR spectroscopy as it allows to recover relevant information, which are not accessible via CW-EPR, by using similar principles used for the NMR sequences.

One of the most relevant aspects to consider, in case of electrons, is that T_1 and T_2 correlation times are usually very short at room temperature. So, to

observe the evolution of the magnetization, it is necessary to cool down the sample with a liquid helium set-up.

The are several experiments that depend on the shape and numbers of pulses, from which is possible to detect the local properties of the paramagnetic species analysed.

2.3.1 Echo Detected EPR

One of the simplest, but very informative, EPR technique is the Hahn Echo. It is composed by two pulses separated with a waiting time (τ) that permits the evolution of the magnetizations. [5]

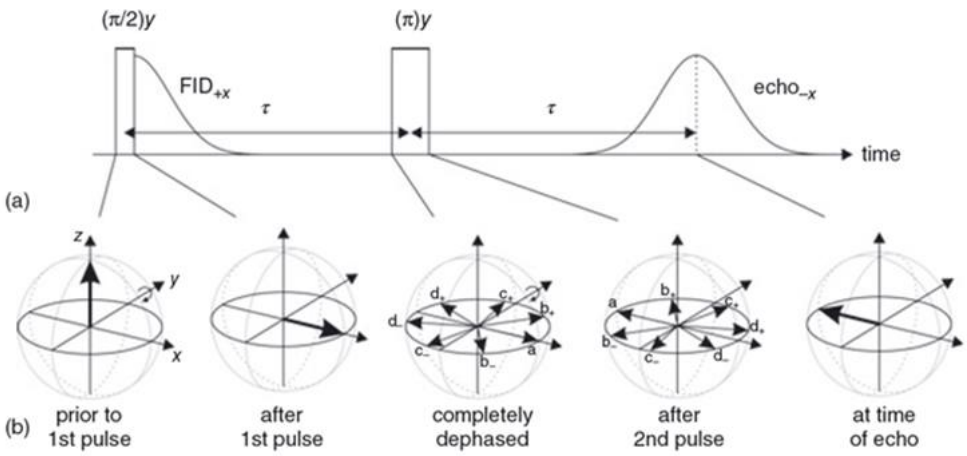

Figure 3: a) pulse sequence to the two-pulse echo. b) mechanism of formation of the two-pulse echo, in the rotating frame representation. [5]

The length of pulses typically used is about 16 and 32 ns with a τ equal to 200 ns, which is short enough to observe an absorption spectrum that

contains the information due to the presence of various species in the sample.

In some cases, it is possible to separate these contributions if the species are characterized by very different relaxation rates. So, by modulating the length of the waiting time it is possible to suppress the species with faster relaxation rates and observe the properties of the ones with slower rates.

2.3.2 Electron T_1 and T_2 Measurements

In general, relaxation is the process by which equilibrium is restored. Longitudinal relaxation is caused by fluctuating magnetic fields, which may have different origins, for example, the tumbling of a nearby spin. Transverse relaxation is an energy-free process that regards the dephasing of coherences, through the interaction with the environment.

It is possible to measure the longitudinal (T_1) a transverse (T_2) relaxation rates, at a specific field, by observing the evolution of the signal intensity as a function of time.

The measurements of T_1 is generally called inversion (Figure 4). It starts with a π pulse that inverts the populations, so the magnetization vector is antiparallel to the Z-axis, then there is a free evolution period, indicated with T. During τ the magnetization vector tends to its equilibrium i.e. along the Z-axis. Finally, a $\pi/2$ pulse is applied, and we obtain a signal proportional to M_z.

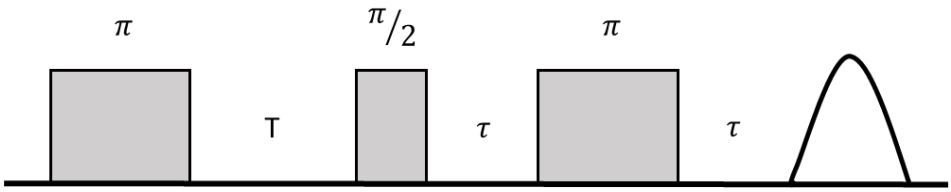

Figure 4: scheme of Inversion Recovery pulse sequence.

The T_2 spin-Echo sequence (Figure 5) starts with a $\pi/2$ pulse that rotates the magnetization in the xy plane along the y axis. Then, during τ, the different spin packets start precessing around z-axis direction with different frequencies depending on the local magnetic field. After that, a π pulse inverts the spin that continue their precession with the same frequency as before, but with an opposite phase. The last τ the spin are again refocusing along the y-direction.

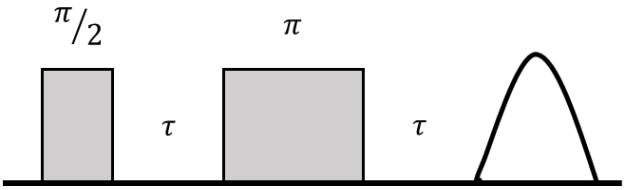

Figure 5: scheme of spin-Echo pulse sequence.

2.3.3 HYSCORE Spectroscopy

The hyperfine sublevel correlation spectroscopy (called HYSCORE) is a bi-dimensional technique that belongs to electron spin echo envelope modulation (ESEEM) spectroscopy. [6] It correlates the nuclear frequencies belonging to different electron spin states.

This sequence derives from the introduction of an intense π pulse between the second and the third pulse in the stimulated-echo sequence, so that the evolution period is split into two times intervals, t_1 and t_2, which vary progressively and independently. After the second $\pi/2$ pulse the nuclear spin system evolves according to the ENDOR frequencies ω_α or ω_β. The non-selective π pulse acts so that the population of the electron spin states β and α are inverted (the nuclear coherence between the electron-spin α and β manifolds are interchanged). This means that the nuclear coherence that had evolved according to ωα frequency before the π pulse, now evolve according to ω_β. Finally, the nuclear coherences are transferred to electron coherence by the last $\pi/2$ pulse and are detected as an electron-spin echo, which is modulated with the nuclear frequencies. By operating a double Fourier transformation with respect to t_1 and t_2, a bi-dimensional spectrum is obtained.

For $S = 1/2$ and $I = 1/2$ system, the spectrum shows correlation non-diagonal peaks at (ω_α,ω_β) and (ω_β,ω_α). The main advantage is the dispersion along the second dimension of the spectral peaks, avoiding the overlap of the small hyperfine or quadrupolar features that affect the mono-dimensional spectra. Each cross-peak represents a correlation between the frequency of a nucleus in an electron spin manifold (e.g. $m_S = 1/2$) and the same nucleus in another spin manifold (e.g. $m_S = -1/2$). Correlation peaks appearing in the (+,+) quadrant are attributed to nuclei in weak coupling regime, while correlation peaks in the (-,+) quadrant, on the other hand, are attributed to nuclei in strong coupling regime. The hyperfine parameters can be extracted from peak positions.

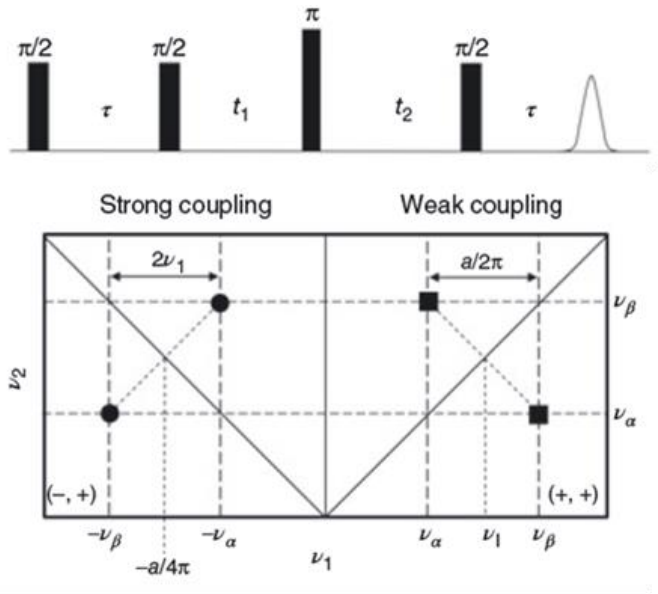

Figure 6: HYSCORE pulse sequence (up) and schematic representation of a HYSCORE spectrum for an S=1/2, I=1/2 system (bottom).

For disordered systems, like polycrystalline and frozen solution samples, the HYSCORE spectra are characterized by broad ridges instead of sharp cross-peaks because all molecular orientations are summed to obtain the recorded signals. So, again for $S = {}^{1}/_{2}$ and $I = {}^{1}/_{2}$, the hyperfine tensor is divided into two parts where the first part describes the isotropic contribution ${}^{a_{iso}}/_{2\pi}$, while the second one is the dipolar one ${}^{T}/_{2\pi}$. The maximum frequency shift is related to the dipolar component of the hyperfine tensor:

$$\Delta\upsilon_{S,max} = \frac{9T^2}{32(2\pi)^2|\upsilon_I|} \tag{2.29}$$

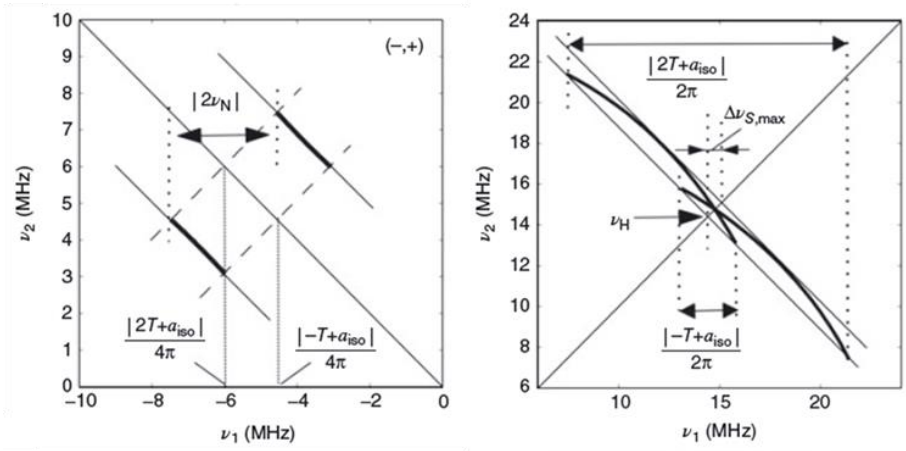

Figure 7: HYSCORE powder patterns for an S=1/2 I=1/2 spin system, the strong hyperfine coupling case (left) and weak hyperfine coupling case (right).

However, there are many cases where the electron spins interact with $I \geq 1$ nuclei and this increases the complexity of the spectra in terms of a higher number of nuclear spin states, but also because the nuclear quadrupole interaction is no more negligible. For $I = 1$, this effect can be expressed as:

$$\omega_{\alpha,\beta}^{DQ} = 2\sqrt{\left(\omega_I \pm \frac{a/2\pi}{4h}\right)^2 + \left(\frac{e^2qQ}{4h}\right)^2 (3+\eta^2)} \qquad (2.30)$$

Double quantum (DQ) cross-peaks are usually narrower than single quantum (SQ) cross-peaks: SQ nuclear frequencies have the first-order dependency on the nuclear quadrupole interaction, while DQ nuclear frequencies only depend on second order on this interaction. Consequently, DQ ridges are more intense.

2.3.4 ENDOR Spectroscopy

Electron-nuclear double resonance (ENDOR) spectroscopy is a method that allows the detection of the resonance frequencies of nuclei coupled to the electron spin. It consists of the excitation of the nuclear spin transition with an incident radiofrequency, which induces the intensity change of an EPR transition. The latter is in turn excited by a microwave pulse series. As the excitation range of the radiofrequency pulse is small (< 1 MHz), the whole NMR spectrum has to be recorded by sweeping the radiofrequency through the spectrum.

Davies ENDOR sequence [7] consists of a first π MW preparation pulse, which flips the electron Boltzmann population of the spin system. This justifies the observation of an inverted echo at the end of the sequence. A non-equilibrium spin state is thus produced, and it is detected thanks to the following echo sequence (Figure 8).

In a $S = {}^{1}/_{2}$ and $I = {}^{1}/_{2}$ spin system, after the preparation pulse an evolution period T follows, during which a radiofrequency pulse resonant with one of the ENDOR frequencies is applied. This determines the saturation of the EPR transition, with the consequent decrease of the echo intensity. When the radiofrequency is moved out of resonance for that specific ENDOR transition, the echo intensity is restored. The same phenomenon is repeated when the radiofrequency meets the resonance of the second NMR transition. The signal is then collected through the spin-echo detecting sequence.

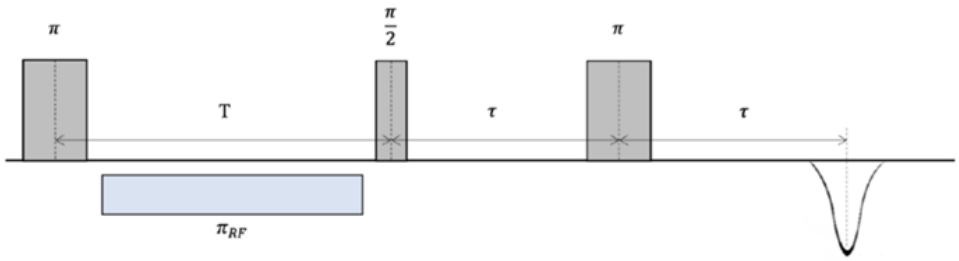

Figure 8: scheme of Davies-ENDOR sequence.

2.4 Paramagnetic Relaxation Theory

For paramagnetic molecular complexes is possible to investigate their properties with NMR relaxometry technique. [8,9]

This technique is based on relaxation effect due to the presence of the paramagnetic complex in solution:

$$R_{i(obs)} = \frac{1}{T_{i(obs)}} = \frac{1}{T_{i(diam)}} + r_i C \quad (2.31)$$

$$r_i = \frac{R_{i(obs)} - R_{i(diam)}}{C} \quad (2.32)$$

By rearranging the equation 2.31 is possible to obtain the parameter *r* called relaxivity, which is defined as the proton (^{1}H) relaxation rate of the water molecules in interaction with the paramagnetic entity, normalized to 1 mM concentration of the paramagnetic centre.

An important aspect that needs to be considered is that the $T_{i(obs)}$ is influenced by two different "types" of water molecules interacting with the paramagnetic system: the one in direct interaction (so-called inner-sphere water) and the other in close vicinity to the complex (called outer-sphere

water). It is possible to write separately the two components also for relaxivity: [10]

$$r_{1p} = r_{1p,is} + r_{1p,os} \tag{2.33}$$

The description of the inner-sphere relaxation phenomenon is defined by a set of equations under the 'collective name' of Solomon-Bloembergen-Morgan equations. In particular, the relaxation rate of the inner-sphere protons might be influenced by two different contributes, related to the dipole-dipole (DD) and the scalar (SC) interaction, as specified in the following equations: [11,12]

$$r_{1p,is} = \frac{1}{1000} \times \frac{q}{55.55} \times \frac{1}{T_{1m}^{H} + \tau_m} \tag{2.34}$$

$$\left(\frac{1}{T_{1m}^{H}}\right)^{DD} = \frac{2}{15}\left(\frac{\mu_0}{4\pi}\right)^2 \frac{{\gamma_I}^2 g^2 {\mu_B}^2}{{r_{VH}}^6} S(S+1)\left(\frac{3\tau_{d1}}{1+{\omega_I}^2{\tau_{d1}}^2} + \frac{7\tau_{d2}}{1+4{\omega_s}^2{\tau_{d2}}^2}\right) \tag{2.35}$$

$$\left(\frac{1}{T_{1m}^{H}}\right)^{SC} = \frac{2S(S+1)}{3}\left(\frac{A}{\hbar}\right)^2 \left(\frac{\tau_{e2}}{1+{\omega_S}^2{\tau_{e2}}^2}\right) \tag{2.36}$$

$$\frac{1}{\tau_{di}} = \frac{1}{\tau_R} + \frac{1}{\tau_m} + \frac{1}{T_{ie}}, \text{with } i = 1,2 \tag{2.37}$$

$$\frac{1}{\tau_{e2}} = \frac{1}{\tau_m} + \frac{1}{T_{ie}} \tag{2.38}$$

Where T_{ie} is the electronic spin relaxation time and $A/\hbar$ is the isotropic scalar coupling constant.

Similarly, the outer-sphere interaction describes the magnetic interaction between the paramagnetic complex and the water molecules that are moving in proximity to the complex: [13]

$$r_{1p,OS} = \frac{32N_A\pi}{405}\left(\frac{\mu_0}{4\pi}\right)^2 \frac{\hbar^2 {\gamma_S}^2 {\gamma_I}^2}{a_{VH}D_{VH}} S(S+1)[3J_{OS}(\omega_I;T_{1e}) + 7J_{OS}(\omega_I;T_{2e})] \quad (2.39)$$

$$J_{OS}(\omega_I;T_{je}) = Re\left[\frac{1+\frac{1}{4}\left(i\omega\tau_{VH}+\frac{\tau_{VH}}{T_{je}}\right)^{1/2}}{1+\left(i\omega\tau_{VH}+\frac{\tau_{VH}}{T_{je}}\right)^{1/2}+\frac{4}{9}\left(i\omega\tau_{VH}+\frac{\tau_{VH}}{T_{je}}\right)+\frac{1}{9}\left(i\omega\tau_{VH}+\frac{\tau_{VH}}{T_{je}}\right)^{3/2}}\right] \quad (2.40)$$

$$\tau_{VH} = \frac{{a_{VH}}^2}{D_{VH}} \quad (2.41)$$

where a_{VH} is the distance of closest approach of an outer-sphere water molecule to the vanadyl centre and D_{VH} is the relative translational diffusion coefficient.

Another important parameter is the rotational correlation time can be estimated with an empirical equation:

$$\tau_R = \frac{4\pi a^3 \eta}{3kT} \quad (2.42)$$

where a is the molecular radius (effective hydrodynamic radius of the molecular species) and η is the viscosity of the solvent.

Moreover, it is possible to use the EPR spectroscopy to obtain a very good approximation of τ_R by analysis of the linewidth of the complex in liquid solution spectrum, [14] that directly depends on the T_2 relaxation time:

$$\frac{1}{T_2} = A_0 + A + Bm_I + Cm_I^2 \quad (2.43)$$

Specifically, the A, B and C terms depend on rotational correlation time, while A_0 collects all other broadening effects.

$$A = \frac{\mu_e^2}{h^2} B_0^2 (\Delta g : \Delta g) \left[\frac{2}{15} j_0 + \frac{1}{10} j_1\right] + I(I+1)(\Delta A : \Delta A) \left[\frac{2}{15} j_0 + \frac{7}{60} j_1\right] \quad (2.44)$$

$$B = \frac{16\pi^2}{15} \frac{\mu_e}{h} B_0 (\Delta g : \Delta A) \left[\frac{5}{15} j_0 + \frac{1}{5} j_1\right] \quad (2.45)$$

$$C = (\Delta A : \Delta A) \left[\frac{1}{12} j_0 - \frac{1}{60} j_1\right] \quad (2.46)$$

Where $j_0 = \tau_R$ and $j_1 = {\tau_R}/{(1 + \omega_0^2 \tau_R^2)}$, on the other side, Δg and ΔA are the anisotropic parts of *g* and *A* tensors.

References Chapter 2

[1] M. Brustolon, E. Giamello, Electron Paramagnetic Resonance: Practitiorer's Toolkit, John Wiley & Sons, New Jersey, 2009.

[2] H. Günther, NMR Spectroscopy Basic Principles, Concepts, and Applications in Chemistry, Wiley, Weinheim, 2013.

[3] M. Bennati, D. M. Murphy, in Electron Paramagnetic Resonance: Practitiorer's Toolkit, John Wiley & Sons, New Jersey, 2009.

[4] N. M. Atherton, Principles of Electron Paramagnetic Resonance, Ellis Horwood, Chichester, 1993.

[5] Stefan Stoll, eMagRes, 2017, Vol 6: 23–38.

[6] Sabine Van Doorslaer, eMagRes, 2017, Vol 6: 51–70.

[7] E. R. Davies, Phys. Lett. 1974, 47A, 1.

[8] Jozef Kowalewski, Danuta Kruk, Paramagnetic Relaxation in Solution, eMagRes, 2011.

[9] Robert N. Muller, Contrast Agents in Magnetic Resonance: Operating Mechanisms, eMagRes, 2007.

[10] Delli Castelli D, Gianolio E, Aime S. Ed. Alessio E, Weinheim: Wiley-VCH, 2011.

[11] Solomon I, Bloembergen M., *J. Chem. Phys.*, 1956, 25, 261−266.

[12] Bloembergen N, Morgan LO., *J. Chem. Phys.*, 1961, 34, 842−850.

[13] Freed, JH., *J. Chem. Phys.*, 1978, 68, 4034−4037.

[14] Stefan Stoll, Arthur Schweiger, Biol. Magn. Reson. 2007, 27, 299-321.

Chapter 3

Materials and Methods

3.1 Materials Preparation

3.1.1 VO-TiO_2 Samples

The preparation of anatase TiO_2 support was done via sol-gel method (sg-TiO_2). Titanium (IV) isopropoxide was mixed with isopropyl alcohol and water in a 1:1:1 volumetric ratio and the solution stirred at room temperature for ~15 minutes to complete the hydrolysis. After this, the gel was left at room temperature for 20 hours, then dried overnight at 80 °C. Finally, the powder was calcined at 500 °C for 2 hours. The anatase $Ti^{17}O_2$ sample was prepared following the reported method. [1]

To study the role of surface geometry, shape engineered TiO_2 supports preferentially exposing the {101} or {001} facets were used). Both materials are provided by professor Maurino's group from Turin University and are synthesized as reported in literature. [2,3]

Vanadium ions were deposited on the TiO2 surface following different methods. Wet impregnation methods were used starting from sol-gel-TiO_2

powder suspended in water, in the presence of 0.5 ml of 0.2 M oxalic acid and containing 2.5 mg of NH_4VO_3. The suspension was stirred for 2 hours at room temperature, then the water excess was eliminated by using a water bath and dried overnight at 80 °C. Finally, the obtained powder was calcined at 400 °C for 5 hours.

The TiO_2 supports (sg-TiO_2, 001-TiO_2 and 101-TiO_2) and the impregnated sample (wi-TiO_2) are treated in an EPR-quartz cell, firstly in vacuum at 200 °C for 1 hour then after that, they were oxidized at 300 °C for 1 hour with 100 mbar of O_2.

The reaction in vapor phase with $VOCl_3$ and VCl_4 was carried out at room temperature by exposing the activated powder to the vapor of the two liquids and then the cell was outgassed to remove the excess of reagent and the reaction product, like HCl. For VCl_4 the grafting reaction was repeated several times the sending/outgassing cycle.

The wi-TiO_2 and $VOCl_3$-TiO_2 samples were reduced with 10 mbar NH_3 at 200 °C for 30 minutes, to obtain the active VO^{2+} species.

3.1.2 VO-ZSM-5 Samples

The H-ZSM-5 is a commercial sample prepared by Zeolyst with a Si/Al=40. The first step of preparation is treating the zeolite powder in an EPR-quartz cell at 400 °C for 2 hours in dynamic vacuum and after that, the sample is oxidized with 100 mbar of O_2 for 1 hour at 500 °C.

For the $^{16}O/^{17}O$ framework substitutions the activated powder was treated at 120 °C for 2 hours in presence of 20 mbar of $H_2{}^{17}O$, the procedure is repeated for 3/4 cycle.

As previously described for TiO_2 samples, the ZSM-5 activated powder was exposed to VCl_4 with the stepwise procedure.

3.1.3 Synthesis of VO-complexes

Vanadyls complexes were prepared in a water solution with a concentration of ~5 mM.

The $[VO(H_2O)_5]^{2+}$ complex was obtained by dissolving 8 mg of $VOSO_4$ in 10 ml of water at pH<2 with H_2SO_4, to avoid the oxidation from V^{4+} to V^{5+}.

For $VO(oxa)_2$ [4] and VO-nta [5] complexes the procedure is similar, with a nearly 1:1 molar ratio between metal ion and ligand in solution. 3 mg of nitrilotriacetic acid, or 3 mg of oxalic acid, were dissolved in 3 ml of water, then the pH was adjusted at about 5-6 pH units, with NaOH solution and, finally, 2.5 mg of $VOSO_4$ were added to the solution.

For the VO-dtpa complex (1:1 molar ratio), 10 mg of ligand were dissolved in 2.5 ml of water with 5 mg of $VOSO_4$, stirred for 1 hour and then the pH was regulated at 7 with 5% of $NAHCO_3$ solution. [6]

The $VO(acac)_2$ complex was prepared according to literature protocols. [7] V_2O_5 was dissolved in a 3:2 H_2O: H_2SO_4 (conc) solution. Then 5 ml of ethanol are added, and the resulting solution was heated at reflux temperature under stirring for 1 hour. The V_2O_5 excess was removed by filtration and acetylacetone was added under stirring at pH=7.

3.2 Experimental Methodologies

The vapor-phase reaction with VCl_4 or $VOCl_3$ was performed at room temperature, as schematically shown in Figure 1. The insert glass (made in quartz) permits selective isolation from the pumping system, such that the reaction with the two liquid reagents takes place in a controlled space. After that, the insert is again connected to the line by open the Teflon stopcock to outgas eventual residue from the cell.

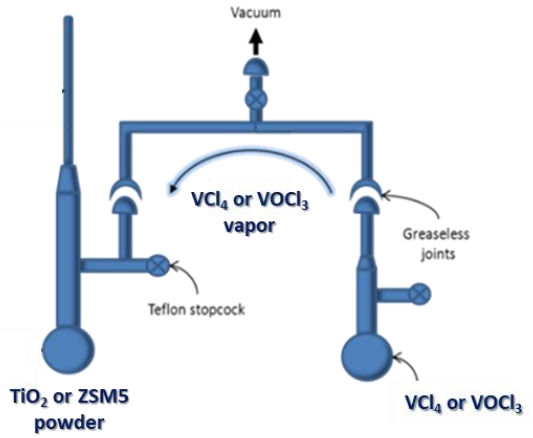

Figure 1: Schematic representation of the experimental set-up for the vapor-phase reaction.

The vacuum-line employed for all the samples treatments is equipped with a pump module generating a residual pressure of 10^{-4} mbar. The condensable gas at 77 K (NH_3) and the liquid reagents ($H_2{}^{17}O$, $VOCl_3$ and VCl_4) were employed after purification by the freeze-pump-thaw method.

For the Q-band pulse measures, the air-sensitive powder materials are transferred from the EPR cells into Q-band tubes inside a glovebox under a

controlled Argon atmosphere (O_2 < 1 ppm, H_2O < 1 ppm) and subsequently sealed with an acetylene torch, to avoid oxygen and water contamination.

For the EPR measurements of the VO-complexes in water solutions are used thin capillary, to reduce the interference due to the high dielectric constant of water. At low temperatures, it is needed to add 100 µl of glycerol, to obtain a good glass when the sample is frozen in liquid nitrogen.

The concentration of the complexes in solution is tested with Evans method [8] and the results are followed reported: $[VO(H_2O)_5]$=3.5 mM, [VO-dtpa]=1.8 mM, $[VO(oxa)_2]$=3.9 mM, [VO-nta]=12.2 mM and $[VO(acac)_2]$=14.1 mM. For pulse EPR measures the VO-nta and $VO(acac)_2$ are diluted to ~3 mM in order to have a similar concentration with the other complexes.

For the NMRD measures the solutions don't need particular treatment, apart for $VO(H_2O)_5$, where 0.2 M of $HClO_4$ are added to increase the stability of the complex, as suggested in literature. [9]

3.3 EPR Characterization Techniques

X-band CW-EPR spectra were detected on a Bruker EMX spectrometer (MW frequency 9.75 GHz) equipped with a cylindrical cavity.

X-and Q-band pulse EPR and Q-band CW EPR experiments were performed on a Bruker ELEXSYS E580 spectrometer (MW frequency 9.76 GHz and 34 GHz respectively) equipped with a continuous helium flow cryostat from Oxford Inc. The magnetic field was measured by means of a Bruker ER035M NMR gaussmeter.

Electron-Spin-Echo (ESE)-detected EPR experiments were carried out with the pulse sequence $\pi/2 - \tau - \pi - \tau -$ echo. The microwave pulse lengths $t_{\pi/2}$ and t_{π} and the τ value employed are specified in the corresponding figure captions.

T_m measurements were performed using a two-pulse Hahn spin-echo sequence, $\pi/2 - \tau - \pi - \tau -$ echo and varying the inter-pulse delay τ from an initial value of 120 ns with time increments of 8 ns for 800 points. The $\pi/2$ and π lengths were set to 16 and 32 ns, respectively.

T_1 measurements were performed through the inversion recovery pulse sequence, $\pi - T - \pi/2 - \tau - \pi - \tau -$ echo, where the inter-pulse delay T has an initial value of $1*10^5$ ns, $\pi/2$ and π has a length 16 and 32 ns respectively, and τ is fixed to 400 ns. The time increments of T and the shot-repetition rate were adjusted at each temperature.

Hyperfine sublevel correlation (HYSCORE) experiments were performed with the pulse sequence $\pi/2 - \tau - \pi/2 - t1 - \pi - t2 - \pi/2 - \tau -$ echo. A four-step (for experiments at X-band) or eight-step (for experiments at Q-band) phase cycle was used for eliminating unwanted echoes. The time traces of the HYSCORE spectra were baseline corrected with a third-order polynomial, apodized with a Hamming window, and zero-filled. After the two-dimensional Fourier transformation, the absolute-value spectra were calculated.

3.4 NMRD Measures

The Nuclear Magnetic Relaxation Dispersion (NMRD) profiles are performed in collaboration with Professor Botta research group at University of Piemonte Orientale.

The $^{1}/_{T_1}$ ^{1}H NMRD profiles were measured on a Fast-Field Cycling (FFC) Stelar SmarTracer Relaxometer over a continuum of magnetic field strengths from 0.00024 to 0.25 T (corresponding to 0.01-10 MHz proton Larmor Frequencies). The relaxometer operates under computer control with an absolute uncertainty in $^{1}/_{T_1}$ of ± 1%. Additional data points in the range 20-120 MHz were obtained with a High Field Relaxometer (Stelar) equipped with the HTS-110 3T Metrology Cryogen-free Superconducting Magnet. The measurements were performed using the standard inversion recovery sequence (20 experiments, 2 scans) with a typical 90° pulse width of 3.5 μs and the reproducibility of the data was within ± 0.5%. The temperature was controlled with a Stelar VTC-91 heater airflow equipped with a copper-constantan thermocouple (uncertainty of ± 0.1 K).

3.5 Density Functional Theory (DFT) Calculations

DFT calculations are performed by Professor Platas-Iglesias from University of A Coruña. DFT calculations were carried out with the Gaussian 16 program package (version B.01) [10] using the hybrid meta-GGA functional TPSSh [11] and the Def2-TZVPP [12] basis set. Bulk solvent effects (water) were

incorporated using a polarized continuum model (PCM) with default parameters using the scrf=pcm keyword in G16. [13] Geometry optimization was followed by frequency calculations, which corroborated that the optimized structures corresponded to local energy minima on the potential energy surfaces. The integration grid was augmented from the default values using the integral=superfinegrid keyword.

References Chapter 3

[1] Livraghi, S.; Chiesa, M.; Paganini, M. C.; Giamello, E., *J. Phys. Chem. C*, 2011, 115, 25413−25421.

[2] T. R. Gordon, M. Cargnello, T. Paik, F. Mangolini, R. T. Weber, P. Fornasiero, and C. B. Murray, *J. Am. Chem. Soc.,* 2012, 134, 6751-6761.

[3] V. Lavric, R. Isopescu, V. Maurino, F. Pellegrino, L. Pellutie`, E. Ortel, V.-D. Hodoroaba, *Cryst. Growth Des.,* 2017, 5640-5651.

[4] D. Sanna, I. Bódi, S. Bouhsina, G. Micera, T. Kiss, *J. Chem. Soc., Dalton Trans.*, 1999, 3275–3282.

[5] P. Buglyó, E. Kiss, I. Fàbiàn, T. Kiss, D. Sanna, E. Garribba, G. Micera, *Inorg. Chim. Acta,* 2000, 306, 174–183.

[6] J. W. Chen, R. L. Belford and R. B. Clarkson, J. Phys. Chem. A 1998, 102, 2117-2130.

[7] R. N. Rogers, G. E. Pake, *J. Chem. Phys*., 1960, 33, 4, 1107-1111.

[8] Daniele M. Corsi, Carlos Platas-Iglesias, Herman van Bekkum and Joop A. Peters, Magn. Reson. Chem. 2001; 39, 723–726.

[9] Ivano Bertini, Zhicheng Xia, Claudio Luchinat, J. Magn. Res., 1992, 99, 235-246.

[10] Frisch, M. J., Trucks, G. W., Schlegel, H. B., Scuseria, G. E., Robb, M. A., Cheeseman, J. R., Scalmani, G., Barone, V., Petersson, G. A., Nakatsuji, H., Li, X., Caricato, M., Marenich, A. V., Bloino, J., Janesko, B. G., Gomperts, R., Mennucci, B., Hratchian, H. P., Ortiz, J. V., Izmaylov, A. F., Sonnenberg, J. L., Williams-Young, D., Ding, F., Lipparini, F., Egidi, F., Goings, J., Peng, B., Petrone, A., Henderson, T., Ranasinghe, D., Zakrzewski, V. G., Gao, J., Rega, N., Zheng, G., Liang, W., Hada, M., Ehara, M., Toyota, K., Fukuda, R., Hasegawa, J., Ishida, M., Nakajima, T., Honda, Y., Kitao, O., Nakai, H., Vreven, T., Throssell, K., Montgomery, J. A., Jr., Peralta, J. E., Ogliaro, F., Bearpark, M. J., Heyd, J. J., Brothers, E. N., Kudin, K. N., Staroverov, V. N., Keith, T. A., Kobayashi, R., Normand, J., Raghavachari, K., Rendell, A. P., Burant, J. C., Iyengar, S. S., Tomasi, J., Cossi, M., Millam, J. M., Klene, M., Adamo, C., Cammi, R., Ochterski, J. W., Martin, R. L., Morokuma, K., Farkas, O., Foresman, J. B., Fox, D. J. Gaussian 16, revision B.01, Gaussian, Inc.: Wallingford, CT, 2016.

[11] Tao, J. M., Perdew, J. P., Staroverov, V. N., Scuseria, G. E., *Phys. Rev. Lett.*, 2003, 91, 146401.

[12] Weigend, F., Ahlrichs, R., *Phys. Chem. Chem. Phys*., 2005, 7, 3297−305.

[13] Tomasi, J., Mennucci, B., Cammi, R., *Chem. Rev*., 2005, 105, 2999−3093.

Chapter 4

Supported Vanadyl Species

4.1 The VO-TiO_2 System

Titanium dioxide is one of the most studied metal oxides as support in heterogeneous catalysis. The titanium oxide structure is characterized by three principal polymorphs: anatase, rutile and brookite, the first two being the two most frequently used in catalytic and photocatalytic applications.

Anatase titanium dioxide has a tetragonal ($D_{4h}^{19} - I4/amd$) structure with bulk cell dimensions equal to $a = b = 3.782$ Å, $c = 9.502$ Å, where Ti^{4+} ions present six-fold coordination. At the surface, in the case of anatase two main surface terminations, {001} and {101} facets are present. The {001} surface is basically flat, with Ti^{4+} ion in five-fold coordination. On the other hand, {101} facets show a bipyramidal geometry, where Ti^{4+} has four-fold or five-fold coordination depending on the atom position. [1] {101} terminations show the highest thermodynamic stability, while {001} TiO_2 forms sheets that tend to aggregate into a three-dimensional structure if heated at high temperature.

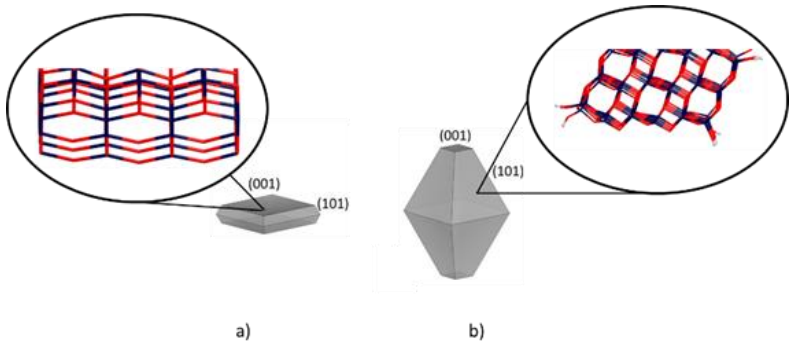

Figure 1: Two surface facets of TiO_2 (a) Square platelet morphology of anatase mainly exposing {001} facets. b) Truncated tetragonal bipyramid morphology of anatase dominated by {101} facets.

Titanium dioxide thus features its own reactivity, which may be increased and/or modified thanks to the presence of surface metal ions and, in particular, the different chemistry associated with specific anatase terminations also influence the structure and chemistry of supported metals. The geometric and electronic structures of supported oxo-vanadia species are highly sensitive to the structure of the oxide support. [2, 3, 4, 5]

The {101} are {001} surface terminations have been shown to accommodate monomeric oxo-vanadium species with different local coordination, which are retained in the two most common V oxidation states +5 and +4. [5, 6, 7] In order to get a molecular-level understanding of the role of the specific crystal facets in affecting the structure of supported transition metal ions featuring an open-shell electronic structure, EPR methodologies can be of high relevance since they can selectively probe, with high accuracy, the electronic and geometric structure of paramagnetic species.

It is also important to notice that VO/TiO_2, with Mo or W as co-catalyst, is largely used for the selective catalytic reduction (SCR) of NO_x in the presence of ammonia. Even though this catalyst has been industrially used for 50

years, many aspects concerning the nature of the catalytic active sites, reaction intermediates, and mechanisms are still debated. [8]

In this way, the application of pulse EPR methodologies to characterize the nature of surface V species on TiO_2 support generated by different precursors, NH_4VO_3 and $VOCl_3$, after reaction with ammonia, permits to investigate of the coordination environment metal and the nature of surface reaction intermediates. These experimental results were published during my first year of PhD. [9]

4.1.1 VCl_4-TiO_2 Experiments

The stepwise procedure for VCl_4 grafting (described in chapter 3.1.1) is followed with CW-EPR measures, to control the formation of vanadyl species on the surface of TiO_2 materials. In Figure 2 is possible to appreciate the progressive increase of the VO^{2+} signals, characterized by the typical pattern due to the anisotropic hyperfine coupling of the electron spin to the *I*=7/2 nuclear spin of ^{51}V (*I*=7/2, abundance 99.76%). This is particularly evident for the parallel components, where it is possible to observe two different main species, indicated with A and B, that shown different intensities depending on the TiO_2 surface geometry. It is interesting to notice that the spectral features of the monomeric VO^{2+} species remain unaltered starting from the first doses of VCl_4 up to the maximum loading and markedly depend on the nature of the specific TiO_2 support, i.e. on the exposed TiO_2 surface.

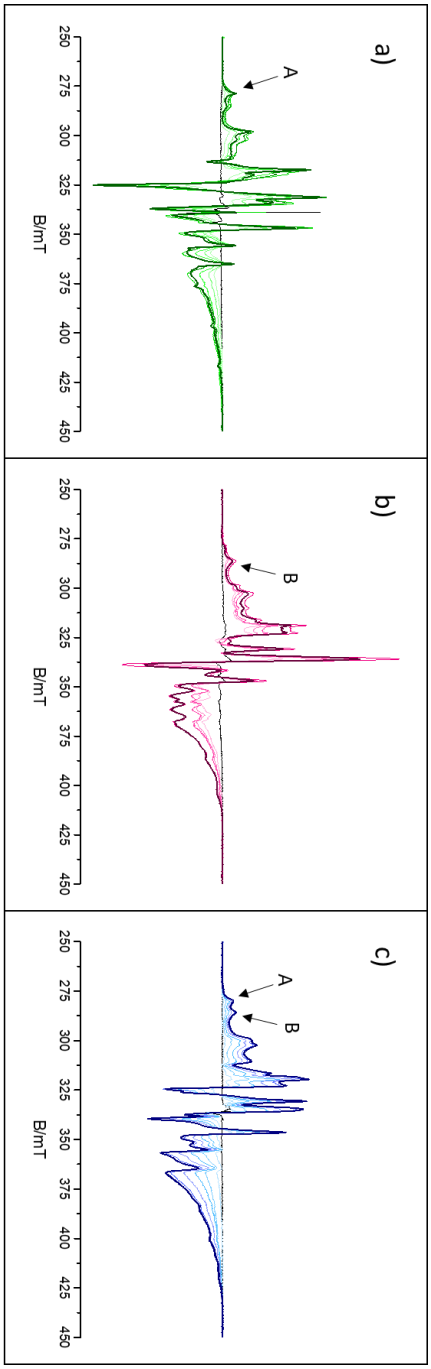

Figure 2: CW X-band EPR spectra of VCl_4 deposited at increasing doses on a) 001-TiO_2, b) 101-TiO_2 and c) sg-TiO_2. All spectra were recorded at 77 K, 1 mW power and 0.2 mT modulation amplitude.

The same procedure is used with the sol-gel TiO_2 enriched with ^{17}O (Figure 3), where it is possible to observe that the VCl_4 grafting is completely comparable with the sample without ^{17}O.

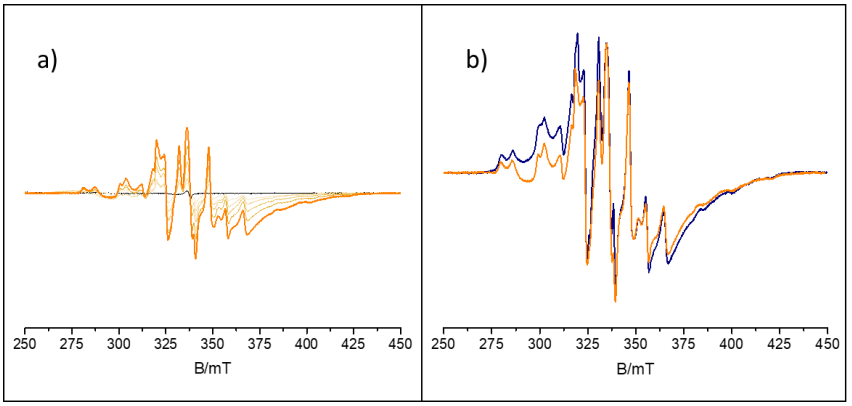

Figure 3: CW X-band EPR spectra a) of VCl_4 deposited at increasing doses on sg-$Ti^{17}O_2$ and b) the comparison with the sg-TiO_2 sample (blue spectrum).

The parameters obtained by computer simulation confirm the presence of three main species, A and B from the vanadyl sites on the TiO_2 facets and the last from V_2O_5 aggregates. It is important to notice that the set of *g* and *A* parameters, obtained from the simulation, well describe the VO-TiO_2 systems, by just changing the ratio between the three V components. The hypothesis that the V^{4+} species are effectively in vanadyls form is confirmed by calculating the $g_{iso} = (g_x+g_y+g_z)/3$ and $^{51}Va_{iso} = (A_x+A_y+A_z)/3$. The result for the two species A and B is g_{iso}(A) = 1.9663, g_{iso}(B) = 1.9634 and $^{51}Va_{iso}$(A) =|318| MHz and $^{51}Va_{iso}$(B) =|238| MHz and these values permit the discrimination between V^{4+} and VO^{2+}. [10]

Table 1: Spin-Hamiltonian parameters derived from the simulation of the VCl_4-TiO_2 samples.

Species	g_x	g_y	g_z	A_x	A_y	A_z	*(001)*	*(101)*	*Sol-gel*
VO^{2+} (A)	1.9834 ±0.0009	1.9834 ±0.0009	1.932 ±0.007	210 ±3	210 ±3	535 ±3	75%	4%	12%
VO^{2+} (B)	1.9743 ±0.0004	1.9610 ±0.0004	1.955 ±0.005	150 ±2	102 ±3	463 ±7	15%	19%	16%
aggregate	1.965±0.001			-	-	-	10%	77%	72%

In the following Figure 4 and Figure 5 are reported the experimental versus simulated spectra for X-band and Q-band experiments. In the simulations, the two species (A and B) are characterized by slightly different spin-Hamiltonian parameters. The intensity ratio of these two species reflects the relative abundance of the two dominant TiO_2 terminations. The A species is predominant in the case of the sample with dominant {001} exposed facets, while it is suppressed in the sample with prevailing {101} facets. Moreover, the two species have similar intensity in the sol-gel sample, where no facet selection is present. In addition, a broad background signal is observed and is associated with aggregated V^{4+} species, which is particularly evident in spectra recorded at Q-band frequency (Figure 5). It is evident that the intensity of this background is particularly pronounced in the case of the sol-gel and {101} faceted samples (Figure 4b and c, Figure 5b and c), while it is very limited for the {001} faceted sample (Figure 4a and Figure 5a). The limited contribution of the broad absorption in the TiO_2 sample with prevailing {001} facets compared to the other two samples suggests that metal clustering is inhibited on {001} facets.

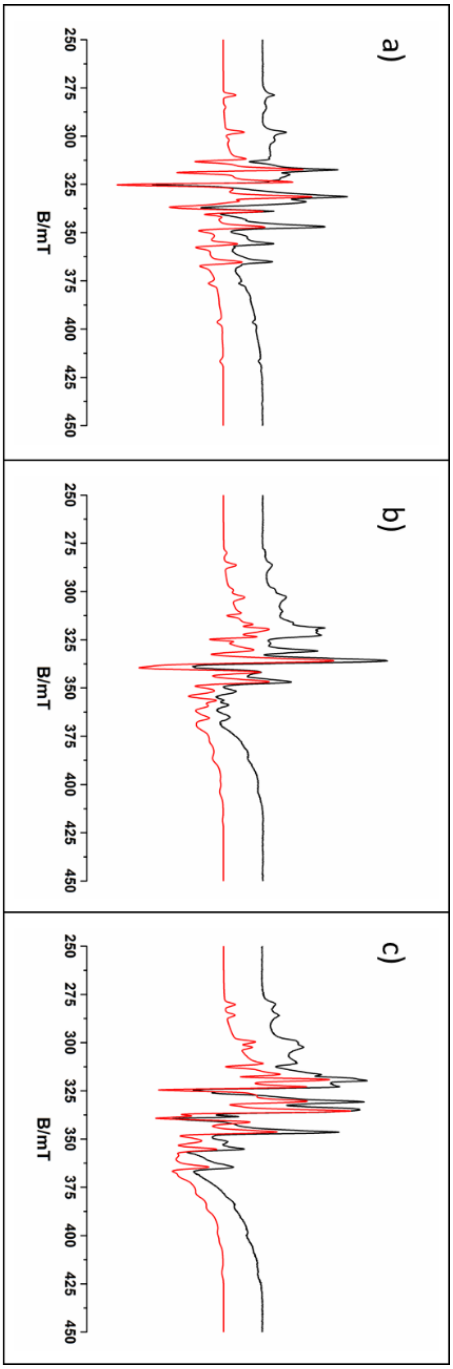

Figure 4: Experimental (black) and simulated (red) CW-EPR spectra of VCl_4-TiO_2 samples recorded at X-band frequencies of a) 001-TiO_2, b) 101-TiO_2 and c) sg-TiO_2l. All spectra were recorded at 77K.

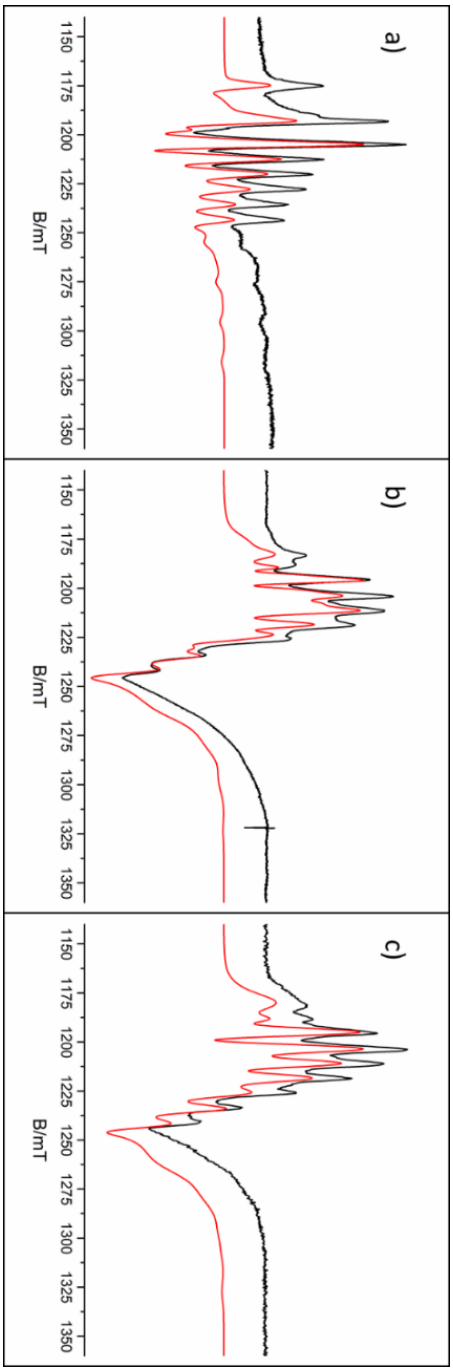

Figure 5: Experimental (black) and simulated (red) CW-EPR spectra of VCl_4-TiO_2 samples recorded at Q-band (d-f) frequencies of a) 001-TiO_2, b) 101-TiO_2 and c) sg-TiO_2. All spectra were recorded at 20 K.

To study deeply these three systems, advanced pulse EPR techniques were used.

In Figure 6 the Q-band echo detected spectra for the three samples are shown. The VCl_4-001-TiO_2 and VCl_4-101-TiO_2 samples present well-resolved spectra, with distinct peaks corresponding to the perpendicular components of the vanadium hyperfine coupling. On the other side, a far less resolved spectrum is observed for the VCl_4-sg-TiO_2 sample.

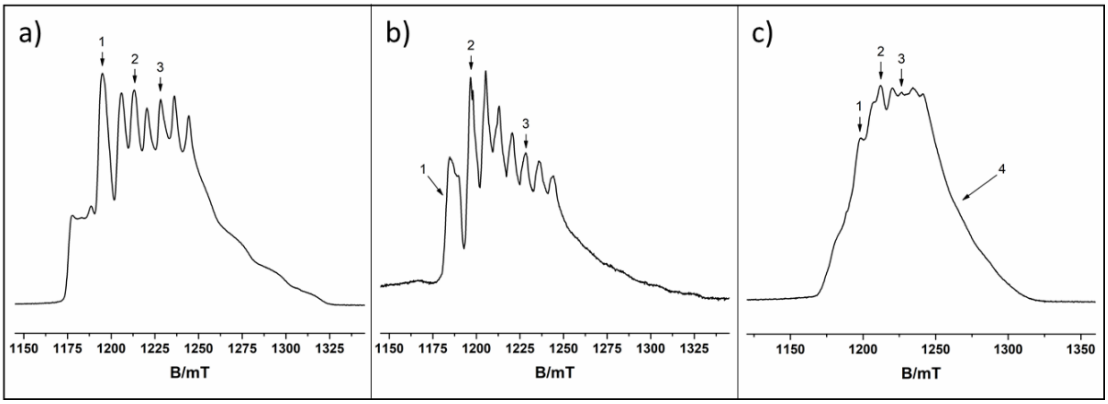

Figure 6: Q-band Echo detected EPR spectra of the VCl_4-001-TiO_2 (a), VCl_4-101-TiO_2 (b) and VCl_4-sg-TiO_2 (c) samples recorded at 25 K and τ= 200 ns. The numbers indicate the magnetic field settings at which ^{51}V HYSCORE experiments were carried out.

In Figure 7 and Figure 8 all the HYSCORE spectra for VCl_4-001-TiO_2 and VCl_4-101-TiO_2 samples are reported. In all spectra is possible to observe the cross-peaks centered at the vanadium Larmor frequency. The HYSCORE spectra present two well-resolved off-diagonal cross-peaks, instead of a “ridge” pattern. This indicates that the hyperfine interaction between the ^{51}V and the paramagnetic centre is dominated by the isotropic hyperfine contribute.

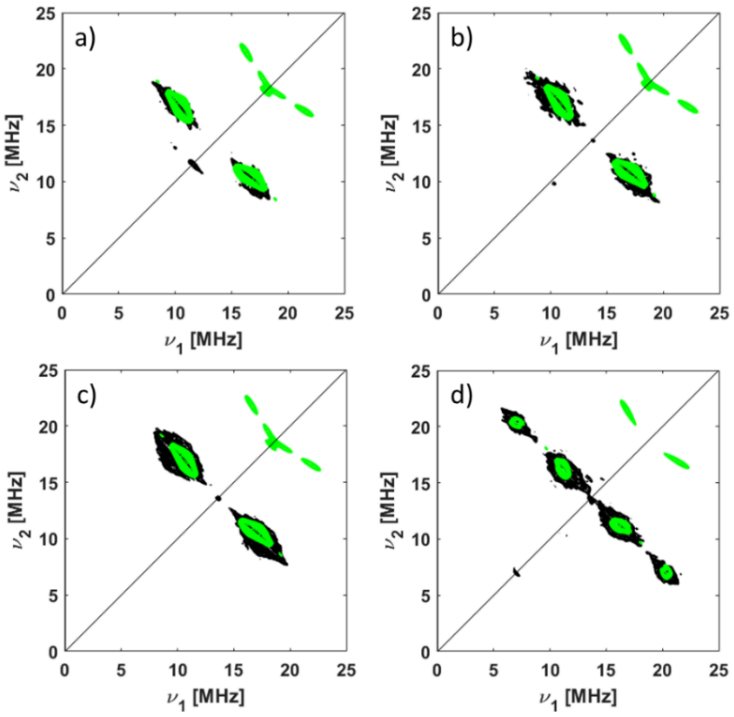

Figure 7: Experimental (black) and simulation (green) of ^{51}V Q-Band HYSCORE spectra of VCl_4-001-TiO_2 sample recorded at: a) position 1 (B_0=1195 mT) and τ= 144 ns, b) position 3 (B_0=1288.5 mT) and τ= 144 ns, c) position 2 (B_0=1215.6 mT) and τ=142 ns, d) position 2 (B_0=1215.6 mT) and τ=214 ns.

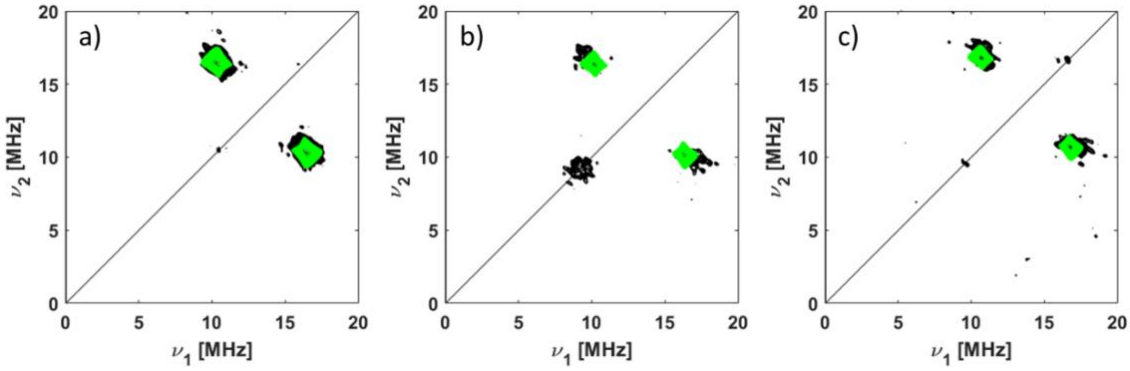

Figure 8: Experimental (black) and simulation (green) of ^{51}V Q-Band HYSCORE spectra VCl_4-101-TiO_2 sample recorded at: a) position 2 (B_0=1198.5 mT) and τ= 144 ns, b) position 1 (B_0=1184.8 mT) and τ= 144 ns, c) position 3 (B_0=1227.8 mT) and τ=144 ns.

Similarly, the VCl_4-sg-$Ti^{17}O_2$ HYSCORE spectra (Figure 9) show cross-peaks centered at the vanadium Larmor frequency. Moreover, it is possible to appreciate an additional signal, centred at the ^{17}O Larmor frequency (I=5/2), introduced by an isotopic enrichment process.

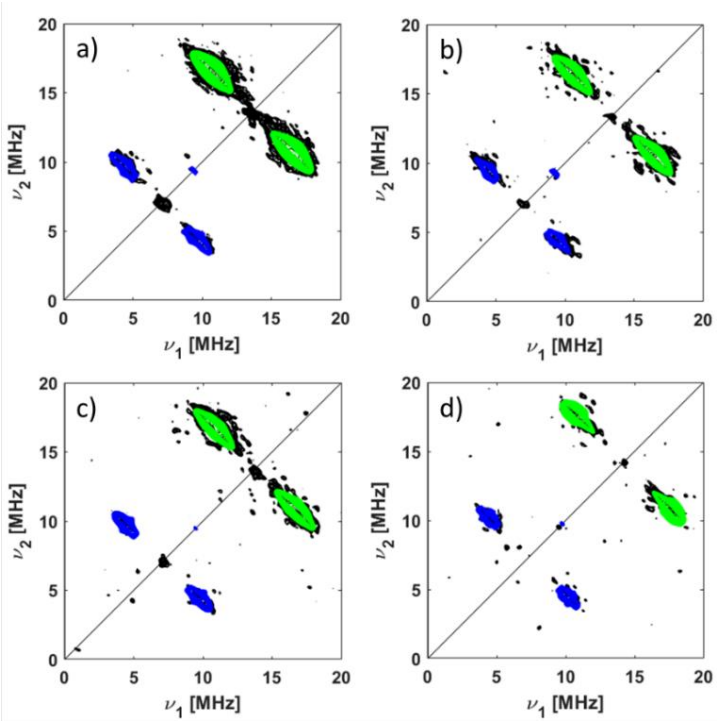

Figure 9: Experimental (black) and simulation (^{51}V green and ^{17}O blue) of Q-Band HYSCORE spectra of VCl_4-sg-TiO_2 sample recorded at: a) position 1 (B_0=1213.5 mT) and τ= 144 ns, b) position 1 (B_0=1200 mT) and τ= 144 ns, c) position 3 (B_0=1225.7 mT) and τ=142 ns, d) position 4 (B_0=1265 mT) and τ=214 ns.

In Table 2 are reported the spin Hamiltonian parameters obtained by the HYSCORE analysis. The ^{51}V cross-peaks of the VCl_4-001-TiO_2 sample (Figure 7) display an elongated shape, which can be reproduced by a_{iso}= 7 MHz and T= 3.5 MHz. These values correspond to a spin-transfer of the order of 3% considering the value of 4165 MHz and 125 MHz for unit spin density in the

4s and 3d orbitals of ^{51}V respectively. [11] A similar result is obtained from the analysis of the spectra recorded for VCl_4-sg-TiO_2 sample as shown in Figure 9. For VCl_4-101-TiO_2 sample, the parameter is quite different in fact, in this case, the shape of the cross-peaks shows a smaller elongation, which translates into a smaller dipolar component in the hyperfine coupling tensor and an a_{iso}= 6 MHz and T= 0.7 MHz. This significant reduction of the dipolar interaction could be an indication of a reduced spin density transfer in the 3d orbitals of the neighboring V nucleus, suggesting a different geometrical arrangement.

Isotropic hyperfine interaction arises from oxygen mediated through bond spin transfer, indicating the presence of V-O-V linkages. The spectral motif can be explained assuming that a fraction of the V^{4+} species interacts with oxidized (V^{5+}) covalently bound vanadium atoms, thus pointing to the presence of mixed-valence dimeric units at the surface like molecular $V_2O_3^{3+}$ species. [12] From the analysis of the ^{51}V HYSCORE spectra it is possible to appreciate that the major part of the electron spin density is concentrated at the V^{4+} centre, while the 3% is delocalized over the second V^{5+} nucleus. The spin delocalization mechanism over the two metal centres is well understood considering a through bond mechanism mediated by the bridging oxygen which is strongly dependent on the geometry of the V−O−V fragment.

Table 2: Spin Hamiltonian parameters derived from the simulation of the HYSCORE experiments of VCl_4-TiO_2.

Sample	Nuclei	A_x	A_y	A_z	Euler angle α,β,γ	e^2qQ/h	η	Euler angle α',β',γ'
Sol-gel	^{17}O	3.9 ±0.1	3.9 ±0.1	7.2 ±0.1	-	-	-	-
	^{51}V	2.8 ±0.2	2.8 ±0.2	8.8 ±0.2	0, 30±5, 0	1±0.2	-	-
(001)	^{51}V	3.7 ±0.2	3.7 ±0.2	14.1 ±0.2	0, 70±5, 0	1.2±0.2	-	0, 50±5, 0
(101)	^{51}V	5.5 ±0.2	5.5 ±0.2	7 ±0.2	0, 60±5, 0	1.3±0.2	-	0, 60±10, 0

For ^{17}O hyperfine interaction in the VCl_4-sg-$Ti^{17}O_2$ sample, the Fermi contact (a_{iso}) term is around 5 MHz and the anisotropic coupling tensor is T = [-1.1±0.5 -1.1±0.5 +2.2±0.5] MHz. This value is in line with the one reported in the case of V/ZSM-5 [13], which will be discussed in the last part of this chapter, and with the values reported for pentaquo vanadyl molecular complexes. [14,15] Such a small ^{17}O hyperfine coupling reflects the non-bonding character of the d_{xy} orbital hosting the unpaired electron and its limited overlap with the p_x oxygen orbital, in line with the localized character of the unpaired electron on one of the two metal centers of the V^{4+}-O-V^{5+} fragment.

4.1.2 The Interaction of Surface VO-species with Ammonia

The samples prepared with $VOCl_3$ and NH_4VO_3 present vanadyl sites in V^{5+} state so, with respect to the experiments done with VCl_4, reduction with NH_3 at 200°C was needed to obtain paramagnetic V^{4+} species.

In Figure 10 the EPR spectra of vanadium-containing sample, obtained by wet impregnation (wi-sg-TiO_2) are shown. Prior to reduction only a minor EPR signal is observed, possibly due to a minute fraction of V^{4+} species present on the surface. (Figure 9a).

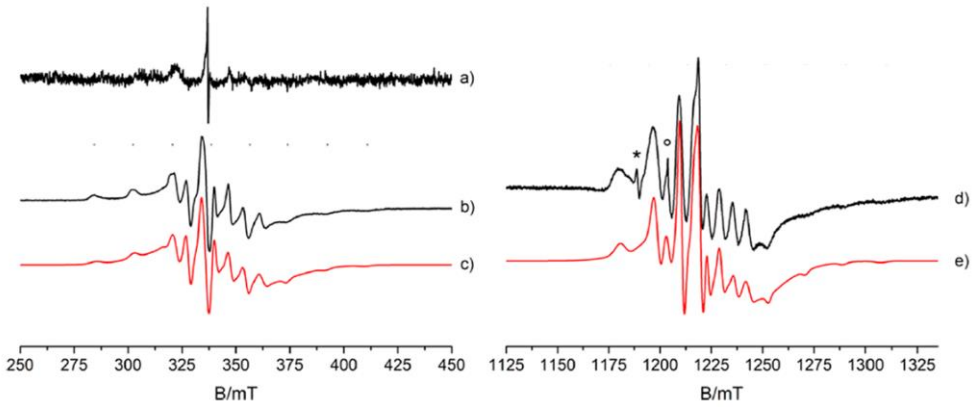

Figure 10: CW spectra at X-band (a, b) and Q-band (d) with simulations (c, e) of sg-TIO_2 impregnated sample. Figure adapted from reference. [9]

After the reduction step with ammonia, the EPR spectrum is characterized by an intense signal amenable to isolated VO^{2+} ions in square-pyramidal coordination. The simulation parameters are reported in Table 3 and confirm the presence of a VO^{2+} species with axial symmetry. Like the systems described previously, also in this sample is possible to appreciate a quite high

content of V_2O_5 aggregates. A peculiar characteristic of the wi-sg-TiO_2 sample is the presence of a small amount of reduced Ti^{3+}, confirmed by pulse ESE measurements, with the typical *g*-factor for surface Ti^{3+} in the anatase sample. [16]

Table 3: Spin-Hamiltonian parameters derived from the simulation of the wi-sg-TiO_2 sample.

Species	g_x	g_y	g_z	$\|A_x\|$	$\|A_y\|$	$\|A_z\|$	**Weight**
VO^{2+}	1.9745 ±0.0006	1.9745 ±0.0006	1.938 ±0.002	173±5	173±5	490±10	13.2
aggregate	1.96±0.01			-	-	-	84.8
Ti^{3+}	1.967 ±0.001	1.967 ±0.001	1.89 ±0.01	-	-	-	<2

Similarly, in Figure 11 are reported the spectra for the TiO_2 sample contacted with $VOCl_3$ vapours. It is possible to see in Figure 11a that the interaction between the vapor phase of $VOCl_3$ and the supports generates a partial reduction of vanadyl in V^{4+} species. In the following step of reduction with ammonia, the signals related to isolate VO^{2+} species increase and, correspondingly, the V_2O_5 aggregates signal increase. Moreover, it is interesting to notice that in case of $VOCl_3$-001-TiO_2 sample the formation of VO^{2+} is not significant, instead the aggregates dominate the spectrum (Figure 11b).

The $VOCl_3$-101-TiO_2 and the $VOCl_3$-sg-TiO_2 present a similar spectrum and this evidence is confirmed by the spin-Hamiltonian parameters reported in Table 4. The *g*- and *A*-factors of the main VO^{2+} species for the two samples present very close values and this seems to confirm the stability of the {101} facet respect the {001} one after reduction with ammonia. In particular, in

the case of the $VOCl_3$-sg-TiO_2 system, it is possible to appreciate a second species with lower abundance and similar spin Hamiltonian parameters, which possess slightly orthorhombic vanadium *g*-factor and A^V hyperfine coupling tensors. This can be indicative of a lower symmetry respect C_{4v} and a slightly different local environment with respect to the impregnated sample.

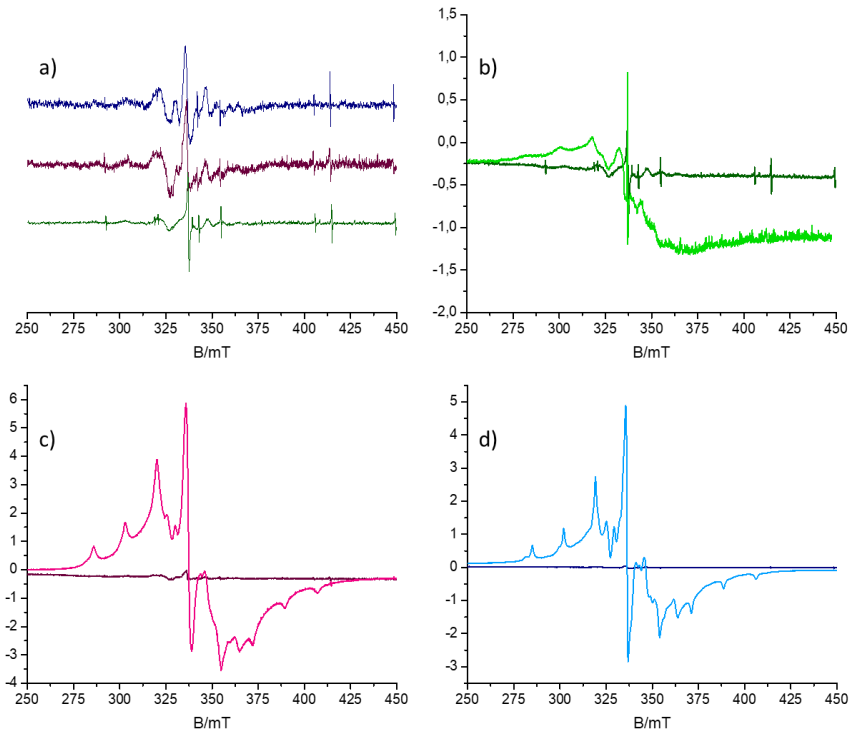

Figure 11: CW X-band $VOCl_3$-TIO_2 spectra at 77K of a) after $VOCl_3$ vapour deposition (spectra normalized), b-d) reaction with NH_3 at 200 °C for 30 minutes at sg-TiO_2 (green), 101-TiO_2 (purple) and 001-TiO_2 (blue).

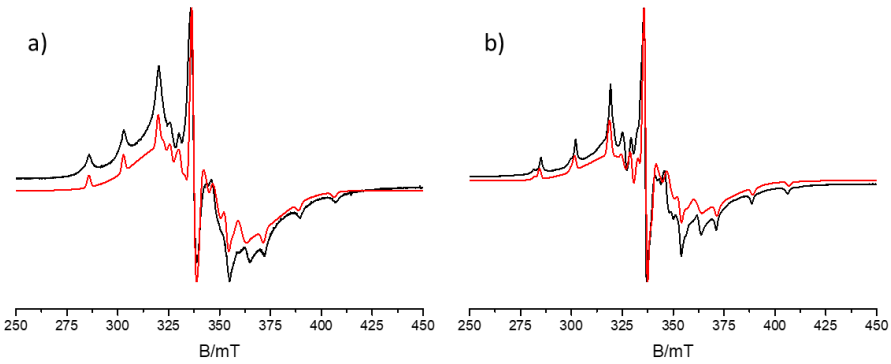

Figure 12: CW X-band simulations of $VOCl_3$ spectra a) 101-TiO_2 and b) sg-TiO_2.

Table 4: Spin-Hamiltonian parameters derived from the simulation of the $VOCl_3$-TiO_2 samples.

Sample	Species	g_x	g_y	g_z	A_x	A_y	A_z	Weight
Sol-gel	VO^{2+} (1)	1.9510 ±0.0006	1.9731 ±0.0006	1.948 ±0.002	140±5	150±5	472±5	12%
	VO^{2+} (2)	1.962 ±0.004	1.99 5±0.004	1.945 ±0.002	158±5	135±5	500±10	4.2 %
	Aggregate	1.965±0.001			-			83.8 %
(101)	VO^{2+}	1.9562	1.9747	1.9495	-135	-140	-470	10 %
	Aggregate	1.965±0.001			-			90 %

The same spin Hamiltonian parameters are also used for the simulation of the ESE-EPR X-band spectra of wi-sg-TiO_2 (Figure 13a) and $VOCl_3$-sg-TiO_2 (Figure 13b) samples.

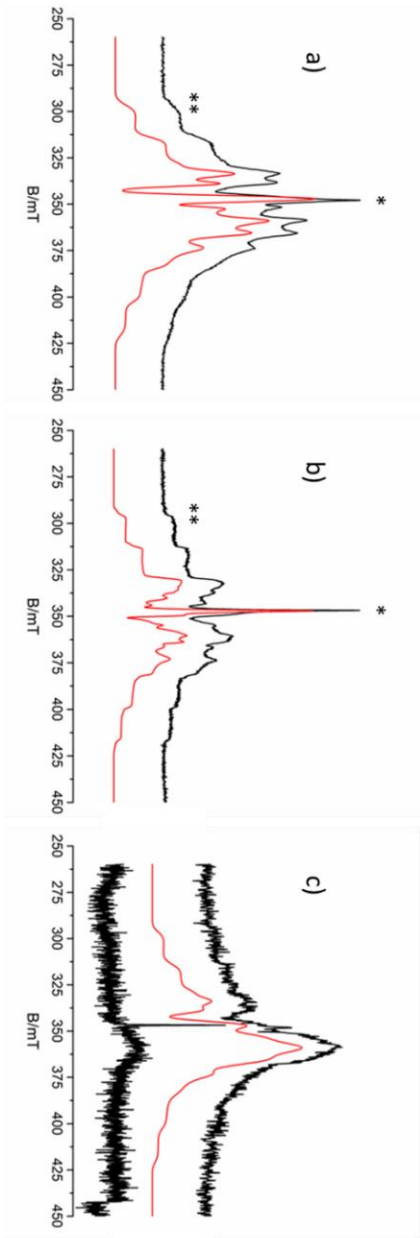

Figure 13: Experimental (black) and simulated (red) X-band ESE-EPR spectra at 15 K of a) wi-sg-TiO_2 recorded after reaction with ammonia at 200 °C with τ=200 ns, b) $VOCl_3$-sg-TiO_2 recorded after reaction with ammonia at 200°C with τ=200 ns and c) wi-sg-TiO_2 (top spectrum) and $VOCl_3$-sg-TiO_2 (bottom spectrum) with τ=4000 ns. The asterisks represent the fields where are measured the HYSCORE spectra (* for the "powder position" and ** for the "single crystal" one). Figure adapted from reference. [9]

In Figure 13c is reported the ESE spectra with τ=4000 ns that confirms the presents of Ti^{3+} on the surface of the wi-sg-TiO_2 sample. This is because, respect to vanadyl species, Ti^{3+} species is characterized by a very long phase memory time. This reveals that, for the impregnated sample, the surface of TiO_2 is involved in the redox cycle related to ammonia reduction on V_2O_5/TiO_2. On the other side, in $VOCl_3$-sg-TiO_2 sample, seems that the surface is less involved.

The HYSCORE spectra of wi-sg-TiO_2 (Figure 14) and $VOCl_3$- sg-TiO_2 (Figure 15) showed a strong interaction of the paramagnetic centers with ^{14}N nuclei. In the case of a nucleus with nuclear spin *I*=1, the M_s manifold is splits in three nuclear frequencies each and this leads to the presence of cross-peaks in (-,+) and (+,+) quadrants. So, it is possible to observe the single-single quantum transition, with $\Delta M_I \pm 1$, centered at (−1.7, 3.5) and (−3.5, 1.7) MHz. Moreover, the most intense cross-peaks centered at (−3.5, 6.9) and (−6.9, 3.5) MHz are assigned to the double-double quantum transition, $\Delta M_I \pm 2$, and the third pair of cross-peaks, (−1.7, 6.9) and (−6.9, 1.7) MHz, to the single-double quantum transitions. In the HYSCORE spectra of wi-sg-TiO_2 is also possible to appreciate a small residue of ^{51}V, graphically represented with the blue antidiagonal line that corresponds to the ^{51}V Larmor frequency.

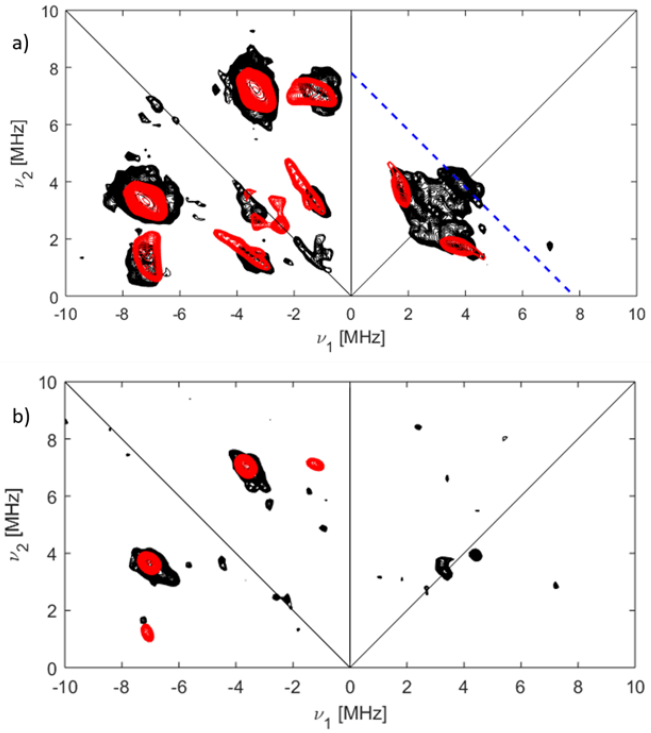

Figure 14: Experimental (black) and simulated (red) HYSCORE spectra of the wi-TiO_2 sample reduced with NH_3. a) spectrum recorded at, B_0=347.4 mT with τ=170 ns and b) spectrum recorded at B_0=299.0 mT and τ =118 ns. All spectra were recorded at T= 35 K. Figure from reference. [9]

The same considerations about ^{14}N are valid also for the $VOCl_3$- sg-TiO_2 sample (Figure 15) but, in this case, only the double-double transition is visible. This is caused by $^{35,37}Cl$ interaction that arises in the (+,+) quadrant, which induces suppression of the single-single and single-double transition of ^{14}N. This Cl hyperfine interaction indicates that the hydrolysis reaction between the surface hydroxyl groups and $VOCl_3$ is incomplete, so the surface vanadium species had a partially chlorinated environment.

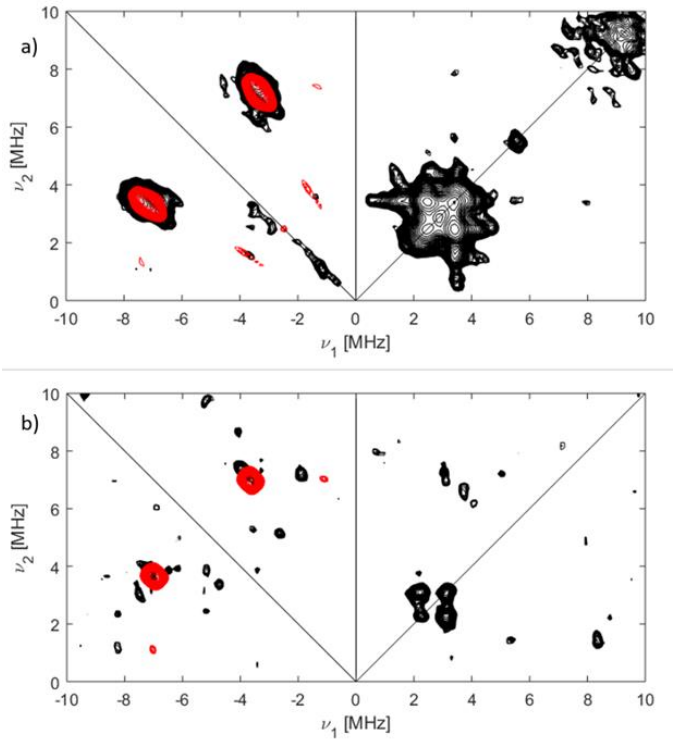

Figure 15: Experimental (black) and simulated (red) HYSCORE spectra of the $VOCl_3$-TiO_2 sample reduced with NH_3. a) spectrum recorded at, B_0=346.1 mT with τ=172 ns and b) spectrum recorded at B_0=294.9 mT and τ =100 ns. All spectra were recorded at T= 15 K. Figure from reference. [9]

Additionally, the wi-sg-TiO_2 sample also shown a hyperfine coupling with a proton that is reported in Figure 16. It is possible to observe a prominent bridge that can be simulated with a single type of proton nuclei.

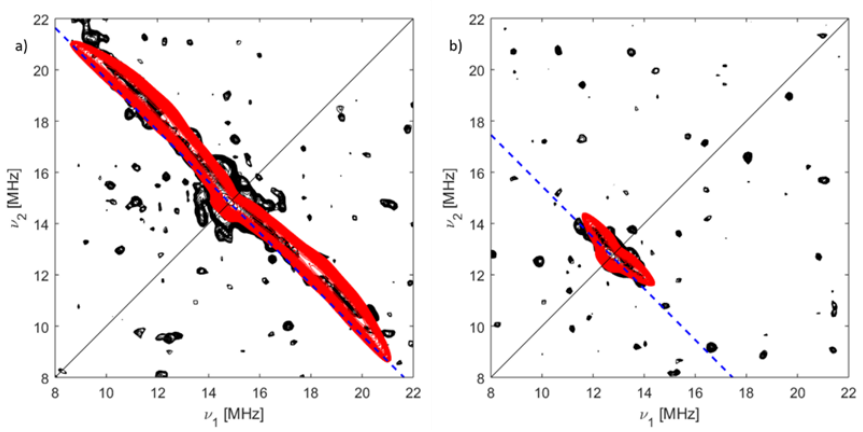

Figure 16: ^{1}H HYSCORE spectra recorded on the V impregnated sample, after reaction with NH_3. a) spectrum recorded at, B_0=347.4 mT and b) spectrum recorded at B_0=294.9 mT. The spectra were recorded at T= 15 K. In the figure, spectra recorded at two τ values (100 ns and 170 ns) have been added together after Fourier transform, to eliminate blind spot effects. Simulated spectra are in red. Figure from reference. [9]

In Table 5 are summarized the parameters used for the simulation of the HYSCORE experiments. It is interesting to notice that, for ^{14}N nuclei, the same spin Hamiltonian parameters well-describe both the systems.

Table 5: Spin Hamiltonian parameters from the simulation of the HYSCORE experiments for wi-sg-TiO_2 and $VOCl_3$-sg-TiO_2.

Sample	**Nuclei**	A_x	A_y	A_z	**Euler angle** α,β,γ	e^2qQ/h	η	**Euler angle** α',β',γ'
wi-TiO_2	^{14}N	4.35 ±0.05	4.35 ±0.05	5.25 ±0.05	43±15	2.45±0.05	80±20	-
$VOCl_3$-TiO_2								
wi-TiO_2	^{1}H	-0.6 ±0.05	-0.6 ±0.05	13.2 ±0.1	80±10	-	-	

The interaction with ^{14}N nuclei, in both samples, is similar to others described in literature [17,18] for nitrogen moieties in equatorial coordination.

Computer simulation of the orientation selective HYSCORE spectra (Figure 16) shows that the proton ridge can be reproduced assuming the interaction of the unpaired electron with a single type of ^{1}H nuclei. The contribution of remote protons was neglected, and attention was paid to reproduce the main features of the elongated ridge. The β-angle between the g_{zz} axis (assumed to coincide with the V=O bond) and the principal $^{H}A_{zz}$ axis is in the range 70-90°, pointing to an axially coordinated proton. The hyperfine coupling constants deduced from the simulation are reported in Table 5. Considerations based on quantum chemical calculations and single-crystal ENDOR data for $[VO(H_2O)_5]^{2+}$ indicate that the parallel principal proton hyperfine value is large and positive. Following these guidelines, the isotropic and dipolar components of the ^{H}A matrix can be obtained corresponding to a_{iso} = 4 MHz and T = 4.6 MHz. Considering a purely dipolar interaction the V-H distance can be estimated to be 0.26 nm. Protons at this distance are clearly attached to atoms directly ligated to the V^{4+} ion and may be associated with the directly coordinated ammonia. [19] However, we note that an alternative possibility is associated with the presence of an equatorially bound OH- group formed during the redox process (scheme 1).

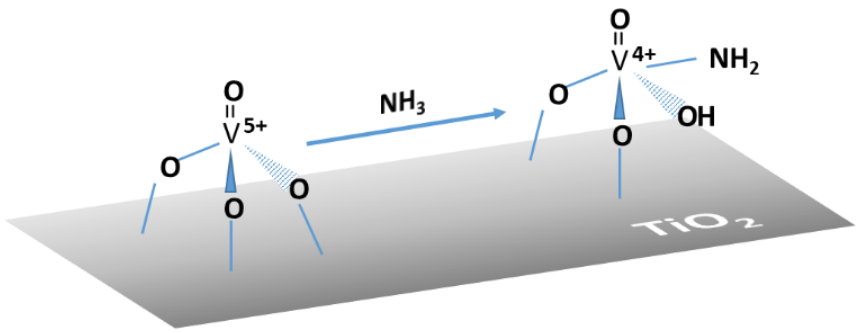

Scheme 1: schematic representation of the structure of the vanadyl species after reaction with ammonia, emerging from the EPR and HYSCORE experiments.

4.2 Vanadium Exchanged H-ZSM-5 Prepared by Vapor Reaction of VCl_4

Zeolites are a class of aluminosilicate porous materials, characterized by a regular and uniform distribution of pores in their structures. More than 200 zeolitic structures are known, which are described by different parameters, as pore size or pore shape.

The zeolites framework is formed by assembly of tetrahedral elementary units (SiO_4^{4-}) that can be linked together by their corners in order to form firstly rings, and then cages, cavities and channels with different spatial arrangements.

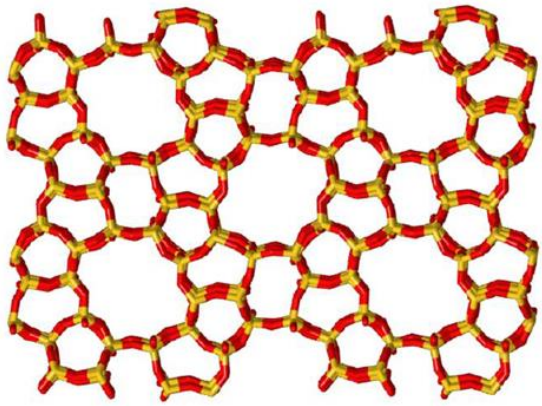

Figure 17: representation of ZSM-5 structure.

During synthesis, Si^{4+} can be replaced by Al^{3+} in an isomorphous substitution, that generates a local charge imbalance that is compensated by the presence of H^+, or another monovalent cation. Unfortunately, this makes zeolites with high Al content thermally and chemically unstable. On the

other side, the acid character of the material depends on the Si/Al ratio and it influences the catalytic properties of the final material. For example, a high number of hydroxyl groups on their surface determines a marked hydrophilic character. This peculiarity strongly affects their reactivity since the hydrated form is their starting condition when they are exposed to the atmosphere.

Another interesting aspect is concerned with the presence of extra-framework ions, which can infer redox functionalities on top of the acid properties of the material. These transition metal ions can be introduced under various forms: supported extra-framework exchanged cations, supported metal clusters, supported metal oxides, complexes, or as lattice cations. This allows reaching two goals: the specific redox properties of the metal ions, by their different oxidation states, and the shape-selective environment by the zeolitic structure.

In the case of paramagnetic ions in the zeolite structure, the use of EPR permits a deep study of the metal atom-oxide interaction, especially with pulse-EPR techniques that allows detecting the hyperfine interaction in the local environment of the paramagnetic active site. However, the oxygen is mainly EPR silent, the magnetically active oxygen isotope ^{17}O (I=5/2) has a natural abundance of 0.037%, therefore it is mandatory to employ ^{17}O isotopic enrichment strategies to investigate the hyperfine structure of the site, based on the work of Morra et al. with Zn^{+} or Cd^{+} center in ZSM-5. [20]

In this way, the focus is to apply EPR techniques to provide detailed information on the interaction of isolated V^{4+} species prepared by evaporation of VCl_4 onto H-ZSM-5 with ^{17}O isotopic labeling.

4.2.1 Grafting of VCl_4

The ZSM-5 powder, after the pre-treatment in vacuum at 400 °C and with O_2 at 500 °C, is exposed to VCl_4 vapours with the same method described for TiO_2 previously. In Figure 18 are reported the X-band CW spectra of the stepwise procedure with VCl_4. In this case, it is possible to observe the progressive growth of a VO^{2+} species and the formation of a small fraction of V_2O_5 aggregates.

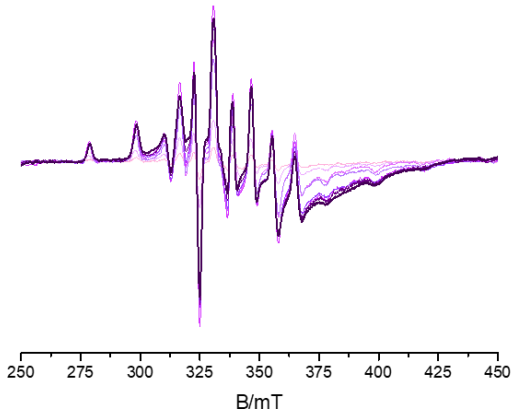

Figure 18: CW X-band EPR spectra of VCl_4 deposited on ZSM-5 at increasing doses at 77 K, 1 mW power and 0.2 mT modulation amplitude.

Moreover, the final VCl_4 sample was measured at different frequencies: X (9.5 GHz), Q (34 GHz) and W-band (94 GHz). This allows a detailed description of the spin Hamiltonian parameters obtained with the simulation. The X-band EPR spectrum could be satisfactorily simulated assuming a collinear axial model (*i.e.* x = y ≠ z, where x, y, z refers to the principal directions of the *g*- and *A*-tensors). A small discrepancy in the

positions of the hyperfine transitions and line shapes was observed between the X-band and the higher frequencies (Q- and W-band). Therefore, the possibility of a non-collinearity between the *A*- and *g*-tensor axes, was investigated and is introduced a tilting between the *g* and *A*(^{51}V) tensor principal axes of 6±2°.

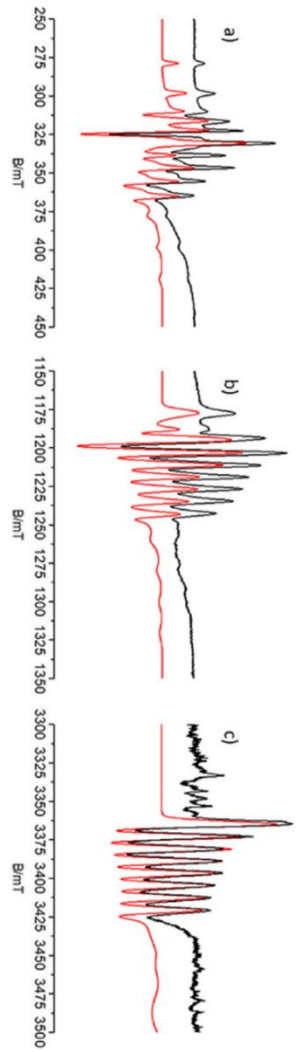

Figure 19: CW X-(a), Q-(b) and W-band (c) spectra with simulations of VCl_4-ZSM-5 adapted from reference. [13]

In Figure 19 shows the experimental versus simulation of X- Q- and W-band CW spectra (measured at 77 K, 30 K and 20 K respectively), where is possible to see the good agreement between them. It is interesting to notice that the *z*-component suffers more from the broadening effects of increasing the frequency, from ~9 GHz at X-band to ~94 GHz at W-band.

The spin Hamiltonian parameters obtained by the simulations confirm the presence of a single vanadyl species characterize by axial symmetry with g_{iso} = 1.9665 and A_{iso} = |323|, which confirm that the species is effectively in VO^{2+} form, instead of V^{4+}, as reported in literature. [21]

Table 6: Spin-Hamiltonian parameters derived from the simulation of the VCl_4-ZSM-5 sample.

Species	g_x	g_y	g_z	A_x	A_y	A_z
VO^{2+}	1.9843 ±0.0002	1.9843 ±0.0002	1.931 ±0.001	|214±3|	|214±3|	|542±3|
Aggregate	1.965±0.0008			-		

The same Hamiltonian parameters are used to also simulate the Q-band echo detected reported in Figure 20a, where the letters indicate the magnetic field settings at which ^{17}O HYSCORE experiments were carried out. In b and c panels in figure Figure 20 are related to the hyperfine interaction with ^{27}Al, while panel d is related to ^{1}H. However, both nuclei show a low signal intensity, so is not possible to do an orientation-selective analysis to have a full study for the hyperfine tensor. For the same reason, the HYSCORE spectra were symmetrized to have a precise evaluation of the full ridge extent.

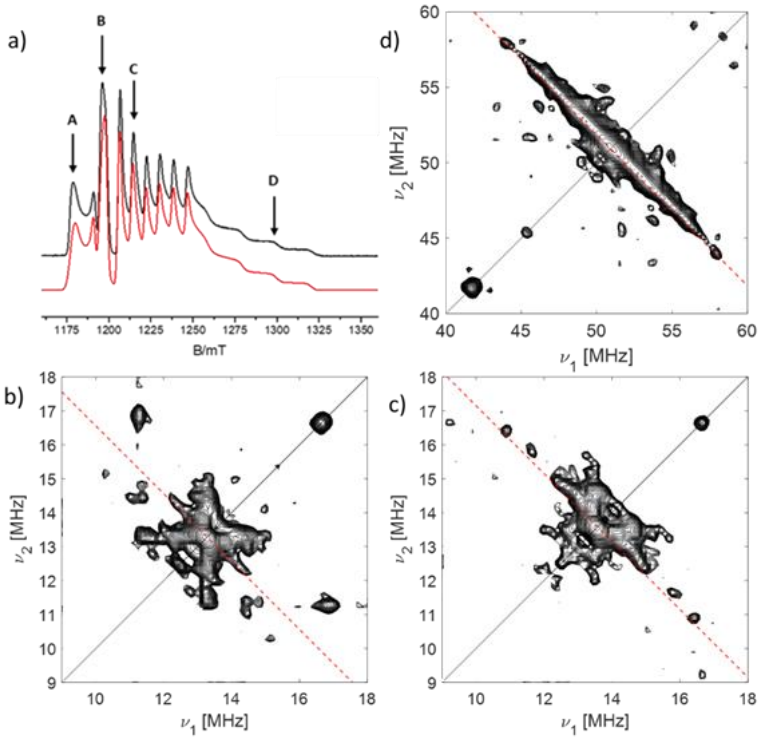

Figure 20: a) Experimental (black) and simulated (red) Q-band Echo detected EPR spectrum recorded at 10 K of the VCl4-ZSM-5 sample; b) Experimental ^{27}Al Q-Band HYSCORE spectrum recorded at position B (B_0=1196 mT) and τ = 110 ns; c) ^{27}Al Q-Band HYSCORE spectrum recorded at position C (B_0=1222 mT) and τ=110 ns; d) ^{1}H Q-Band HYSCORE spectrum recorded at position B (B_0=1196 mT). The spectrum is the sum of two spectra recorded at τ=110 ns and τ=140 ns. [13]

From the extension of the ^{27}Al ridge in both the HYSCORE spectra is possible to estimate a maximum hyperfine coupling of 2.5 MHz, while from the shape of the ridges and the vertical displacement is possible to hypothesize a significant dipolar contribution close to $^{Al}T\approx0.95$ MHz with collinearity of the g_z and $^{Al}T_z$ axes. This value is in good agreement with others reported in literature for vanadyl species located in aluminum phosphate materials and should be compatible with the interaction of the unpaired electron on the V

ion with an aluminum framework atom in the second coordination shell.[22,23]

The electron-nuclear distances, *r*, larger than 0.25 nm and in case of negligible spin delocalization over the ligand the dipolar approximation holds:

$$T = \frac{\mu_0}{4\pi} g_e g_n \beta_e \beta_n \frac{1}{r^3} \quad (4.1)$$

with *r* being the distance between the unpaired electron localized in the V d orbitals and the nucleus n.

Assuming a negligible a_{iso} value, the distance $r_{V-Al} = 0.28 \pm 0.03\, nm$ between the VO^{2+} ion and a framework Al ion is derived, using the point dipole approximation. This value is in fair agreement with the V-Al distance reported for similar V/ZSM-5 systems. [24]

Moving to the ^1H hyperfine coupling (Figure 20d) is possible to observe a pronounced ridge with a maximum width around 13 MHz. This value is in good agreement with other studies about vanadyl species on the surface of silicate [25] or aluminophosphate system, [26]characterize by a_{iso} = 3.5±0.5 MHz and T=4.5±0.5 MHz. Moreover, this coupling also shows a good agreement with quantum chemical calculations experiments for equatorially bound hydroxyls of $[VO(H_2O)_5]^{2+}$ and single-crystal ENDOR. [27]

The evaluation of the hyperfine coupling was estimated in the order of $A = [-1 - 1 + 12.5]$ MHz. Moreover, assuming a purely dipolar interaction, the V-H distance estimates with equation (4.1) is $r_{V-H} = 0.26 \pm 0.01\, nm$. Another interesting point is the there is no evidence of coordinating Cl

nuclei, and this suggests complete hydrolysis of VCl_4 molecules after reaction with surface OH groups and H_2O molecules.

The ^{17}O HYSCORE spectra are reported in Figure 21 and Figure 22. Specifically, the results obtained for ^{17}O coupling start with the analysis of the spectrum recorded at $\mathbf{B}_0$=1996 mT (field position B in Figure 20a) and then validate by using the same approach with the other HYSCORE spectra measures at different field positions. It is possible to observe in Figure 21 that the spectrum is dominated by the presence of two off-diagonal cross-peaks at about (9.5, 4.5) MHz and (4.5, 9.5) MHz, centred at the ^{17}O Larmor frequency (ν_O = 6.9 MHz) and relating the m_I ½ → −½ transitions of the two m_S manifolds (single quantum transitions, SQ-SQ). Additionally, it is possible to appreciate the cross peaks at (19, 4.5) MHz and (4.5, 19) MHz, and (19, 9) MHz and (9, 19) MHz that are assigned to single-double (SQ-DQ) and double quantum (DQ-DQ) transitions. These signals are plotted in a separate insert in Figure 21 because of their low intensity with respect to the other signals, which corresponds to lower transition probability.

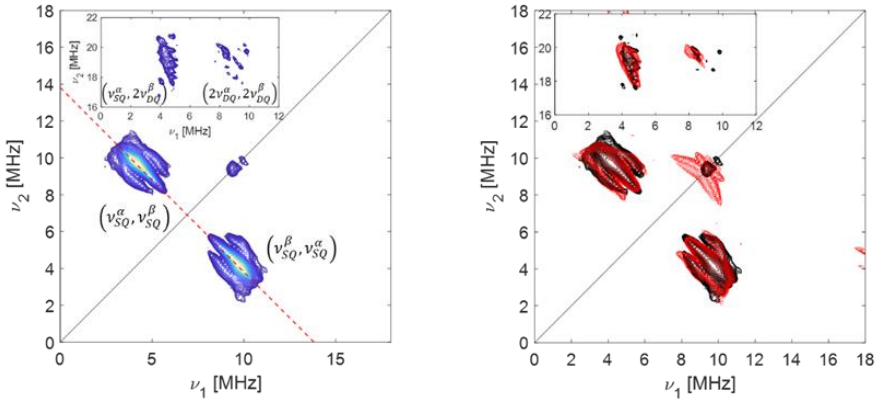

Figure 21: Experimental and simulated (red) 17O HYSCORE spectra of a ^{17}O enriched VCl4-ZSM-5 sample. The spectra are recorded at a magnetic field setting B_0=1196 mT (position B in figure 2a) with τ= 144 ns at 10 K. [13]

Moreover, it is possible to observe in Figure 21 a moderately elongated SQ cross-peaks composed of a central intense peak, flanked by two extra cross-peaks with lower intensity, and these features can be explained as part of a splitting quintet due to the nuclear quadrupole interaction. The difference in the intensity between the central cross-peaks with respect to the satellite lines can be explained by the presence of two different nuclei, where one shows a smaller nuclear quadrupole value to that contributing to the central line (indicate with O1), while the other is characterize by a larger coupling that generates the splitting structure (O2). This hypothesis is confirmed by a simulation analysis, plotted in red in Figure 21 obtained by summing the contributions of two O nuclei (O1 and O2 in Table *7*), where was not possible to reproduce the experimental spectrum with a single set of nuclei because in this way is not possible to take into account both the splitting and the relative intensity of the different cross-peaks.

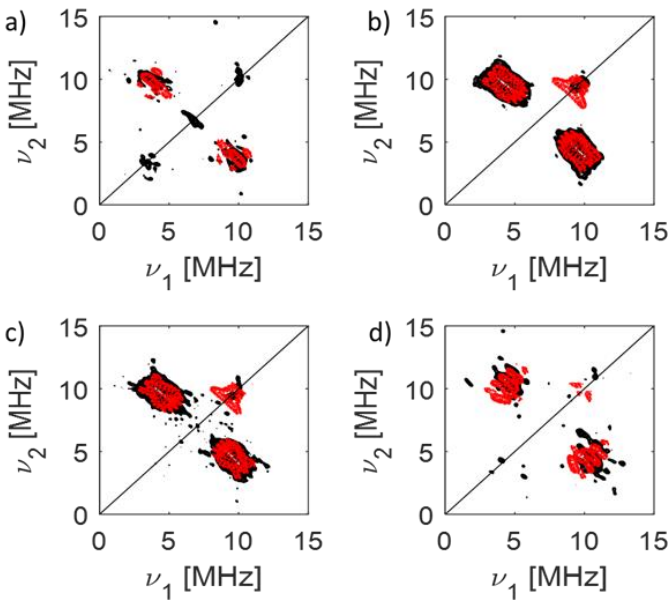

Figure 22: Experimental (black) and simulated (red) ^{17}O HYSCORE spectra of the VCl_4-ZSM-5 sample. a) observer position: B_0=1180.7 mT τ =216 ns; b) observer position: B_0=1196.0 mT, τ = 144 ns; c) observer position B_0=1213.1 mT τ = 144 ns and (d) observer position: B_0=1300.0 mT, τ = 144 ns. All spectra were recorded at T= 30 K. Figure from reference. [13]

From the simulation of the HYSCORE spectra recorded at different magnetic field settings, the central intense pair of cross-peaks belonging to O2 could be simulated with the parameters reported in Table *7*. From these values, a Fermi contact (a_{iso}) term of about 4 MHz and an anisotropic coupling tensor $T = [-1.7 \pm 0.5 - 1.7 \pm 0.5 + 3.4 \pm 0.5]$ MHz are extracted. The dipolar hyperfine tensor translates into a V-O1 distance of the order of 0.19 nm.

The ^{17}O hyperfine interaction obtained for this system is very small, concerning what was observed for Zn^+ ions featuring a $4s^1$ ground state, [20] which points to a non-bonding character of the d_{xy} orbital hosting the unpaired electron, like what is observed for pentaquo vanadyl molecular complexes. [14]

The orientation of the *T* tensor relative to the *g*-tensor principal frame, given by the Euler angle β, shows that the V-O2 are tilted by ≈50° with respect to the g_z axis. This, in case of vanadyl ion, is assumed to be collinear with the direction of the shortest V=O bond. Hence, the hyperfine parameters point to a geometry where the O=V-O2 angle is of the order of 130°. Spectral simulations allow estimating the upper limit of the nuclear quadrupole interaction for O2 as e^2qQ/h = 2 ± 0.5 MHz. The splitting lines observed in the experimental spectrum are due to the nuclear quadrupole interaction of O1 and can be reproduced with e^2qQ/h values of the order of 9±1 MHz, keeping the hyperfine parameters (a_{iso} and *T*) unchanged. This value is in line with the value of 10.7 MHz reported by Baute and Goldfarb [14] for equatorially bound ^{17}O labeled water molecules in the vanadyl aquo complex.

Table 7: Spin Hamiltonian parameters derived from the simulation of the HYSCORE experiments of VCl_4-ZSM-5 sample.

Nuclei	A_x	A_y	A_z	**Euler angle** α,β,γ	e^2qQ/h	η	**Euler angle** α',β',γ'
$^{17}O(1)$	2.6 ±0.5	2.6 ±0.5	7.2 ±0.5	0, 60±10, 0	9.5±0.5	0.2±0.2	0, 70±10, 0
$^{17}O(2)$	2.6 ±0.5	2.6 ±0.5	7.2 ±0.5	0, 50±10, 0	2.0±0.5	0.0	-
^{27}Al	-0.35 ±0.5	-0.35 ±0.5	2.5 ±0.5	0, 0±30, 0	-	-	-
^{1}H	-1.0 ±0.5	-1.0 ±0.5	12.5 ±0.5	0, 60±30, 0	-	-	-

To summarize, the analysis of multifrequency EPR experiments of vanadyl species, introduced in H-ZSM-5 through reaction of the zeolite with VCl_4

vapours, provides evidence for the formation of isolated vanadyl species. HYSCORE experiments indicate the interaction of such vanadyl species with at least one Al ion in the second coordination sphere at a distance of the order of 0.28 nm and a directly linked hydroxyl species with an H-V distance of the order of 0.26 nm. Moreover, ^{17}O HYSCORE experiments indicate the presence of at least two different binding oxygens characterized by different nuclear quadrupole couplings and assigned to the hydroxyl oxygen (large coupling) and a framework oxygen ion (low quadrupole). These results indicate that the grafting protocols place V-oxo species onto the exchange site featuring Al species, with an all-oxygen first coordination sphere. The lack of Cl couplings is understood as the result of consecutive hydrolysis steps involving surface hydroxyls and residual water molecules. A similar reaction path was reported by Lacheen and Iglesia [24] for the reaction of gas-phase $ZrCl_4$ with H-ZSM-5 and subsequent hydrolysis. The reaction of $ZrCl_4$ with acidic OH groups was proven to lead to HCl and $ZrCl_3^+$-ZSM-5 species, which evolved during hydrolysis, into $ZrO(OH)^+$ species. This reaction pathway nicely agrees with our observation of vanadyl species coordinated to a hydroxyl ion and the absence of coordinating Cl ions. Charge neutralities require that such species, featuring a single positive charge, are localized at Al sites as shown in Scheme 2a, whereby they compensate for the proton charge. In this scheme, the Al ion is located along the direction of the V=O bond, coinciding with the g_z component of the *g*-tensor and below the xy plane, where the spin density is located (d_{xy} orbital). This geometrical arrangement is consistent with reports relative to ZrO^{2+} monomers at ZSM-5 Al sites [24] and Zn^+ species at T7 sites of the same zeolite. [20] The O=V-O angle can be derived from the orientation of O(2) with respect to the g_z

component leading to a bond angle of 130°±10° consistent with VO^{2+} units coordinated at the surface of heteropolyacids, [28] We remark that this coordination geometry does not exclude the possible binding at other sites such as T8, placed on the wall of the straight channel, [20] with a relatively flat local environment and potentially favouring coordination to a larger number of oxygens.

The possibility that OH-free V=O species, resulting from the condensation of two monomers, are present cannot be excluded but such species will require sites featuring two neighbouring Al ions to compensate for the +2 charge as shown in Scheme 2b. Clearly, the abundance of such species will depend on the Al/Si ratio.

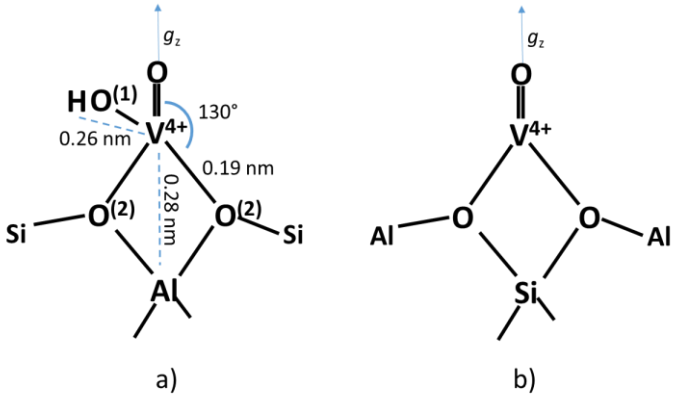

Scheme 2: Schematic representation of two possible VO structures. The oxygen numbering in Scheme 1a refers to the nuclei in Table 7.

Moreover, monomeric $VO(OH)^{+}$ could de-anchor in the presence of trace moisture to exchange and migrate possibly to external surfaces and form aggregates, which may explain the broad background observed in the CW EPR spectra.

References Chapter 4

[1] Diebold, U., Surf. Sci. Rep., 2000, 48, 53-229.

[2] Busca, G., *Mater. Chem. Phys*. 1988, *19*, 157–165.

[3] Hausinger, G., Schmelz, H., Knozinger, H., *Appl. Catal.,* 1988, *39*, 267–283.

[4] Handy, B. E., Gorzkowska, I., Nickl, J.; Baiker, A., Schramlmarth, M., Wokaun, A., *Ber. Bunsen-Ges.* 1992, *96*, 1832–1840.

[5] Wei-Zhen Li et al., *J. Phys. Chem. C* 2015, *119*, 15094–15102.

[6] J Arnarson, L., Rasmussen, S. B., Falsig, H., Lauritsen, J. V. & Moses, P. G., *J. Phys. Chem. C* 2015, *119*, 23445‑23452.

[7] Song, L., Zhang, R., Zang, S., He, H., Su, Y., Qiu, W., Sun, X., *Catal. Lett*. 2017, *147*, 934–945.

[8] Lai, J.-K.; Wachs, I. E., ACS Catal. 2018, 8, 6537–6551.

[9] V. Lagostina, M. C. Paganini, M. Chiesa, E. Giamello, *J. Phys. Chem. C,* 2019, 123, 7861−7869.

[10] P. Jakes, R.-A. Eichel, *Mol. Phys.*, 2012, 110, 277-282.

[11] Morton, J. R., Preston, K. F., *J. Magn. Reson*. 30, 577, 1978.

[12] M. R. Maurya, *Coo. Chem. Rev., 2019, 383, 43-81*.

[13] V. Lagostina, E. Salvadori, M. Chiesa, E. Giamello, *J. Catal*., 2020, 391, 397-403.

[14] D. Baute, D. Goldfarb, *J. Phys. Chem. A*, 2005, 109, 7865-7871.

[15] N. Cox, W. Lubitz, A. Savitsky, *Mol. Phys.*, 2013, 111, 2788-2808.

[16] Livraghi, S.; Chiesa, M.; Paganini, M. C.; Giamello, E., *J. Phys. Chem. C*, 2011, 115, 25413–25421.

[17] Larsen, S. C.; Singel, D. J., *J. Phys. Chem.*, 1992, 96, 9007–9013.

[18] Woodworth, J.; Bowman, M. K.; Larsen, S. C., *J. Phys. Chem. B*, 2004, 108, 16128 –16134.

[19] Morra, E.; Maurelli, S.; Chiesa, M.; Giamello, E., *Top. Catal.*, 2015, 58, 783–795.

[20] E. Morra, M. Signorile, E. Salvadori, S. Bordiga, E. Giamello, M. Chiesa, *Angew. Chem*., 2019, 131, 12528–12533.

[21] P. Jakes, R.-A. Eichel, *Mol. Phys.*, 2012, 110, 277-282.

[22] V. Nagarajan, D. Rings, L. Moschkowitz, M. Hartmann, A. Pöppl, Chem. Lett., 2005, 34, 1614-1615.

[23] S. Maurelli, G. Berlier, M. Chiesa, F. Musso, F. Corà, J. Phys. Chem. C, 2014, 118, 19879−19888.

[24] H. S. Lacheen, E. Iglesia, J. Phys. Chem. B, 2006, 110, 5462-5472.

[25] M. Chiesa, V. Meynen, S. Van Doorslaer, P. Cool, E. F. Vansant, *J. Am. Chem. Soc.*, 2006, 128, 8955-8963.

[26] S. Maurelli, G. Berlier, M. Chiesa, F. Musso, F. Corà, *J. Phys. Chem. C*, 2014, 118, 19879−19888..

[27] N. M. Atherton, J. F. Shackleton, *Mol. Phys.*, 1980, 39, 1471-1485.

[28] A. Poeppl, P. Manikandan, K. Koehler, P. Maas, P. Strauch, R. Boettcher, D. Goldfarb, *J. Am. Chem. Soc.*, 2001, 123, 4577-4584.

Chapter 5

Magnetic Properties and Relaxation in Vanadium (IV) Molecular Complexes

5.1 Introduction

Magnetic molecules are next-generation components of many different technological areas, ranging from magnetic resonance imaging (MRI) [1] to quantum information technologies. [2] In any of these applications the ability to modulate the spin-lattice relaxation times and phase-memory relaxation times is needed. T_1 defines the lifetime of an excited spin and is the upper limit of T_m. In contrast, T_m is the lifetime of the electron spin superposition or coherence time. Designing systems where both of these parameters are long is a challenge due to the ubiquitous spin bath (nearby electronic spins or nuclear spins), which produces stochastic interactions that shorten T_1 and T_m.

Among others, vanadium (IV) complexes are actively studied as potential candidates for molecular spin qubits operating at room temperatures, [3,4,5] but also proposed as potential contrast agents, [6] whereby the paramagnetic complexes near solvent protons create a local fluctuating magnetic field that

increases the efficiency of proton relaxation. Vanadium (IV) has an electron spin $S = 1/2$ and a nuclear spin $I = 7/2$ for the stable isotope ^{51}V with nearly 100% natural abundance. Vanadyl complexes, in particular, have longer electron spin decoherence times than many other first-row transition metal ions, being this the key property for applications in quantum information processing. The relaxivity (defined in chapter 2.4) induced by VO^{2+} compounds are lower than those of low molecular weight gadolinium complexes, but still provide significant enhancement in magnetic resonance images. [7] Mustafi et al. [7] reported the use of $VO(acac)_2$ as a potential contrast agent and studied the interaction of the complex with serum albumin and in vivo experiments for imaging in rats tumours. It is important to say that vanadyl complexes are used in other medical applications [8] for the treatment of diabetes, anti-tumour therapy and anti-parasitic issues. Another application is in catalysis, [9] as a catalyst for various oxidation reactions in liquid or in supported systems.

The NMR of paramagnetic species is a quite complicated field because the presence of unpaired electrons cause-effect principally on the transverse correlation time (T_2) that is directly associated with the linewidth of the NMR signals. So, in the case of long T_2, is possible to observe the NMR spectra, but when the T_2 is much shorter the signal became too broad to be detected. To overcome this limitation was developed the Fast Field Cycling NMR [10]permits to study of the structural and dynamical properties of the complexes dissolved in a solvent (usually in H_2O) by investigating the solvent magnetic properties. This technique is largely used for the development of new contrast agents for MRI applications.

The contrast agents that are approved for human clinical diagnosis are mainly based on Gadolinium (III) complexes, coordinated by an organic ligand with eight coordination sites and one water molecule. [11,12,13] This set-up is important because the water molecule directly coordinated to the Gd(III) ion is in exchange with the bulk water, which generate the relaxation effects, and, on the other side, gives a high kinetically stability to the complex, in order to prevent the releasing of free metal ion in human blood. From this first type of contrast agent based on Gd(III), other metal ions are tested as potential CAs, and also new contrast way is tested, as para-CEST [14] (Chemical Exchange Saturation Transfer) effect due to shift-reagents paramagnetic complexes.

Experimentally, the effects of the paramagnetic complex on water protons relaxations are investigated with relaxometry measures that are influenced by many parameters. The theoretical description of the relaxation theory is given by the Solomon-Bloembergen-Morgan equations (see chapter 2.4), [15]which contain many aspects that describe the relaxation mechanism, scalar (contact) and dipolar-dipolar effects. Moreover, for Gd^{3+} that has $S = {}^{7}/_{2}$, the zero field contribution on electronic relaxation must be taken into account.. It is also important to take into account the dynamic aspect, in terms of motion of the complex in solution depending on the rotational effect and viscosity for example.

It is clear that many parameters influence the description of relaxation effects of paramagnetic complexes in water solution and, to partially simplify the system, in 1998 Chen et al. [6] proposed the use of vanadyl complexes combining Nuclear Magnetic Relaxation Dispersion (NMRD) and EPR techniques to have a better understanding of the rotational dynamics.

It is indeed clear that the technological improvement in these 23 years is a relevant aspect. The very first FF-NMR spectrometer was assembled in research laboratories, but now there are commercial instruments that measure until quite high field (3 T) coupled with a precise temperature control unity that permits to perform variable. [16]

In this chapter combined EPR and relaxometry studies are reported on a series of vanadyl complexes with the aim of clarifying the relationship between the different molecular parameters (electron spin relaxation times, rotational effects, hydration state, water exchange rate…) that describe the structural and dynamic properties of the complexes. In particular, the inner-sphere and second/outer-sphere contributions to the overall relaxation properties are investigated by changing the type of ligand with particular attention to the role of the specific water coordination site, axial vs equatorial, by using selected ligands as oxalic acid (oxa), nitrilotriacetic acid (nta) and acetilcacetonate (acac), which form complexes with just one water molecule in direct coordination to the vanadyl ion but with a different spatial position (figure 1). These results are compared with the VO-water complex [17] and VO-dtpa [6] results already reported in literature. In particular, the spin dynamics extracted by EPR (rotational correlation time (τ_R), [18] spin lattice relaxation (T_1) [19] and spin echo dephasing (T_m or T_2) [20]) will be compared to NMR relaxometry data to clarify structure-property.

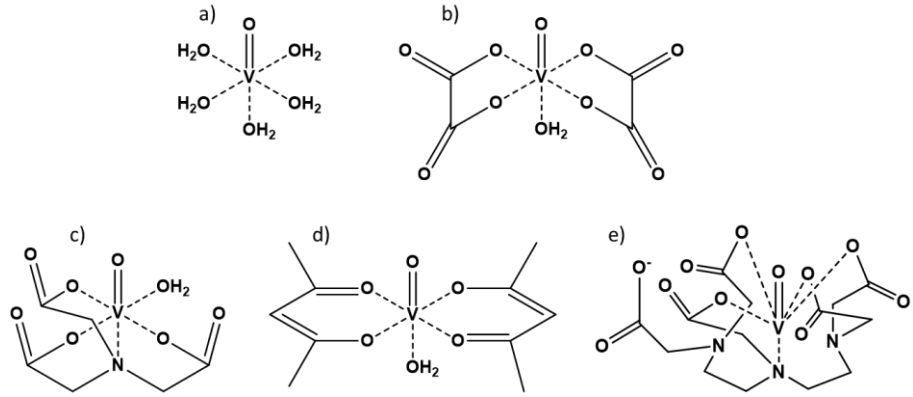

Figure 1: structures representation of VO complexes: a) $VO(H_2O)_5$, b) $VO(oxa)_2$, c) VO-nta, d) $VO(acac)_2$ and e) VO-dtpa.

5.2 EPR studies

5.2.1 CW experiments

The EPR spectra of VO-complexes in water frozen solution show the characteristic EPR spectrum with the expected eight-fold hyperfine splitting typical of V^{IV} (^{51}V *I* = 7/2, natural abundance 99.76%) and rhombic *g*- and *A*-tensors. Computer simulation of the spectra based on the first two terms (electronic Zeeman and hyperfine coupling) of the spin Hamiltonian of eq 3.1 (where g is the electronic anisotropic Landé tensor, *A* the hyperfine coupling tensor, *P* the quadrupolar interaction and g_N the nuclear spectroscopic factor) provide the parameters reported in Table 1.

$$\boldsymbol{\mathcal{H}} = \mu_B \, \hat{\boldsymbol{S}} \cdot \boldsymbol{g} \cdot \vec{\boldsymbol{B}} + \hat{\boldsymbol{I}} \cdot \boldsymbol{A} \cdot \hat{\boldsymbol{S}} + \hat{\boldsymbol{I}} \cdot \boldsymbol{P} \cdot \hat{\boldsymbol{I}} + -\mu_N \, \hat{\boldsymbol{I}} \cdot g_N \cdot \vec{\boldsymbol{B}} \qquad (3.1)$$

Table 1: Spin-Hamiltonian parameter of VO-complexes obtained from CW EPR spectra simulations.

Complexes	g_x	g_y	g_z	A_x	A_y	A_z
$VO(H_2O)_5$	1.9786	1.9786	1.9344	-206.5	-206.5	-546
VO-dtpa	1.9822	1.9770	1.9444	-184	-176	-507
$VO(oxa)_2$	1.9801	1.9760	1.9392	-192	-181	-520
VO-nta	1.9820	1.9770	1.9375	-203	-187	-527
$VO(acac)_2$	1.9805	1.9735	1.9444	-161	-176	-498

The experimental and simulated spectra of the different complexes recorded at 77 K are reported in Figure 2. The symmetry of the $[VO(H_2O)_5]^{2+}$ tensors is completely axial while, for the other complexes, a slightly rhombic is found. The $VO(acac)_2$ complex is characterized by quite a different spectrum that reflects the differences in spin-Hamiltonian parameters.

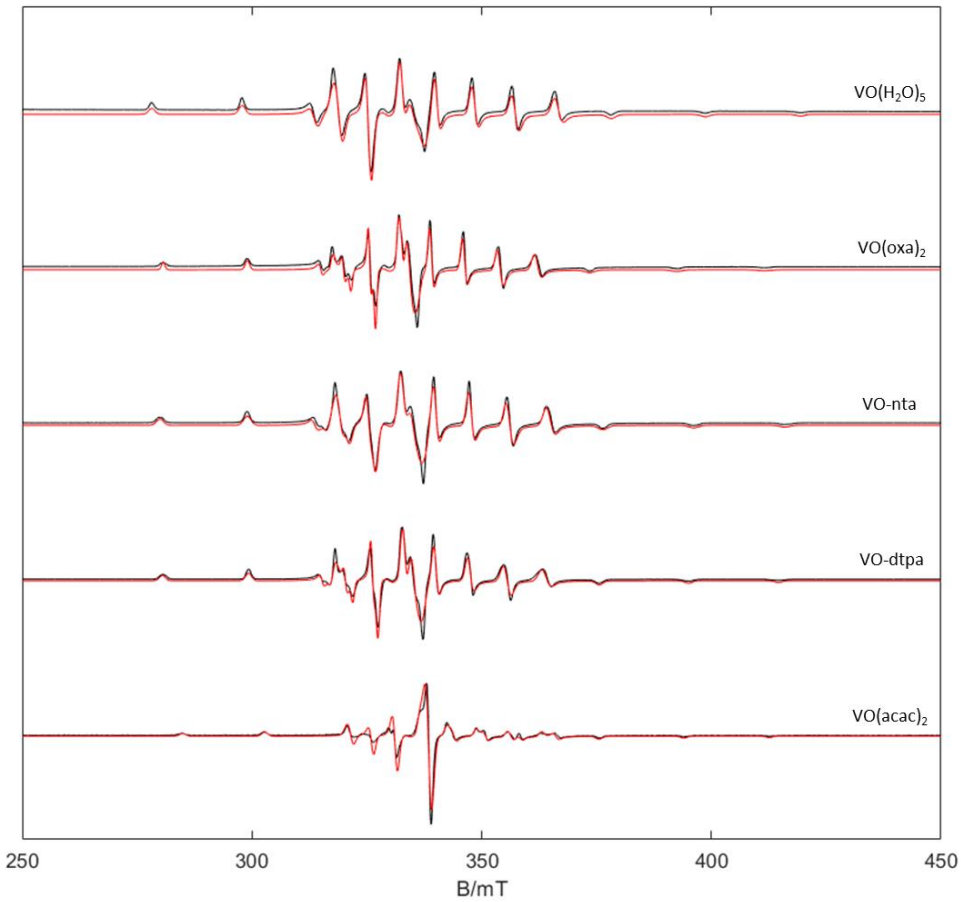

Figure 2: X-band CW EPR spectra of frozen solutions of complexes (experimental black line, simulation red one) at 77 K, 1 mW power and 0.2 mT modulation amplitude.

5.2.2 Variable temperature experiments

EPR spectra for all complexes, except $VO(acac)_2$, were measured in the temperature interval between 294 K and 353 K in water solution. Under these circumstances, the anisotropic *g*- and *A*-tensors are averaged out depending on the rate of motion of the complex, which in turn depends on

the temperature. The result is an 8 lines spectrum centered at the average g factor. Inspection of Figure 3 shows a clear m_I linewidth dependency, which is directly correlated to the rotational correlation time. [21] By using the rigid limit spin-Hamiltonian parameters reported in Table 1, τ_R was determined through the simulation of the spectra using the Easyspin routine garlic. In this way, the spectra are simulated leaving as a unique free parameter τ_R.

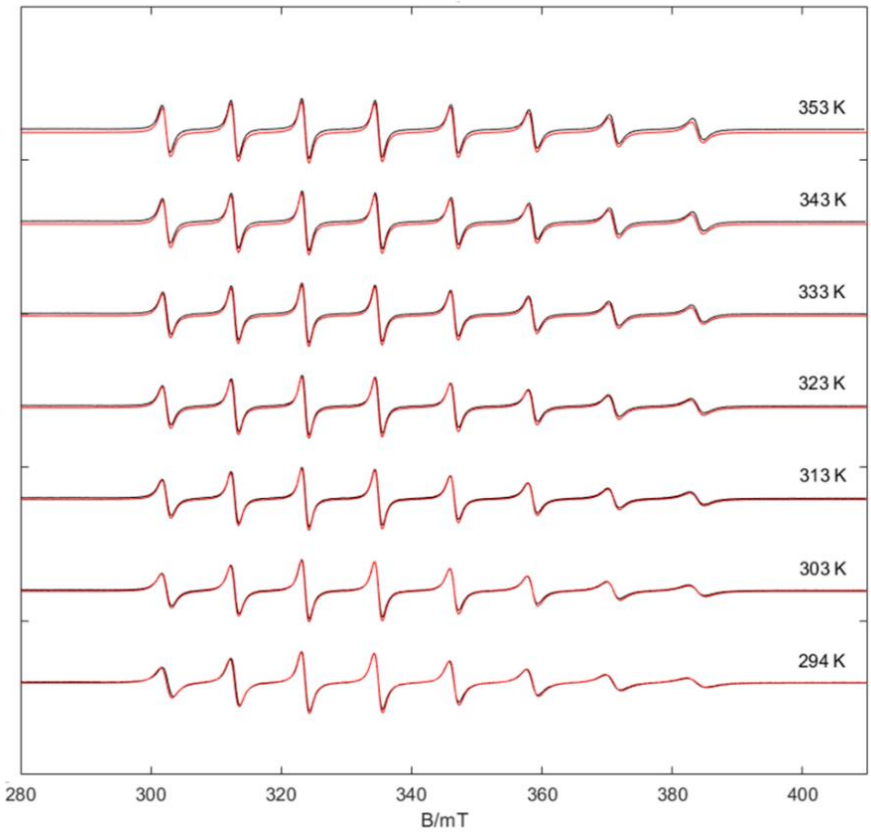

Figure 3: X-band CW EPR spectra of $VO(H_2O)_5$ at variable temperature experimental (black) and simulation (red) 10 mW power and 0.5 mT modulation amplitude.

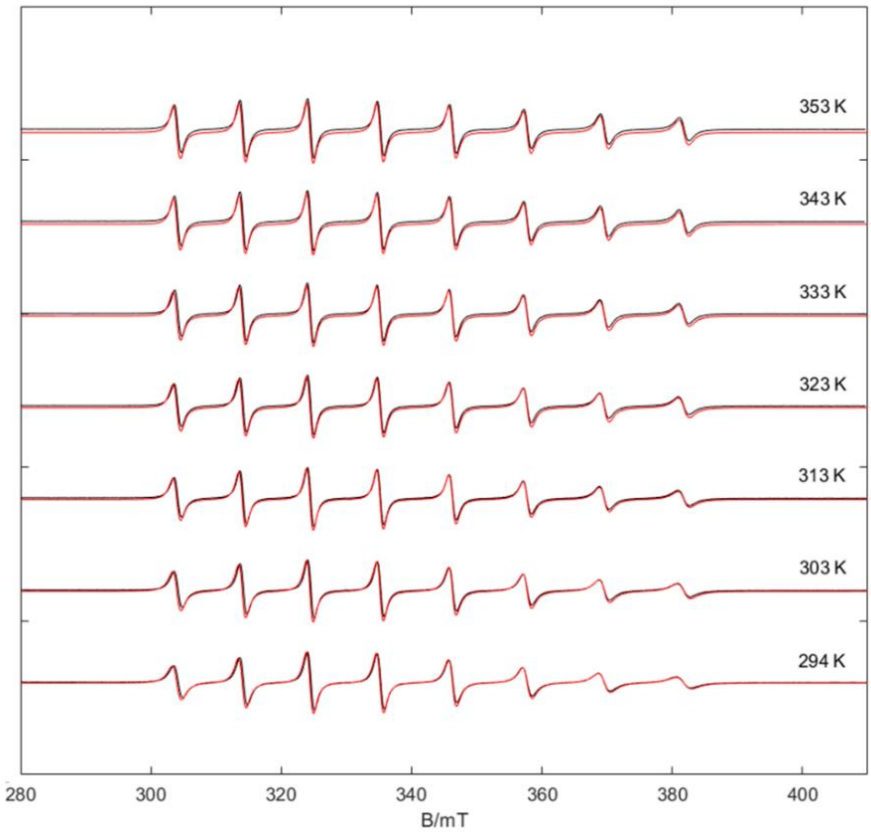

Figure 4: X-band CW EPR spectra of VO-nta at variable temperature experimental (black) and simulation (red) 10 mW power and 0.5 mT modulation amplitude.

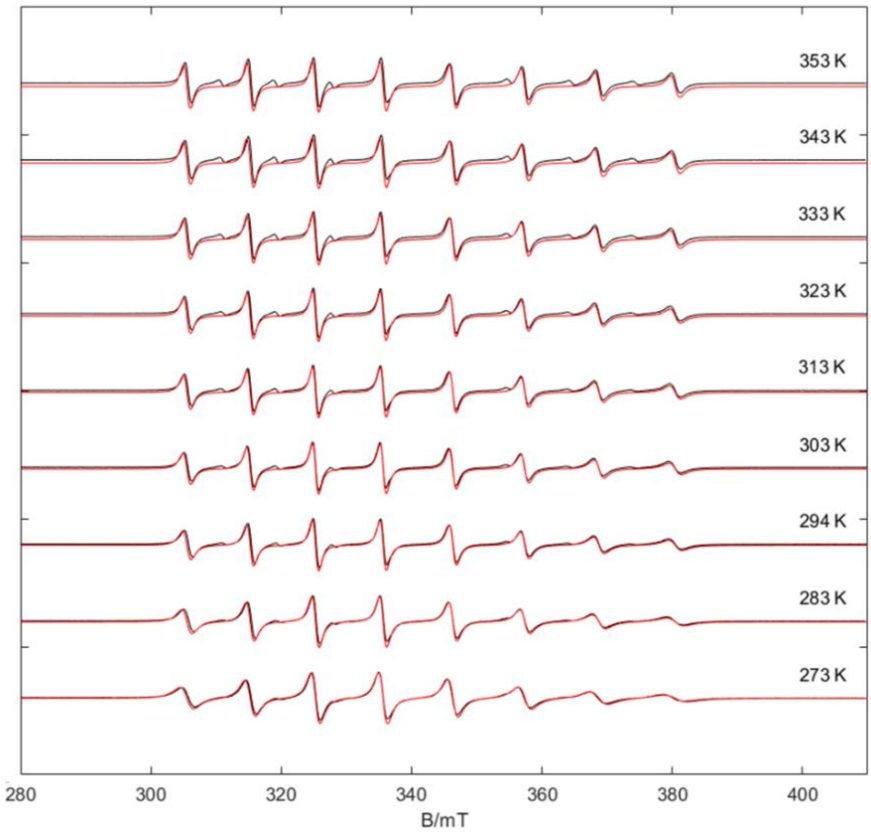

Figure 5: X-band CW EPR spectra of $VO(oxa)_2$ at variable temperature experimental (black) and simulation (red) 10 mW power and 0.5 mT modulation amplitude.

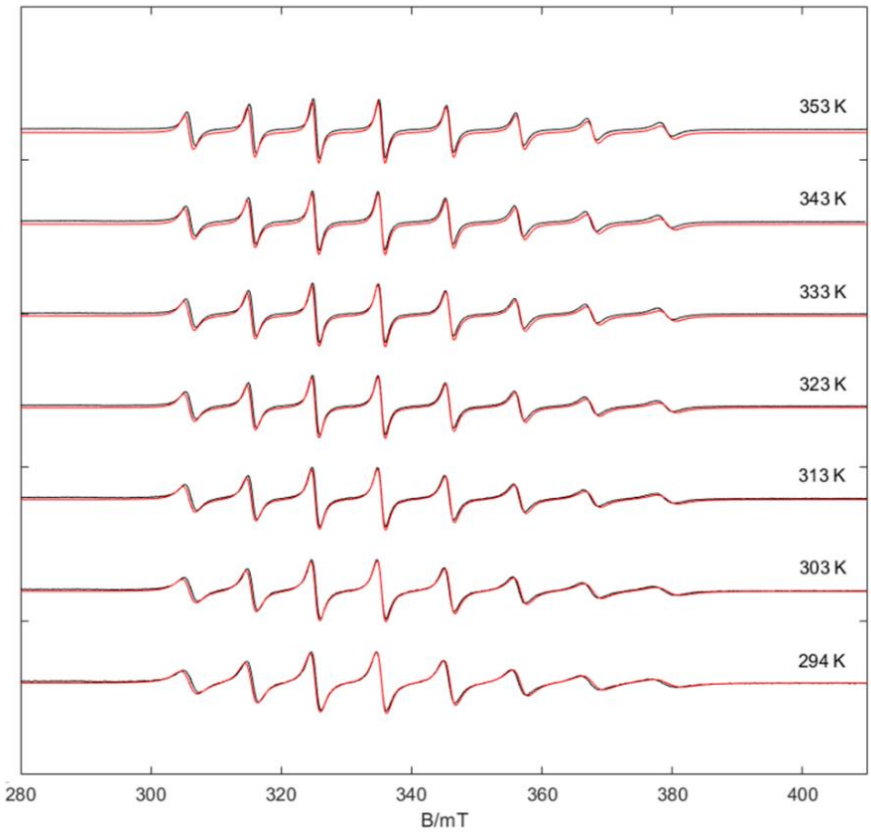

Figure 6: X-band CW EPR spectra of VO-dtpa at variable temperature experimental (black) and simulation (red) 10 mW power and 0.5 mT modulation amplitude.

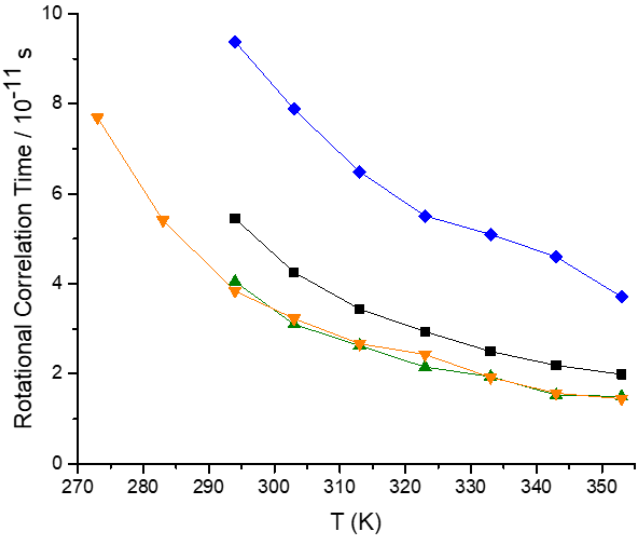

Figure 7: Rotational correlation time in function of temperature of $VO(H_2O)_5$ (black), VO-dtpa (blue), $VO(oxa)_2$ (orange) and VO-nta (green).

The obtained τ_R values are summarized in Table 2 and plotted in Figure 7: Rotational correlation time in function of temperature of $VO(H_2O)_5$ (black), VO-dtpa (blue), $VO(oxa)_2$ (orange) and VO-nta (green) as a function of temperature. A similar trend is observed for the different complexes where τ_R decreases while temperature increase, as expected. The slowest τ_R is found for the VO-dtpa complex while the faster rotational correlation time is found for VO-nta and $VO(oxa)_2$. For $VO(acac)_2$ only the room temperature spectrum is measured (~295 K) providing a $\boldsymbol{\tau_R} = 7.7 * 10^{-11}$ s.

Table 2: Rotational correlation time ($\boldsymbol{\tau}_{\mathrm{R}}$ $(10^{-11}$ s)) of VO-complexes calculated by EasySpin simulations.

T (K)	$VO(H_2O)_5$	VO-dtpa	VO-nta	$VO(oxa)_2$	$VO(acac)_2$
273	-	-	-	7,69	-
283	-	-	-	5,41	-
295	5,45	9,38	4,05	3,84	7.7
303	4.26	7,88	3,10	3,23	-
313	3,44	6,49	2,63	2,67	-
323	2,94	5,51	2,15	2,43	-
333	2,50	5,10	1,94	1,92	-
343	2,19	4,60	1,53	1,57	-
353	1,99	3,71	1,50	1,45	-

5.2.3 Electron Spin Dynamics. T_1 and T_m Measurements

To investigate the temperature dependence of the electronic relaxation times of the VO complexes, Q-band ESE EPR spectra were recorded by using a standard Hahn echo sequence. Representative spectra recorded at 10 K are shown in Figure 8, along with the corresponding computer simulations. The spin Hamiltonian parameters obtained by the analysis of the CW-X-band EPR spectra provide a good simulation of the Q-band ESE spectra allowing to place good confidence on the values of Table 1 and indicating that all the allowed electron spin transitions are detected under the experimental conditions. The electron spin relaxation times were measured at a fixed magnetic field, indicated by the asterisk in Figure 8. To investigate the spin relaxation times in detail and to quantify the electronic phase memory time and the spin-lattice relaxation times in the frozen solutions as a function of

the temperature, echo decay and inversion recovery experiments were performed in the temperature interval 20-200 K. The results are shown in Figures 9-13.

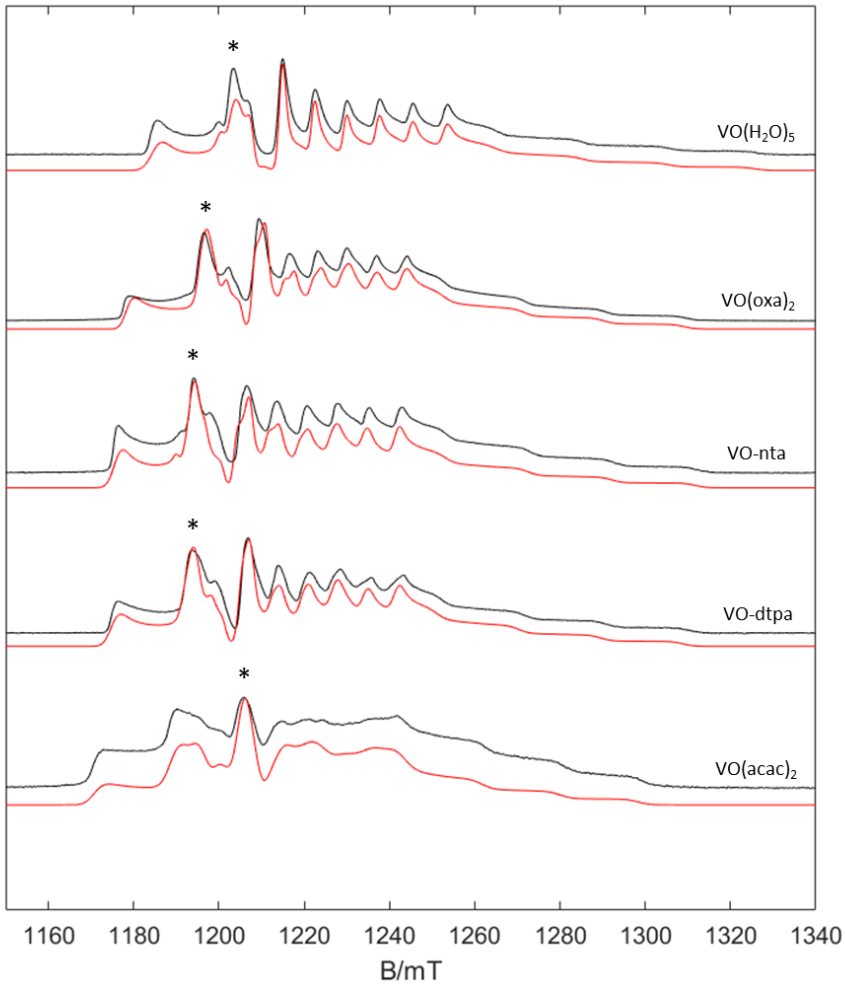

Figure 8: Q-band ESE spectra (black) with simulation (red) of VO-complexes.

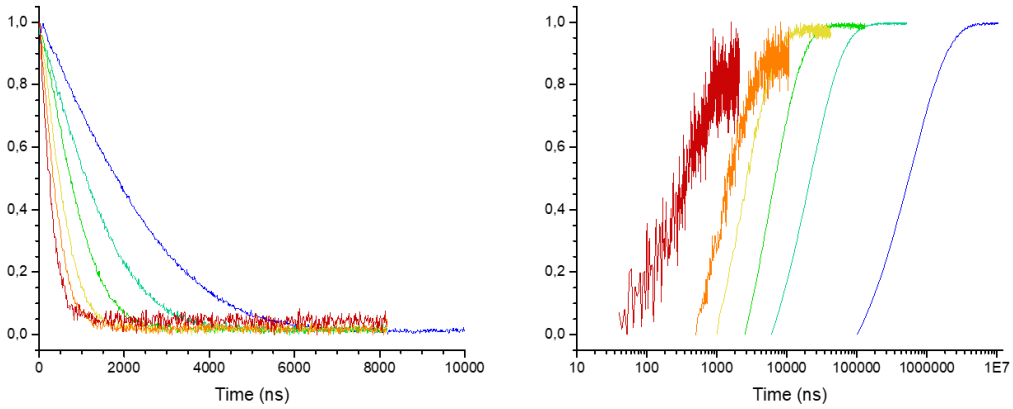

Figure 9: $VO(H_2O)_5$ T_m (left) and T_1 (right) at different temperatures: 20 K (blue), 50 K (light blue), 80 K (green), 120 K (yellow), 150 K (orange) and 200 K (red).

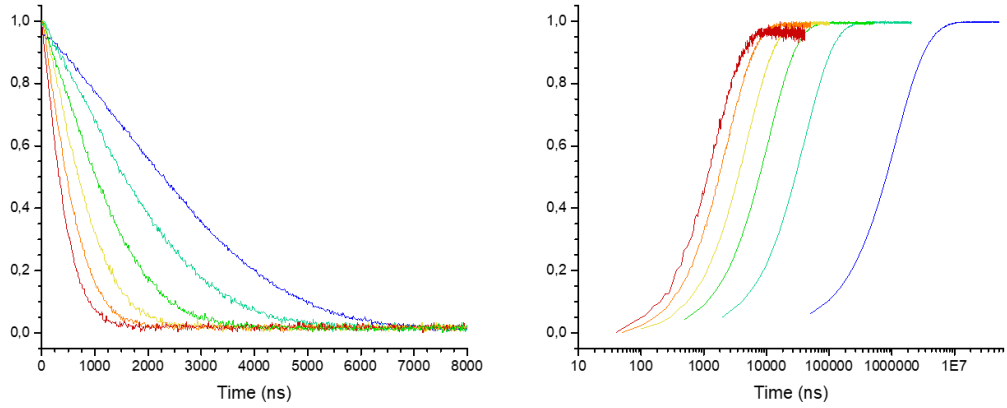

Figure 10: $VO(oxa)_2$ T_m (left) and T_1 (right) at different temperatures: 20 K (blue), 50 K (light blue), 80 K (green), 120 K (yellow), 150 K (orange) and 200 K (red).

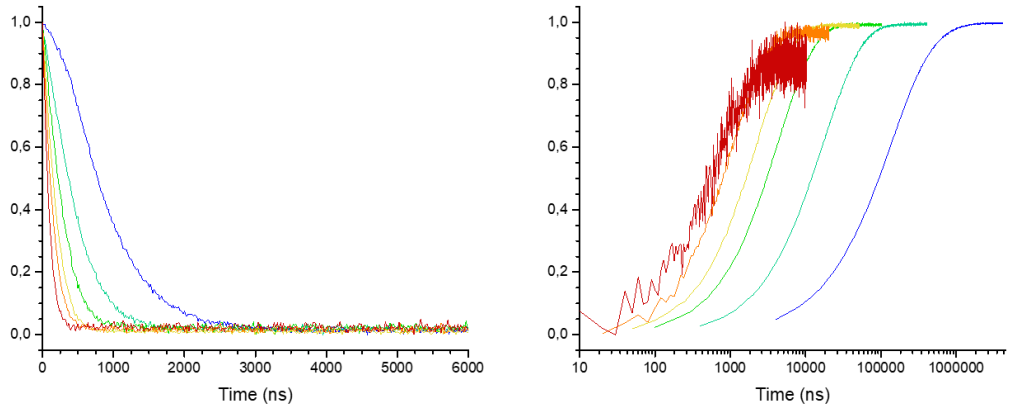

Figure 11: VO-nta T_m (left) and T_1 (right) at different temperatures: 20 K (blue), 50 K (light blue), 80 K (green), 120 K (yellow), 150 K (orange) and 200 K (red).

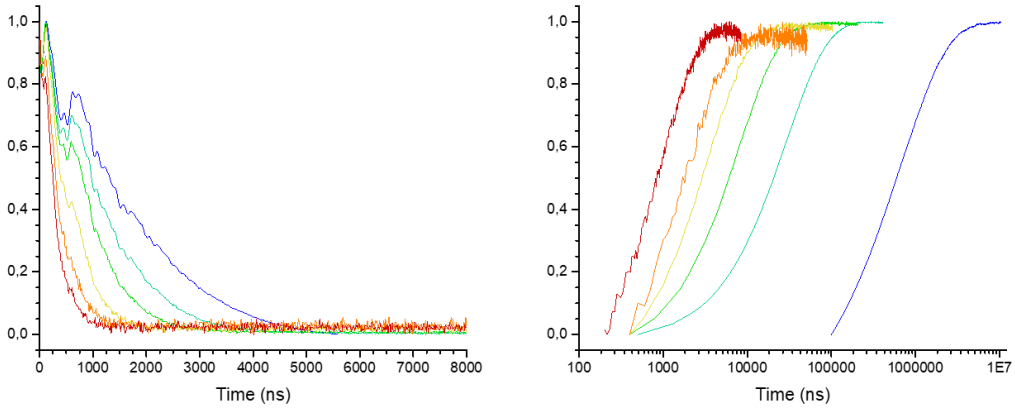

Figure 12: VO-dtpa T_m (left) and T_1 (right) at different temperatures: 20 K (blue), 50 K (light blue), 80 K (green), 120 K (yellow), 150 K (orange) and 200 K (red).

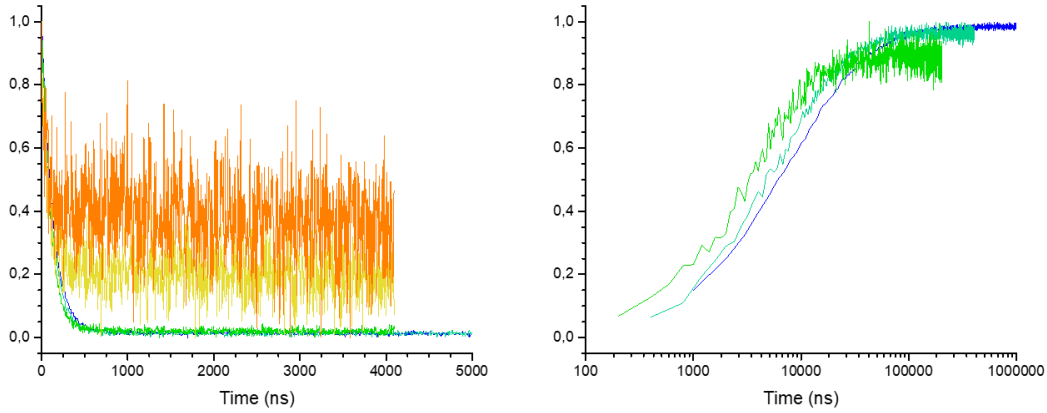

Figure 13: $VO(acac)_2$ T_m (left) and T_1 (right) at different temperatures: 20 K (blue), 50 K (light blue), 80 K (green), 120 K (yellow), 150 K (orange) and 200 K (red).

For T_m measurements the decay traces were fitted using the stretched-exponential equation 3.2:

$$I = I_0 + k_m exp^{\left[-\left(\frac{2\tau_p}{T_m}\right)^{\beta m}\right]} \quad (3.2)$$

as usually done for transition metal systems, where I indicate the echo intensity, $2\tau_p$ is the delay between the initial pulse and the echo detection and τ_m is the stretch factor. The extracted T_m values are reported in Table 3 and plotted in Figure 14.

Table 3: T_m and stretch fitting values in function of temperature for VO-complexes.

Complexes	T (K)	T_m (ns)	Stretch
$VO(H_2O)_5$	20	2408	1,37
	50	1505	1,39
	80	966	1,41
	120	616	1,37
	150	439	1,29
	200	302	1,2
VO-nta	20	569	1,09
	50	419	11,8
	80	293	1,21
	120	193	1,17
	150	142	1,12
	200	105	1,12
$VO(oxa)_2$	20	3004	1,61
	50	2027	1,46
	80	1329	1,42
	120	888	1,4
	150	610	1,31
	200	438	1,26
VO-dtpa	20	2511	1,30
	50	1393	1,40
	80	1028	1,39
	120	630	1,29
	150	424	1,35
	200	331	1,41
$VO(acac)_2$	20	130	1,01
	50	120	1,03
	80	104	1,04
	120	64	0,77
	150	-	-
	200	-	-

To investigate the temperature dependence of the electronic spin-lattice relaxation time T_1, inversion recovery experiments were carried out in the same temperature interval. The resulting inversion recovery traces were fitted with a bi-exponential equation 3.3:

$$I = I_0 + k_m exp\left[-\left(\frac{\tau}{T_1}\right)\right] + k_n exp\left[-\left(\frac{\tau}{T_{1\prime}}\right)\right] \quad (5.3)$$

In table 3 are reported the values of T_1 and the amplitude of the two values. It is important to notice that the longest T_1 is the most relevant for all the complexes and is the one plotted in figure 14. For some of the complexes are missing the highest temperature values because the echo relaxation is too fast to allow the measurements.

Table 4: T_1 and amplitude fitting values for VO-complexes.

Complexes	T (K)	T_1 long (ns)	Amplitude 1	T_1 short (ns)	Amplitude 2
$VO(H_2O)_5$	20	$9{,}16*10^5$	83000	$3{,}22*10^5$	44980
	50	16386	66744	31028	58775
	80	6755	47007	2909	10710
	120	2447	23221	1059	887
	150	1331	7342	516	909
	200	368	-	368	-
VO-nta	20	$2{,}48*10^5$	17552	53592	12846
	50	23247	20255	7345	8247
	80	6373	15768	2189	5404
	120	2763	11863	1125	3364
	150	1375	6904	42	483
	200	-	-	-	-
$VO(oxa)_2$	20	$2{,}03*10^6$	19493	$8{,}33*10^5$	24437
	50	53576	16464	27641	9577
	80	13881	14430	7861	9403
	120	5834	14604	3228	4850
	150	2768	11293	1650	3715
	200	1548	8951	681	123
VO-dtpa	20	$1{,}09*10^6$	66250	329033	39265
	50	36538	151048	126411	40286
	80	10123	53584	4108	17233
	120	4220	26632	1650	6880
	150	2130	9198	330	2239
	200	873	22792	4,5	10290
$VO(acac)_2$	20	38657	8592	6444	19521
	50	17595	5868	4030	8094
	80	11404	3841	3290	11979
	120	-	-	-	-
	150	-	-	-	-
	200	-	-	-	-

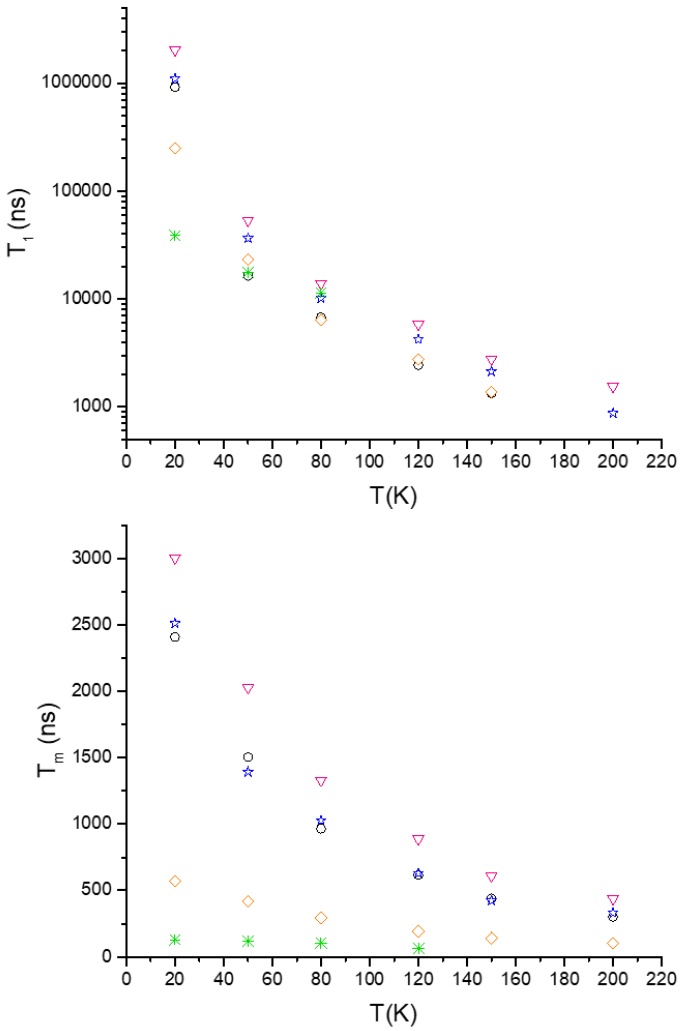

Figure 14: T_1 (top) and T_m (bottom) in function of temperature of $VO(H_2O)_5$ (black circles), VO-dtpa (blue stars), $VO(oxa)_2$ (purple triangles), VO-nta (orange squares) and $VO(acac)_2$ (green asterisks).

The concentration of the complexes, measures with Evans method, is comparable around 3 mM. It is possible to see that T_1 values for the various complexes present a significant difference at 20 K, where $VO(oxa)_2$ is characterized by the longest T_1 of the series, followed by $VO(H_2O)_5$ and VO-dtpa that show a similar value, while VO-nta and $VO(acac)_2$ present a T_1

faster and quite different respect to the other complexes. The results obtained for T_m fitting of the measures shown a significant difference between the various complexes at all the temperature points, except for $VO(H_2O)_5$ and VO-dtpa where T_m converges to a similar value.

5.3 Nuclear Magnetic Relaxometric Studies

The NMRD profiles of the vanadyl complexes were measured at various temperatures (283, 298 and 310 K) from 0.01 to 120 MHz (expressed as a function of ^1H Larmor frequency). For each NMRD profile, 25 relaxation times were measured, in order to have a good definition of the curves.

Figure 15 reports the NMRD profiles of the $VO(H_2O)_5$ complex, which presents a similar shape to the one measured by Bertini *et al*. [17]. The profiles are shown at low field a nearly constant value of relaxivity (r_1), between 0.01 to 0.1-0.2 MHz. Then there is a dispersion zone centered at 1-2 MHz and the following region with constant values at frequency above 20 MHz. At low fields, r_1 is dominated by the scalar contribution, which depends on the hyperfine coupling constant $A_H/\hbar$ and the correlation time $1/\tau_{si}$, which is the sum of the exchange rate constant ($k_{ex} = 1/\tau_M$) and the electronic longitudinal ($1/T_{1e}$) or transverse ($1/T_{2e}$) relaxation rates. The electronic relaxation times are generally nearly invariant in the temperature range used for NMRD measurements. Thus, the increase of relaxivity at low frequencies as a function of temperature indicates that r_1 is limited by a slow water exchange rate, as τ_M is longer than T_1 for the proton nuclei of the coordinated water. At high frequencies, the inner-sphere contribution to r_1

is provided by the dipolar mechanism, for which the relevant correlation time involves τ_M, T_{ie} and τ_R. The shortest among these three correlation times is τ_R, which is in the ps time scale, while τ_M and T_{ie} appear to be in the μs and ns time scales, respectively. Thus, the fast rotation of the complex in solution limits r_1 at high fields, and therefore the trend with temperature is inverted, as τ_R becomes shorter in increasing temperature.

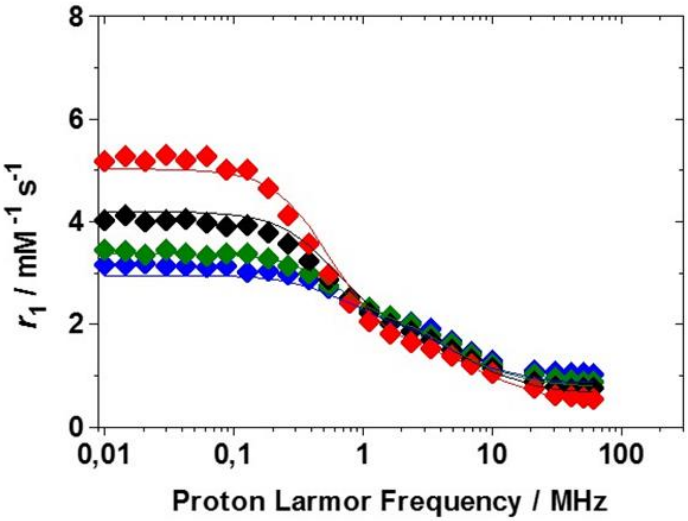

Figure 15: ^{1}H NMRD profiles at different temperatures: 283 (blue), 288 (green), 298 (black) and 310 K (red) for $[VO(H_2O)_5]^{2+}$. The solution has a pH<2 to prevent the oxidation of VO^{2+}.

For $VO(oxa)_2$ complex, Figure 16, the shape of the NMRD profiles present many similarities compared with those of $VO(H_2O)_5$ described before. In this case, however, the increase in relaxivity as function of the temperature at low fields is even more dramatic. This is possibly related to a rearrangement in the structure of the complex [22] that changes the water position from equatorial to axial.

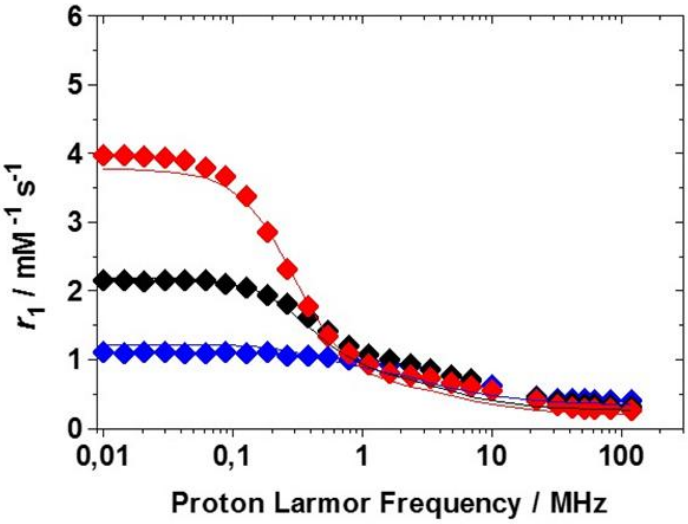

Figure 16: ^{1}H NMRD profiles (pH = 5.5) at different temperatures (283, 298 and 310 K) for $VO(oxa)_2$.

Quite different is the case of VO-nta complex (Figure 17), for which relaxivities are lower when compared with the first two complexes. The NMRD profiles show a wide region of constant relaxivity from 0.01 to 2 MHz, with a dispersion around 2-40 MHz and a fairly constant relaxivity at higher fields. This shape is characteristic of paramagnetic complexes for which the inner-sphere contribution to relaxivity arises from the dipolar mechanism. The relaxivity shows an evident decrease when increasing the temperature, which shows that τ_R is limiting proton relaxivity at high fields. At low fields, the decrease in relaxivity with temperature is likely related to the outer-sphere contribution, as increasing temperature leads to a faster diffusion.

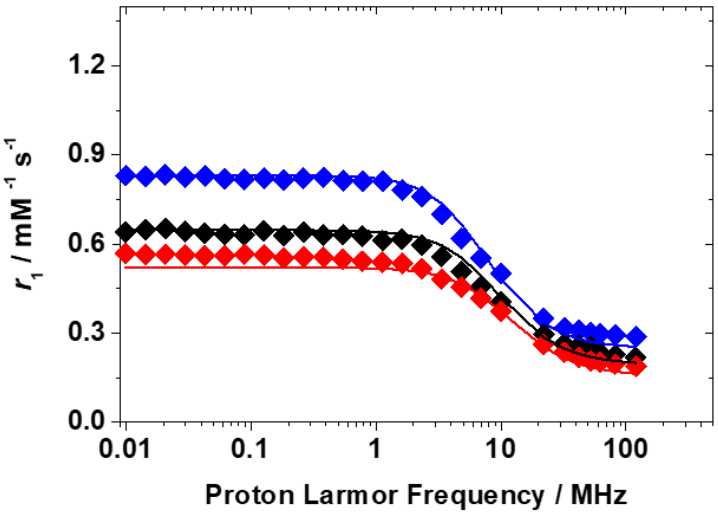

Figure 17: ^{1}H NMRD profiles (pH = 5.5) at different temperatures (283, 298 and 310 K) of VO(nta).

The NMRD profiles of the $VO(acac)_2$ complex, in Figure 18, evidence a change in the shape of the curves as a function of temperature, which may be related to the presence of different isomers in solution. [23]

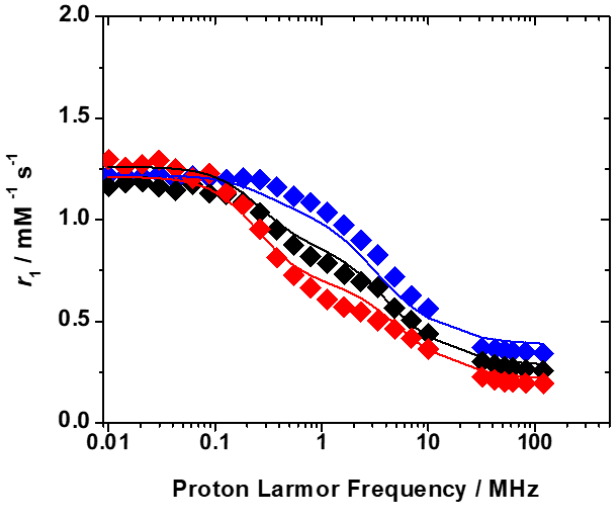

Figure 18: ^{1}H NMRD profiles (pH = 5.6) at different temperatures (283, 298 and 310 K) of $VO(acac)_2$.

The analysis of the NMRD profiles was done by fitting curves to the equations shown in chapter 2.4. Moreover, the systems were also investigated using DFT calculations performed by Professor Platas-Iglesias (University of A Coruña), which provided additional information on some important parameters that control the observed relaxivities.

To aid the fitting of NMRD data DFT calculations are performed on the $[VO(H_2O)_5]^{2+}$ system. The optimized geometry is characterized by short V-O_{cis} distances and a long V-O_{trans} distance associated with the *trans* influence of the V=O bond. The calculated distances are in excellent agreement with the experimental values obtained with X-ray diffraction measurements. [24,25,26] The calculated V=O distance (1.565 Å) is also in nice agreement with the X-ray data (1.57-1.58 Å). DFT calculations were also performed on the $[VO(oxa)_2(H_2O)]^{2-}$ system, for which X-ray structures were reported with the coordinated water molecule in both *cis* [27,28] and *trans* [29] positions with respect to the V=O bond. The calculations on the *trans* isomer systematically led to square pyramidal optimized geometries, even upon the inclusion of two explicit second-sphere water molecules. The ^{1}H NMRD data clearly show the presence of a water molecule coordinated to the VO^{2+} cation, and thus subsequent calculations were performed on the *cis* isomer (Table 5). The DFT calculations provide a V-O_{water} distance that is considerably longer than that those observed in the solid-state. The inclusion of two explicit second-sphere water molecules shortens the V-O_{water} distance by ~0.04 Å, but the calculated value remains 0.11 Å longer than the X-ray value.

Calculations performed on the $[VO(nta)(H_2O)]^-$ system provide a minimum energy conformation with the coordinated water molecule in *cis* position and the *N* atom of nitrilotriacetate occupying the *trans* position, which leads

to a long V-N distance (2.372 Å) associated with the *trans* influence of the V=O bond. This is in good agreement with the X-ray structures reported in the literature. [30,31] Again, the inclusion of explicit second-sphere water molecules causes a shortening of the V-O_{water} distance, as observed previously for Mn(II) and Gd(III) complexes. [32,33] Finally, DFT calculations yield two minimum energy geometries for the $[VO(acac)(H_2O)]^-$ system characterized by *cis* and *trans* coordination of the water molecule. The relative Gibbs free energies calculated with DFT favor the *trans* isomer by 4.1 kcal mol^{-1}. The relative energy is reversed and reduced to 0.3 kcal mol^{-1} upon inclusion of two second-sphere water molecules, and thus both forms have a significant population in solution. This is in line with EPR measurements, which evidenced the presence of the *cis* and *trans* isomers in solution. [34] As expected, the *trans* isomer displays a long V-O_{water} distance of 2.48 Å. This distance was found to be up to ~0.27 Å shorter in the solid-state. The overestimation of the V-O_{water} distance by DFT is likely related to a rather flat potential energy surface associated with the weak interaction arising from the strong trans influence of the V=O bond.

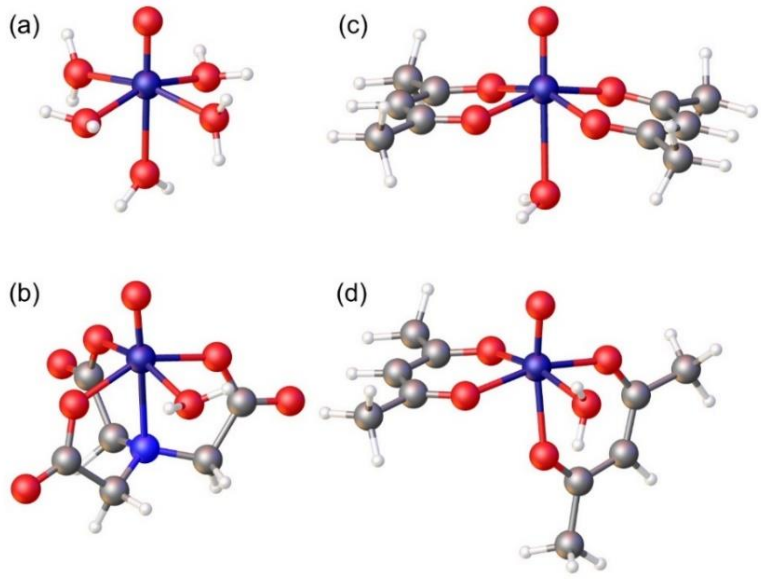

Figure 19: Geometries of $[VO(H_2O)_5]^{2+}$ (a), $[VO(nta)(H_2O)]^{-}$ (b) and $[VO(acac)(H_2O)]$ (c) and (d) obtained with DFT calculations (TPSSh/Def2-TZVPP).

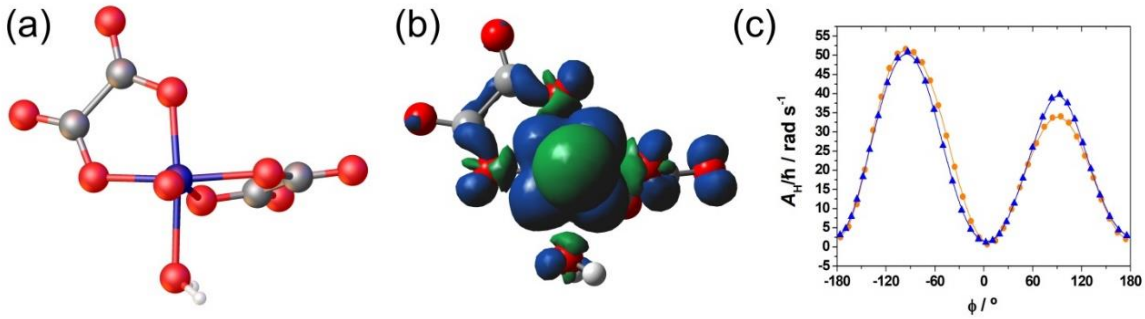

Figure 20: Geometry (a), spin density (positive values in blue) (b) and $A_H/\hbar$ values for the ^1H nuclei of the coordinated water molecule as a function of ϕ (see text) calculated for $[VO(oxa)_2(H_2O)]^{2-}$ with DFT (TPSSh/Def2-TZVPP).

Table 5: Average V-O and V-H distances (Å) and ^{1}H hyperfine coupling constants $A_H/\hbar$ of coordinated water molecules obtained with DFT calculations at the TPSSh/Def2-TZVPP level.

Complexes	**Symmetry**	$r_{V\text{-}O}$ **calc. (Å)**	$r_{V\text{-}O}$ **exp. (Å)**	$r_{V\text{-}H}$ **(Å)**	$A_H/\hbar$ **(10^6 rad s^{-1})**
$[VO(H_2O)_5]^{2+}$	*trans*-O	2.212	2.175[a] / 2.183[b] / 2.21[c]	2.888	0.544
	cis-O	2.054	2.027[a] / 2.027[b] / 2.03[c]	2.671	27.13
$[VO(oxa)_2(H_2O)]^{2-}$	*cis*-O	2.186	2.033[d] / 2.022[e]	2.667	18.22
$[VO(nta)(H_2O)]^{-}$	*cis*-O	2.128	2.016[f]/ 2.005[g]	2.682	27.22
$[VO(nta)(H_2O)]^{-}\cdot 2H_2O$	*cis*-O	2.085	-	2.587	32.68
$[VO(acac)(H_2O)]$	*trans*-O	2.479	2.196[h]	2.950	0.37
$[VO(acac)(H_2O)]\cdot$	*cis*-O	2.173	-	2.678	8.37

The calculated ^{1}H $A_H/\hbar$ values are positive, falling within the range of ca. 10-33 rad s^{-1} for water molecules in *cis* position with respect to the V=O bond, and around 0.5 rad s^{-1} for water molecules in *trans* position. Thus, longer V-O_{water} distances are characterized by lower spin densities at the ^{1}H nuclei of the coordinated water molecule, as would be expected. However, the V-O_{water} distance is not the only factor that affects the $A_H/\hbar$ values, as it becomes evident by comparing the values calculated for the $[VO(oxa)_2(H_2O)]^{2-}$ and $[VO(oxa)_2(H_2O)]^{2-}\cdot 2H_2O$ systems. Indeed, the $[VO(oxa)_2(H_2O)]^{2-}\cdot 2H_2O$ system presents a shorter V-O_{water} distance than $[VO(oxa)_2(H_2O)]^{2-}$ associated with a lower $A_H/\hbar$ value (Table 5). Inspection of the spin density calculated for the $[VO(oxa)_2(H_2O)]^{2-}$ system (Figure 20) shows that most of the positive spin density resides close to the V atom, with a shape that resembles a d_{xy} orbital, as would be expected. [35] The vanadyl oxo atom displays a negative spin density due to spin polarization, as well as the donor atoms of the metal coordination environment, though to a lesser

extent. Spin polarization results in a small but positive spin density nearby the region where the ^{1}H nuclei of the coordinated water molecule are situated. This spin density distribution suggests that the $A_H/\hbar$ values at the water ^{1}H nuclei are strongly dependent on their position with respect to the equatorial plane, with higher $A_H/\hbar$ values expected when H atoms lie on the xy plane. The $[VO(ox)_2(H_2O)]^{2-}$ system was therefore further explored by running relaxed potential energy surface scans, in which the dihedral angle ϕ defined by the V=O group and the water molecule (O=V-O-H) was varied in the range -180 to +180º (Figure 20c). The calculated $A_H/\hbar$ is positive regardless of the value of ϕ, but show two well-defined maxima at ϕ= 90 and -90º, which correspond to situations in which the H atom of the coordinated water molecule lies in the equatorial plane. On the contrary, $A_H/\hbar$ reaches the minimum values when the water O-H bond is perpendicular to the equatorial plane (ϕ= 0, 180º). The $A_H/\hbar$ values obtained by averaging those obtained for the two ^{1}H nuclei of the coordinated water molecule were found to vary in the range 35.5-9.4 rad s^{-1}, and thus the orientation of the water molecule with respect to the xy plane is expected to have a significant impact in the $A_H/\hbar$ values.

The EPR measurements described above evidenced significant variations of the ^{51}V hyperfine coupling constants for the complexes investigated in this work, while *g*-factors appear to be quite insensitive to the nature of the ligands coordinated to the V(IV) centre (Table 1). The values of A_x, A_y and A_z are calculated with relativistic DFT calculations using the TPSS functional, which provides more accurate results than the hybrid TPSSh. The results (Table 6) show that DFT predicts the experimental hyperfine coupling constants to rather good accuracy, including the observed trend that the

absolute *A* values decrease following the sequence $[VO(H_2O)_5]^{2+}$ > $[VO(nta)(H_2O)]^-$ > $[VO(ox)_2(H_2O)]^{2-}$ > $[VO(acac)(H_2O)]^-$. The *A*-tensor values calculated for the *cis* and *trans* isomers of $[VO(acac)(H_2O)]^-$ are rather similar. Thus, it is possible to conclude that DFT describes rather accurately the spin density distributions in these complexes.

Table 6: Average V-O and V-H distances (Å) and ^1H hyperfine coupling constants $A_H/\hbar$ of coordinated water molecules obtained with DFT calculations at the TPSSh/Def2-TZVPP level. [a] Data for the *trans* isomer. [b] Data for the *cis* isomer.

Complexes	Method	A_x	A_x	A_x
$[VO(H_2O)_5]^{2+}$	Calc.	-241	-244	-558
	Exp.	-206.5	-206.5	-546
$[VO(oxa)_2(H_2O)]^{2-}$	Calc.	-187	-194	-493
	Exp.	-192	-181	-520
$[VO(nta)(H_2O)]^-$	Calc.	-201	-202	-498
	Exp.	-203	-187	-527
$[VO(acac)(H_2O)]$	Calc.[a]	-159	-186	-480
	Calc.[b]	-191	-206	-496
	Exp.	-161	-176	-498

The first interesting aspect that emerged from NMRD fitting is that for $VO(H_2O)_5$, $VO(oxa)_2$ and $[VO(acac)_2(H_2O)]$ not only the dipole-dipole mechanism contributes to the inner-sphere relaxivity, but also an additional contact term contributes, which is responsible for the dispersion shape observed in Figure 15 and Figure 16. For $[VO(nta)(H_2O)]^-$ the inclusion of a contact contribution was not required. The fits of the ^1H NMRD data were performed by fixing some parameters to standard values: the diffusion coefficient $D_{V\text{-}H}^{298}$ and its activation energy E_D were fixed to standard values of 22.4×10^{-10} m^2 s^{-1} and 20 kJ mol^{-1}. The relative diffusion of water and the paramagnetic complex is expected to be dominated by the fast water

diffusion, and thus these parameters should be similar for all complexes and close to those characterizing the self-diffusion of water. [36] The distance of closest approach of an outer-sphere water molecule was also fixed to the typical value of 3.6 Å, except for the $VO(oxa)_2$ complex. In the latter case, a_{V-H} was fixed to a slightly shorter value of 3.4 Å, as otherwise the fits provided a very long value of τ_R^{298}. The high negative charge of this complex may induce rather strong hydrogen bonds with outer-sphere water molecules, resulting in a shorter a_{V-H} distance. The r_{V-H} distances were fixed to the values obtained with DFT calculations, except in the case of $[VO(acac)_2(H_2O)]$, for which is taken an intermediate value with respect to those calculated for the *cis* and *trans* isomer. Finally, the number of coordinated water molecules was fixed to 5 for the aqua-ion and to q = 1 for all other complexes. Table 7 summarizes all the parameters derived from the NMRD fitting.

The τ_R^{298} values obtained from NMRD fitting for $VO(H_2O)_5$, and $VO(acac)_2$ are in excellent agreement with those estimated with EPR measurements (47.8 and 77 ps, respectively). The corresponding activation energy (E_r), which generally assumed values in the range 18-22 kJ/mol, show somewhat higher values for $VO(H_2O)_5$ and $VO(acac)_2$. For $VO(oxa)_2$ the fit of NMRD data results in a significant discrepancy with respect to the EPR correlation time. It is tentatively attributed to this discrepancy to a significant second-sphere contribution to relaxivity associated with the negative charge of the complex. Significant second-sphere contributions to relaxivity were observed for Gd(III) complexes having high negative charge (i. e. incorporating phosphonate groups). [37]

The values of $A_H/\hbar$ obtained from the fits for $VO(H_2O)_5$ and $VO(oxa)_2$ and those obtained with DFT are in satisfactory mutual agreement, providing

support to the analysis of the experimental data. For $[VO(acac)_2(H_2O)]$ the value obtained from NMRD lies between those calculated for the *cis* and *trans* isomers, which are both present in solution.

The τ_M^{298} for the vanadyl aquo-ion is sensibly longer compared to the values observed for $[Gd(H_2O)_8]^{3+}$ (τ_m^{298} = 1.2 ns) [38] and $[Mn(H_2O)_6]^{2+}$ (τ_m^{298} = 35.5 ns). [39] The τ_M^{298} value of 19.1 μs is also sensibly shorter than that determined for the equatorial water molecules using ^{17}O NMR measurements (2 ms). [40] This suggests that ^1H exchange is faster than the exchange of the whole water molecule due to the prototropic contribution to water exchange at the acidic pH used for NMRD measurements. On the other hand, $VO(oxa)_2$ and VO(nta) show similar water exchange rates, while for $VO(acac)_2$ it is slightly slower. The related activation enthalpy assumes a very similar value for all complexes except $VO(oxa)_2$. The very high enthalpy barrier determined for the latter may be related to the expulsion of the coordinated water molecule from the inner-coordination sphere as a result of interconversion between the *cis* and *trans* isomers. This process would shift the coordinated water molecule to the labile *trans* position, facilitating water exchange. Support for this hypothesis is provided by the detection of a minor fraction of the *trans* isomer in solution by using EPR measurements (4%). [22] A ^1H exchange mechanism involving rearrangement of the water ligand from an equatorial to an axial position was suggested previously on the grounds of a T_2 NMR relaxation study. The same work reported a ^1H τ_m^{298} value for $VO(oxa)_2$ (τ_m^{298} = 5.4 μs) in good agreement with that determined here. [41]

Table 7: Parameters from the fit of the NMRD data of VO-complexes (*fixed during the analysis). [a] from reference. [17]

Parameters	$[VO(H_2O)_5]^{2+}$	$[VO(oxa)_2(H_2O)]^{2-}$	$[VO(nta)(H_2O)]^{-}$	$[VO(acac)_2(H_2O)]$
τ_M^{298} (μs)	19.1 ± 0.9	5.5 ± 0.5	6.3 ± 1.7	9.1 ± 1.8
$\Delta H_M^{\ddagger}$ ($kJ\ mol^{-1}$)	18.8 ± 1.2	64.6 ± 3.6	24.0 ± 5.9	18.2 ± 3.3
τ_R^{298} (ps)	43.5 ± 1.0	75.8 ± 2.8	41.9*	72.4 ± 4.8
E_r ($kJ\ mol^{-1}$)	26.8 ± 1.2	20.0*	15.7*	29.6 ± 3.6
τ_s^{298} (ns)	0.99 ± 0.01	0.70 ± 0.06	0.50 ± 0.10	0.90 ± 0.09
E_s ($kJ\ mol^{-1}$)	1.0*	37.5 ± 3.1	1.0*	1.0*
$D_{V\text{-}H}^{298}$ ($10^{-10}\ m^2\ s^{-1}$)	22.4*	22.4*	22.4*	22.4*
E_D ($kJ\ mol^{-1}$)	20.0*	20.0*	20.0	20.0*
$A_H/\hbar$ ($10^6\ rad\ s^{-1}$)	20.8 ± 1.5	22.3 ± 0.8	-	11.8 ± 1.2
$r_{V\text{-}H}$ (Å)	2.671*	2.667*	2.682*	2.75*
$a_{V\text{-}H}$ (Å)	3.6*	3.4*	3.6*	3.6*
q	5*	1*	1*	1*

References Chapter 5

[1] M. C. Heffern, L. M. Matosziuk and T. J. Meade, *Chem. Rev*., 2014, 114, 4496–4539.

[2] F. Troiani and M. Affronte, Chem. Soc. Rev., 2011, 40, 3119, Atzori M., Sessoli R., *J. Am. Chem. Soc*., 2019, 141, 11339–11352.

[3] Zadrozny J.M., Niklas J., Poluektov O.G., Freedman D.E., *J. Am. Chem. Soc.,* 2014, 136, 15841–15844.

[4] Atzori M., Tesi L., Morra E., Chiesa M., Sorace L., Sessoli R, *J. Am. Chem. Soc.*, 2016, 138, 2154–2157.

[5] Atzori M., Morra E., Tesi L., Albino A., Chiesa M., Sorace L., Sessoli R., *J. Am. Chem. Soc.*, 2016, 138, 11234–11244.

[6] J. W. Chen, R. L. Belford and R. B. Clarkson, J. Phys. Chem. A 1998, 102, 2117-2130.

[7] Devkumar Mustafi, Bo Peng, Sean Foxley, Marvin W. Makinen, Gregory S. Karczmar, Marta Zamora, John Ejnik, Heather Martin, *J. Biol. Inorg. Chem*., 2009, 14, 1187–1197.

[8] D. Rehder, *Inorg. Chim. Acta,* 2020, 504, 119445.

[9] J. A.L. da Silva, J. J.R. F. da Silva, A. J.L. Pombeiro, *Coo. Chem. Rev*., 2011, 255, 2232– 2248.

[10] E. Anoardo, G. Galli, and G. Ferrante, *Appl. Magn. Reson*., 2001, 20, 365-404.

[11] R. E. Lauffer, *Chem. Rev*., 1907, 87, 901-927.

[12] P. Caravan, J. J. Ellison, T. J. McMurry, R. B. Lauffer, *Chem. Rev.,* 1999, 99, 2293-2352.

[13] J. Wahsner, E. M. Gale, A. Rodríguez-Rodríguez, P. Caravan, *Chem. Rev.*, 2019, 119, 957−1057.

[14] I. Hancu, W. T. Dixon, M. Woods, E. Vinogradov, A. D. Sherry, R. E. Lenkinski, Acta Radiol., 2010, 51, 910-923.

[15] J. Kowalewski, D. Kruk, G. Parigi, *Adv. Inorg. Chem.*, 2005, 57, 41-104.

[16] R. M. Steele, J.-P. Korb, G. Ferrante, S. Bubici, *Magn. Reson. Chem.*, 2015, 502-509.

[17] Ivano Bertini, Zhicheng Xia, Claudio Luchinat, J. Magn. Res., 1992, 99, 235-246.

[18] Stefan Stoll, Arthur Schweiger, Biol. Magn. Reson. 2007, 27, 299-321.

[19] Y. Zhou, B. E. Bowler, G. R. Eaton, S. S. Eaton, *J. Magn. Res*., 1999, 139, 165–174.

[20] G. R. Eaton, S. S. Eaton *J. Magn. Res.,* 1999, 136, 63–68.

[21] Stefan Stoll, Arthur Schweiger, *J. Magn. Reson.*, 2006, 178, 42-55.

[22] P. Buglyó, E. Kiss, I. Fàbiàn, T. Kiss, D. Sanna, E. Garribba, G. Micera, Inorg. Chim. Acta, 2000, 306, 174–183

[23] V. Nagarajan, B. Muller, O. Storcheva, K. Kohler, A. Poppl, *Res. Chem. Intermed.*, 2007, 33, 705-724.

[24] Magnussen, M., Brock-Nannestad, T., Bendix, J., *Acta Cryst*., 2007, C63, m51-m53.

[25] Krakowiak, J., Lundberg, D., Persson, I. A, *Inorg. Chem.*, 2012, 51, 9598-9609.

[26] Tézé, A., Marchal-Roch, C., So, H., Fournier, M., Hervé, G., *Solid State Sci*., 2001, 3, 329-338.

[27] Oughtred, R. E., Raper, E. S. The Crystal., *Acta Cryst.* 1976, B32, 82-87.

[28] Lin, L., Wu, S., Huang, C., Zhang, H., Huang, X., Lian, Z., *Acta Cryst.*, 2004, E60, m631-m633.

[29] Sehimi, H., Chérif, I., Zid, M. F., *Acta Cryst.*, 2016, E72, 1002–1005.

[30] Tesmar, A., Inkielewicz-Stepniak, I., Sikorski, A., Wyrzykowski, D., Jacewicz, D., Zieba, P., Pranczk, J., Ossowski, T., Chmurzynski, L., *J. Inorg. Biochem.*, 2015, 152, 53-61.

[31] Tesmar, A., ., Wyrzykowski, D., Kazimierczuk, K., Klak, J., Kowalski, S., Inkielewicz-Stepniak, I., Drzezdzon, J., Jacewicz, D., Chmurzynski, L., *Z. Anorg. Allg. Chem.*, 2017, 643, 501–510.

[32] Esteban-Gómez, D., de Blas, A., Rodríguez-Blas, T., Helm, L., Platas-Iglesias, C., *Chem. Phys. Chem.,* 2012, 13, 3640 – 3650.

[33] Patinec, V., Rolla, G. A., Botta, M., Tripier, R., Esteban-Gómez, D., Platas-Iglesias, C., *Inorg. Chem.*, 2013, 52, 11173−11184.

[34] Amin, S. S., Cryer, K., Zhang, B., Dutta, S. K., Eaton, S. S., Anderson, O. P., Miller, S. M., Reul, B. A:, Brichard, S. M., Crans, D. C., *Inorg. Chem.*, 2000, 39, 406-416.

[35] Ruiz, E., Cirera, J., Alvarez, S., *Coord. Chem. Rev.* 2005, 249, 2649-2660.

[36] Mills, R., *J. Chem. Phys*., 1973, 77, 685-688.

[37] Elhabiri, M., Abada, S., Sy, M., Nonat, A., Choquet, P., Esteban-Gómez, D., Cassino, C., Platas-Iglesias, C., Botta, M., Charbonnière L. J., *Chem. Eur. J.,* 2015, 21, 6535 – 6546.

[38] Powell, D. H., Ni Dhubhghaill, O. M., Pubanz, D., Helm, L., Lebedev, Y. S., Schlaepfer, W., Merbach, A. E., *J. Am. Chem. Soc*., 1996, 118, 9333-9346.

[39] Esteban-Gómez, D., Cassino, C., Botta, M., Platas—Iglesias, C. *RSC Adv*., 2014, 4, 7094–7103.

[40] Wüthrich, K., Connick, R. E. *Inorg. Chem.*, 1967, 6, 586-590.

[41] Nagypál, I., Fábián, I., *Inorg. Chim. Acta*, 1982, 61, 109-113.

Conclusion

In this Ph.D. thesis, magnetic resonance techniques were used to investigate the properties of vanadyl species in various systems. The first part reports studies on supported systems, where VO^{2+} species are grafted on the surface of two different materials, TiO_2 and ZSM-5. In the second part, the focus shifts to the properties of vanadyl molecular complexes in water solution, by combining EPR, NMR and DFT techniques.

The local structure of vanadium ions supported on shape engineered TiO_2 nanoparticles have been studied. The formation of vanadyl ions by grafting with VCl_4 on nanoparticles with different distributions of {001} and {101} terminations act as an efficient surface probe, allowing to titrate the different terminations, thanks to distinctively different spin-Hamiltonian parameters. The observation of two distinct families of surface V species has been demonstrated and it is possible to assign the EPR spectroscopic features to VO^{2+} surface ions at TiO_2 terminations. It is also possible to observe a small ^{51}V hyperfine interaction in HYSCORE spectra which points to the presence of mixed-valence dimeric units at the surface, similar to molecular $V_2O_3^{3+}$ species, whereby most of the electron spin density is concentrated at one V centre with a fraction corresponding to about 3% delocalized over the second V nucleus.

On the other hand, two different methodologies, grafting with $VOCl_3$ and wet impregnation with NH_4VO_3, were tested on TiO_2 supports to study the nature of vanadium surface species and their interaction with NH_3. CW

EPR experiments confirmed the reduction of V^{5+} to V^{4+} after reaction with ammonia. HYSCORE spectra provided additional information about the hyperfine coupling between the vanadium electron spin and ^{14}N and ^{1}H nuclei, which is compatible with reaction intermediates that involves ammonia fragments directly coordinated to vanadyl species in the equatorial plane. In the impregnated sample, the T_m filtered ESE-detected EPR experiments reveal an additional reduction of Ti^{3+} ions from the substrate, which points to a non-innocent role of the substrate during the reaction of the V sites with ammonia.

The same experimental protocol was used to obtain V species supported on H-ZSM-5. CW and pulse EPR experiments, at different frequencies, provide evidence for the formation of VO^{2+} species upon hydrolysis of the molecular precursor. The combination of ^{1}H, ^{27}Al and ^{17}O HYSCORE experiments (Q-band) allowed a detailed geometrical description of the structure of the isolated single metal sites.

In the last part of the thesis, vanadyl molecular complexes in water solution were investigated. In particular, a series of ligands were selected, oxalic acid (oxa), nitrilotriacetic acid (nta) and acetylacetonate (acac), and compared with vanadyl aquo-complex ($VO(H_2O)_5$) to study the role of water coordination in a specific site. CW EPR in solution provided an estimate of the rotational correlation time of the complexes, while with pulse EPR the electronic T_1 and T_2 relaxation times were measured. From the NMRD profiles, measured in collaboration with Professor Botta evidence was obtained that VO-nta features equatorially coordinated water, while VO-oxa shows a rearrangement of the structure that is activated at higher temperatures. Meanwhile, analysis of the $VO(acac)_2$

complex indicated the concomitant presence of the two isomers in solution. The experimental results were confirmed and corroborated by DFT calculations (performed by Professor Platas-Iglesias from University of A Coruña).

Appendix

Pubblications

I. Valeria Lagostina, Maria Cristina Paganini, Mario Chiesa, Elio Giamello "*Exploring the Interaction of Ammonia with Supported Vanadia Catalysts by Continuous Wave and Pulsed Electron Paramagnetic Resonance (EPR) Spectroscopy*" The Journal of Physical Chemistry C, 2019, 123, 7861−7869.

II. Valeria Lagostina, Loredana Leone, Fabio Carniato, Giuseppe Digilio, Lorenzo Tei and Mauro Botta ''*Electronic Effects of the Substituents on Relaxometric and CEST Behaviour of Ln(III)-DOTA-Tetraanilides*'' Inorganics, 2019, 7, 43.

III. Valeria Lagostina, Enrico Salvadori, Mario Chiesa, Elio Giamello "*Electron paramagnetic resonance study of vanadium exchanged H-ZSM5 prepared by vapor reaction of VCl_4. The role of ^{17}O isotope labelling in the characterisation of the metal oxide interaction*" Journal of Catalysis, 2020, 391, 397–403.

Manuscripts in preparation

I. Valeria Lagostina, Eleonora Romeo, Annamaria Ferrari, Mario Chiesa *''Atomic-level Insights into the Geometric and Electronic Structure of Vanadium (IV) Sites at Well-defined TiO_2 Anatase Crystals''*

II. Valeria Lagostina, Fabio Carniato, Carlos Platas-Iglesias, Mario Chiesa, Mauro Botta *''Magnetic Properties and Relaxation in Vanadium (IV) Complexes''*

Abbreviations and Acronyms

ACAC	Acetylacetonate
CW	Continuous Wave
DFT	Density Functional Theory
DTPA	Diethylenetriamine pentaacetate
ENDOR	Electron-Nuclear Double Resonance
EPR	Electron Paramagnetic Resonance
ESE	Electron Spin Echo
ESEEM	Electron Spin Echo Envelop Modulation
FFC	Fast-Field Cycling
FID	Free Induction Decay
HYSCORE	Hyperfine Sublevel Correlation
MRI	Magnetic Resonance Imaging
NMR	Nuclear Magnetic Resonance
NMRD	Nuclear Magnetic Relaxation Dispersion
NTA	Nitrilotriacetate
OXA	Oxalate
SCR	Selective Catalytic Reduction
SG	Sol-gel
WI	Wet-Impregnation